SOLUTION-PROCESSED

ORGANIC LIGHT SOURCES FOR

MICROFLUIDIC LAB-ON-A-CHIP SYSTEMS

DISSERTATION

for the acquisition of the academic title

Doktor-Ingenieur (Dr.-Ing.)

submitted to the Council of the Faculty of Physics and Astronomy

of the Friedrich-Schiller-Universität Jena

by M.Sc. Zhe Shu

born in Xianning, Hubei, P. R. China on 17.08.1987

Supervisors:

Major Supervisor: **Prof. Dr. Andreas Tünnermann**
                                             Friedrich-Schiller-Universität Jena
Associate Supervisor: **Prof. Dr. Klaus Dieter Jandt**
                                               Friedrich-Schiller-Universität Jena
Associate Supervisor: **Prof. Dr. Romain Quidant**
                                The Institute of Photonic Sciences, Barcelona

Day of the Disputation: 30th November 2017

Abstract

Microfluidic Lab-on-a-chip (LoC) systems provide a miniaturized platform for sample processing and biological / medical diagnostics. This system provides great potential in personalized and localized point-of-care diagnostic applications. However, despite the numerous developments on LoC technology, many external lab-scale components such as fluorescent excitation light sources are still required at the current state of the art. In an effort to address this, in this dissertation, organic light sources have been thoroughly investigated as cost-efficient excitation light sources for fluorescence sensing on microfluidic LoC systems by solution-processing manufacturing methods. In particular, inkjet printing techniques are used exclusively for the first time as a vacuum-free, mask-free, low processing temperature patterning method in the fully solution-processed organic light sources.

When tested on highly flat and smooth substrates, organic light-emitting diodes (OLED) exhibit high brightnesses, yet demonstrate difficulty for fully solution processing. With a novel inkjet-printable Al:ZnO:PEI electron injection layer (EIL), the costly ITO anode and evaporated EIL/cathode can be replaced by inkjet-printable conductive polymer PEDOT:PSS. A brightness of > 16 000 cd/m² can be achieved under 40 V pulses from a fully solution-processed yellow OLED, which is comparable with the available state-of-the-art devices. For rougher or curved substrates, it is favorable to use light-emitting electrochemical cells (OLECs) instead of OLEDs. The *in situ* electrochemical doping of OLECs brings advantages of higher surface roughness tolerance and direct solution-processing possibility. However, doping also induces low brightness and short lifetime. Therefore, in an effort to improve emission brightness and operational lifetime under the voltage-pulsed mode, dopant concentration and active layer thickness of OLEC are investigated for the first time. The optimized solution-processed blue OLEC can emit a brightness as high as 4000 cd/m² with a lifetime > 10 000 pulses at 2800 cd/m². Furthermore, an on-chip demonstrator has been constructed by integrating solution-processed blue OLEC with an OPD and two orthogonally oriented linear polarizers on a glass chip. This is the first on-chip fluorescent sensor using solution-processed OLEC for fluorescent excitation. The sensor can detect a minimum concentration of as low as 1 μM Fluorescein (FAM) in water, which is better than the comparable reported setup. In conclusion, the manufacturing procedures and device designs introduced here provide a general guideline for integrating organic light sources as cost-efficient on-chip fluorescent excitation sources.

Table of Contents

1 Introduction and motivation

Microfluidic Lab-on-a-chip (LoC) systems provide a miniaturized platform for sample processing and biological / medical diagnostics. Its proposed advantages include: reduction of user error and sample usage, fast and inexpensive analysis, portability and automation potential. It provides great potential in personalized and localized point-of-care diagnostic applications. However, despite the numerous developments on LoC technology [1,2], many external lab-scale components and devices are still required at the current state of the art. Consequently, much of today's research has focused on the integration of functionalities such as micro-channels, micro-pumps, and micro-heaters directly onto microfluidic chips to realize monolithic and disposable point-of-care sensing platforms [3–9]. One of the most important functionalities on a microfluidic LoC system is the fluorescence sensor. Because of its high sensitivity as well as selectivity, it is the most common diagnostic method in biological and medical applications [10,11]. However, very few examples of fully integrated, compact fluorescence sensing systems on microfluidic chips can be found. Widely-used fluorescent excitation light sources such as LASERs or LEDs have relatively large dimensions and are quite expensive. The typical manufacturing process of silicon-based optoelectronics requires high temperature, high vacuum, chemical etching, photo-lithography. This process is not compatible with microfluidic LoC substrates. Moreover, they have limited emission-wavelength-tuning abilities and big differences in manufacturing processes for different emission wavelengths. Therefore, they can only be separately integrated by means of hybrid assembly [12].

In order to reduce the manufacturing cost, functional materials such as conductive polymers, light-emitting polymers (LEP), and functional metal/metal oxide nanoparticles have been tailored to dissolve into common solvents. Thus, functional thin films can be deposited via solution-processed manufacturing processes such as printing and solution-based coating techniques. Amongst numerous solution-processing techniques, drop-on-demand inkjet printing is the most promising technique for functionality integrations on microfluidic LoC systems. Firstly, the intrinsic solution-based process provides thin film deposition under ambient conditions or inert atmospheres, and therefore avoiding a costly high vacuum process; secondly, its digital drop-on-demand material deposition property eliminates the use of high-cost masks and/or lithographic-based patterning processes; thirdly, low drying and curing temperatures are sufficient for functionalization. Thus, it is com-

patible with low-cost disposable plastic and paper-based substrates; last but not least, inkjet printing is a non-contact, direct writing technique that makes it particularly suitable to directly integrate functionalities onto substrates with various 3D structures such as microfluidic chips.

With the aforementioned, this dissertation focuses on developing cost-efficient excitation light sources that can be directly integrated onto microfluidic LoC systems for fluorescence sensing. With this aim, the following requirements should be fulfilled:

1) Suitable light excitation wavelengths to excite specific fluorescent dyes for sensing;
2) good solution-processing ability via inkjet printing for cost-efficient manufacturing;
3) good compatibility and integration ability on sensing chips;
4) high emission brightness to achieve good sensitivity;
5) sufficient operational lifetime at relatively high brightness.

Organic light sources, such as the organic light-emitting diode (OLED) and the organic light-emitting electrochemical cell (OLEC), have been intensively investigated and demonstrate great emission wavelength coverage, particularly in the visible range. Organic light-emitting materials with different and specific emission wavelengths can be designed and chemically synthesized to meet a range of specific application requirements in dimension and shape [13]; even UV and IR emission wavelengths can be covered [14–16]. The relatively low long-term stability of organic light sources is not a critical factor in analytes due to the short lifetime of the target application in this dissertation. Therefore, organic light sources show great potential in sensing applications and fulfills requirement (1).

In the case of OLEDs, researchers have already been exploring and developing them as excitation light sources for on-chip fluorescence sensing platforms [17,18]. From these efforts, OLEDs have demonstrated suitable emission brightness and stability for fluorescence sensing, meeting requirement (4) and (5). Much higher emission brightness can be achieved especially when OLEDs are operated under pulsed mode [19]. Moreover, the intrinsic flexibility of OLEDs has attracted researchers and designers to develop OLEDs for innovative applications that fill specific niches such as transparent window screens [20], car rear lighting [21] and artistic lighting designs [22]. Although OLEDs have been developed as a mature display technology that currently dominates smart-phone screens in

the global market [23], the manufacturing process of OLEDs still relies highly on the vacuum-based thermal evaporation process. This process requires a high vacuum, high processing temperature as well as shadow mask for patterning. Despite the high potential of manufacturing OLEDs using solely solution-processing techniques [24–30], very few examples have been reported [24] and no solution-processed OLEDs have been integrated and tailored for on-chip fluorescent sensing applications.

(1) The first goal of this work is to develop a manufacturing recipe of OLEDs using fully solution-processing techniques, specifically inkjet printing.

Apart from tremendous efforts on fully solution-processing OLEDs, few reported examples could be found. In particular, no all-inkjet-printed OLEDs could be found. Most claimed fully solution-processed OLEDs are still using pre-patterned transparent anode ITO and thermally evaporated metal cathodes. The reasons for this are an interlayer mixing issue due to complex layer structures, difficulties in producing ultrathin work-function adaptation layers, and usage of non-soluble and non-air-stable metal cathodes. Hence, simplified layer structure and solution-processable electrodes as well as work-function interlayers are the key points of interest for fully solution-processing OLEDs. Inkjet printable conductive polymer PEDOT:PSS traditionally served as the hole injection layer (HIL) for OLEDs device due to its high work function (-5.2 eV) and low hole injection barriers to most LEPs. Recently, researchers and commercial companies have been improving the electrical conductivity of PEDOT:PSS (up to 3000 S/cm) using various methods [31–34]. Thus, PEDOT:PSS alone can serve as an inkjet printable electrode. In order to reduce the electron injection barrier, a novel inkjet-printable single-layer electron injection layer (EIL) is introduced in this dissertation. In effect, OLEDs with much higher emission brightness can be solution-processed with a simple 4-layer structure. The novel EIL was inkjet printed from an Al-doped ZnO nanoparticle dispersion mixed with the work-function adaptation polymer, PEI.

Nevertheless, OLEDs require a substrate surface with high flatness and smoothness to achieve good efficiency and stability. This can be problematic when OLEDs should be deposited onto polymeric microfluidic chips with 3D micro-structures and relatively rough surfaces. Conversely, organic light-emitting electrochemical cells (OLECs)-an emerging OLEDs alternative-has been intensively investigated for low-cost, low-brightness display and signaling applications [35,36]. Compared to OLEDs, the additional dopants bring

OLECs the advantages of simple device architecture, fully solution-processing ability, simple chip integration as well as relatively high roughness and flatness tolerance. Therefore, it is a favorable light source in terms of solution-processing and polymeric microfluidic LoC system integration, fulfilling requirement (2) and (3). However, the even lower emission efficiency, long turn-on time, and shorter operational lifetime hinder its development in high brightness sensing applications. Furthermore, there is no OLEC reported for sensing applications.

(2) The second goal of this work is to provide the knowledge and develop the parameters for sufficient excitation performance in fully solution-processed OLEC.

A blue emitter was chosen for demonstration, because it provides high injection barriers and thus has complex layer structures as well as material compositions. If the blue emitter works well, the recipe can be easily transferred to other visible colors. Voltage-pulsed driving operation is introduced and investigated in order to overcome the intrinsic low brightness and short lifetime of OLECs. A working blue OLEC can be easily solution-processed by spin-coating an OLEC active layer between inkjet printed Ag and PEDOT:PSS layers. Although there is high deviation of surface flatness of bottom Ag electrode, a brightness of more than 1000 cd/m² can be emitted under pulsed mode. Furthermore, as the device performance highly depends on dynamic electrochemical doping, various dopant concentrations and active layer thicknesses have been investigated to improve emission brightness and device stability. Hence, a material and device design recipe for tailoring OLEC for fluorescence sensing applications can be developed.

(3) The final goal of this work is to demonstrate a high on-chip sensing performance using an integrated solution-processed organic light source.

With this aim, a solution-processed blue OLEC and OPD are integrated onto a glass chip. Widely used fluorescent dye (FAM) is diluted in water at various concentrations. Two orthogonally oriented linear polarizers were used to shield detector from the excitation light. The fluorescence sensor with integrated fully solution-processed OLEC and OPD is first reported. Moreover, to demonstrate the flexibility of OLEC and simple transferability of emission wavelength, yellow OLECs were fabricated on ultrathin glasses. A concept of further increasing emission brightness was also achieved via a tandem OLED/OLEC structure.

This dissertation is structured as follows: Chapter 2 reviews the basic concepts and state of the art of organic electronics, organic light-emitting diodes, organic light-emitting electrochemical cells, solution-processing techniques, and the use of OLEDs for medical / chemical fluorescence sensing. Chapter 3 provides the theoretical model and principles of improving the emission brightness and operation lifetime for organic light-emitting devices. Chapter 4 contains the solution-processing manufacturing process (i.e. spin coating plus inkjet printing) of OLECs and OLEDs; device characterization methods are also included. In chapter 5, a fully solution-processed yellow OLED with a novel inkjet-printed interlayer of Al-doped ZnO and a PEI mixture is introduced. The OLED devices are then characterized under voltage-pulsed mode. Chapter 6 describes the device characterization of solution-processed blue OLECs under voltage-pulsed operation. It includes a study of maximum emission brightness and time constant behavior under voltage-pulsed operation with respect to the mass ratio of LEP and dopants as well as active layer thickness. Described in chapter 7 is devices with ITO-free OLECs, tandem OLED and OLEC, and a demonstrator of integrated OLEC, OPD as well as polarization filters on a glass chip. Chapter 8 concludes this dissertation with a summary and outlook.

2   Concepts and state-of-the-art of organic light sources

This chapter describes basic concepts and the state-of-the-art of most relevant techniques to this dissertation. Firstly, an overview of printed electronics and solution-processing techniques are introduced. Next, the basic working concept and state-of-the-art of organic light-emitting diodes (OLEDs) and organic light-emitting electrochemical cells (OLECs) are explained. Finally, current status of integrating OLEDs for medical / chemical fluorescence sensing are reviewed.

2.1   Printed electronics and solution-processing techniques

In 20th century the electronics, in particular inorganic semiconductors, have remarkably advanced our daily lives and altered the way the world works. The products such as computers, robots, Televisions, smart-phones, solar cells and light-emitting diodes (LED) become increasingly indispensable. However, the great success of inorganic devices such as silicon semiconductors is based on mass production and miniaturization of function units like transistors. Furthermore, a typical high-temperature and vacuum-based process is used in inorganic electronic industrials, which limits the applications in flexible, high throughout and personalized applications. Within the last three decades, the emerging and significantly developed organic and printed electronics have become a key technology to fulfill these niches. The solution-processing manufacturing of organic materials can highly reduce the number of vacuum processes and hence manufacturing cost, particularly for large-area flexible electronics [37]. Organic and printed functional materials are typically processed at low temperatures (< 200 °C), which provides the possibility of using cost-efficient flexible polymeric and paper substrates [38]. High physical and chemical tunable properties, as well as combination flexibility in organic chemistry provides organic materials with rich mechanical, electrical and optical properties. For example, conducting polymer poly(3,4-ethylenedioxythiophene) polystyrene sulfonate (PEDOT:PSS, invented by Bayer AG) [39][40] provides good conductivity (up to 1000 S/cm), high transparency (90% transmission in visible range) and no dependency of metal element such as copper, silver, gold and Aluminum. It is also highly flexible and lightweight, which can directly integrate the electrical functions on textile and plastics. In addition to the pure electrical conducting properties, conjugated polymers exhibit various electronic and optical functionalities by attaching different side chains and engineering the main chain architecture

[41–43]. Well-developed examples include organic semiconductors, in particular organic light-emitting diodes (OLED) [44–46], organic photovoltaics (OPV) [43,47] as well as organic photodiodes (OPD) [48], and organic field-effect transistors (OFET) [49].

Solution-based deposition method or solution-processing technique provides advantages of potentially lower capital investment, compatibility with large area substrates, lower material consumptions, vacuum free and lower processing temperature, and compatibility with flexible substrates. This technique includes but is not limited to spin-coating [50], spray coating [51], dip coating [52], slot-die coating [53] and printing methods such as inkjet [54,55], screen [56], and gravure printing [57]. Solution-based coating methods such as spin coating, spray coating, and dip coating are simple methods to deposit thin layers by dropping functional solutions onto highly spanned target substrates, spraying over static target substrates, or dipping the target substrates into functional solutions which are then withdraw with steady speed. Specifically, spin coating is widely used for preparing small sized OLED samples [58,59]. It is commonly used to produce photoresist thin films in microelectronics industries. With rapid spinning of the substrate , a uniform thin film with controllable layer thickness can be deposited onto planar substrates. Thanks to its rapid, highly reproducible thin film deposition properties, spin coating is commonly used in scientific research for material and device investigations. The thickness of spin coated thin films can be well controlled via the spinning speed and ink viscosity [60]. However, although all these coating methods typically result in uniformly thin films, additional mask or patterning methods are typically required.

On the other hand, printing methods provide the intrinsic patterning during thin film deposition and efficient material utilization. Through Gravure printing, the thin films are deposited via mechanical contact between the substrates and pre-patterned metallic rolls. Gravure printing has great advantages in high speed and high throughput roll-to-roll manufacturing as it can achieve maximum print speed of 1000 m/min with resolution down to 20 μm [61]. It is of particular interest for large area OLED-based lighting applications, where the cost per printed unit is a core issue. Screen printing is another contact printing method, where the ink is transferred by squeezing through patterned mesh onto target substrates. It is one of the most inexpensive and fast methods for organic layer deposition. However, the typical minimum thickness of 0.5 μm prevents it from depositing OLED thin layer stacks [62,63]. Moreover, the necessary of mesh mask in screen printing and metallic

rolls in Gravure printing for each design increase the initial cost and are not suitable for customized disposable point-of-care applications.

In contrast, inkjet printing is a digital, non-contact solution deposition technique. There are two types of popular commercially used inkjet printers: continuous inkjet printer [64–66] and drop-on-demand (DoD) inkjet printer [67,68]. The continuous inkjet printers are mainly used for commercial marking and coding on products and packages. DoD inkjet printers, specifically piezoelectric DoD inkjet printers, are selected and intensively investigated for organic electronic fabrications. A continuous inkjet printer consists of a fluid reservoir, one or more ejecting nozzles and charged plates. The fluid reservoir supplies the ink into the nozzles that eject continuous droplets. The ejected droplets are then deflected by charged plates so that they can be deposited on desired positions. Contrastingly, a DoD inkjet printer is working with low fluid impedance nozzles and controllable actuators (thermal or piezoelectric). By generating pressure pulses from actuators, the ink is ejected out of nozzles due to actuator shape deformation. In the meantime, high mechanical precision arises in both x- and y-directions for directing the printhead to the desired positions.

The piezoelectric DoD inkjet printing technique has the most control over the precision of printed patterned without using any masks. In addition, the non-contact deposition ability of inkjet printing results in minimized contamination. In industrial printheads, thin films with complex patterns can be printed under high speeds onto large area flexible substrates with thousands of nozzles and under high frequencies. All these make inkjet printing as the most cost-efficient solution deposition technique for organic electronics [69–71]. Aside from the great success in printing commercial image and characters in the 20th century, the inkjet printing method has been intensively researched to fabricate various organic and printed electronic applications including Radio-frequency identification (RFID) antennas [72,73], OLEDs [70,74,75], organic photodiodes (OPDs) [76], Organic photovoltaics (OPVs) [77,78], and Organic field-effect transistors (OFETs) [49,79]. Nevertheless, large challenges remain for depositing thin films with high uniformity via inkjet printing on planar substrates. One major issue is the intrinsic solvent evaporation phenomenon such as coffee ring effect [80].

2.2 Organic light-emitting diode (OLED)

Organic electroluminance was first discovered in 1960s from single crystals of anthracene [81]. However, there is no applications had been recorded because of the high working voltages till the discovery of efficient and low-voltage OLEDs from Kodak researchers in 1987 [82]. The OLED was based on multi-layer sandwich p-n heterojunction. With proper design, electrons and holes can efficiently inject into emitting layer 8-hydroxyquinoline aluminum (Alq$_3$) and emit light. A brightness of > 1000 cd/m^2 was emitted under less than 10 V. Since then, OLEDs have been tremendously investigated and produced fruitful achievements. OLEDs provide the advantages of self-emitting property, high efficiency, full-visible color capability, wide viewing angle, high contract, low power consumption, lightweight, large area and flexibility. The particular traits of producing on large and flexible substrates as well as easy color tuning demonstrate high competing ability compared to conventional display and lighting techniques such as liquid crystal display (LCD), thin film transistor liquid crystal display (TFT-LCD), and light emitting diode (LED). All these properties make this device especially advantageous for display area and offers promising applications in lighting. For example, smartphones with active matrix OLEDs displays have become a dominant player in the market in recent years, especially in the field of high-end smartphones [23]. The curved OLED display of Samsung Galaxy Edge series, which present the unique flexible properties of OLEDs in contrast to its competitors, has drawn large attention and unexpected success in the market [83]. High-end dominator Apple also integrated OLED display in its products such as iWatch and MacBook Pro. Increasingly, manufacturers are focused on developing big area and curved OLED TVs. LG electronics has already released several OLED products in the market and is even working on rollable OLED TVs in 2017 [84]. In the field of lighting, Audi is delivering new model of Audi TT with integrating OSRAM OLED taillights in 2016 [85].

Similar to the inorganic LEDs, a basic OLED structure consists of an emissive layer sandwiched by two electrodes (see Figure 2-1). At least one of the electrodes should be transparent so that the light can out-couple from the device. A reflective metal such as Al or Ag is typically used as the other electrode for high electrical conductivity and improving the emission brightness. For simplicity, this three-layer structure is used to explain the working mechanism of OLEDs. The electrical conductivity of semi-conductive small molecules and polymers comes from the delocalization of π electrons from the extended π bonding over the complete molecule [86]. The highest occupied molecular orbital

(HOMO) and the lowest unoccupied molecular orbital (LUMO) of organic semiconductors behave similarly to the conducting band and valence band of inorganic semiconductors. The radiative decay of excitons inside the emissive layer (EML) from LUMO to HOMO emits photons and thus emits light. There are two main types of organic electroluminescent materials: small molecules [82,87] and polymers [88,89]. One major difference between them is the thin film deposition process. Small molecule based EML is generally deposited by thermal evaporation under high vacuum, while the polymer-based EML is processed from solution-based processing techniques as previously mentioned in section 2.1. Generally, the former is a mature industrial technology with higher efficiencies and longer lifetimes due to the high material purities, ideal multilayer stack and high degree of horizontal molecular orientation, whereas the latter benefits from low production costs and can process over large, flexible substrates due to a better mechanical integration into roll-to-roll manufacturing.
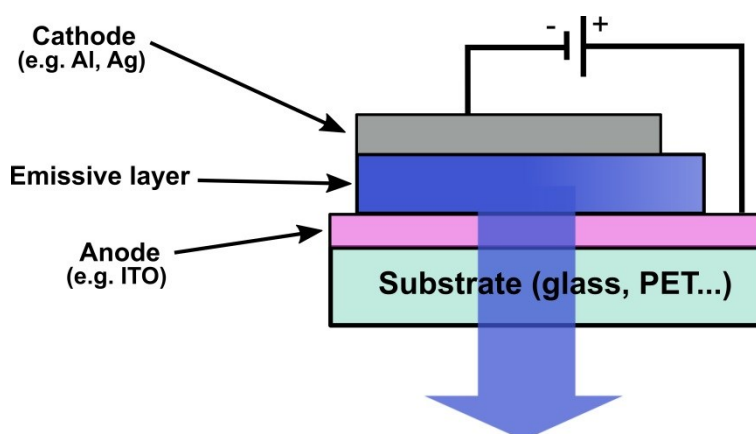
Figure 2-1 Schematic diagram of a simple sandwiched three-layer OLED structure on a transparent substrate. It consists of a transparent anode such as ITO, an organic emissive layer (a blue light emission is illustrated here), and a reflective cathode such as Al or Ag.

The energy diagram of a basic OLED structure is illustrated in Figure 2-2. Under positive electrical potential bias, electrons inject into the HOMO of the organic emissive layer from the cathode, and holes inject into the LUMO from the anode. The external electrical field also drives the injected electrons and holes diffuse toward each other within the EML. It has been reported that the current of OLEDs is determined by the mobility of the charge carriers, which means the current is space-charge limited [90,91]. When a pair of injected electrons and holes meets, they form an exciton. The exciton will either radically

relax via fluorescent or phosphorescent decay, and consequently a photon will be emitted resulting in light emission.

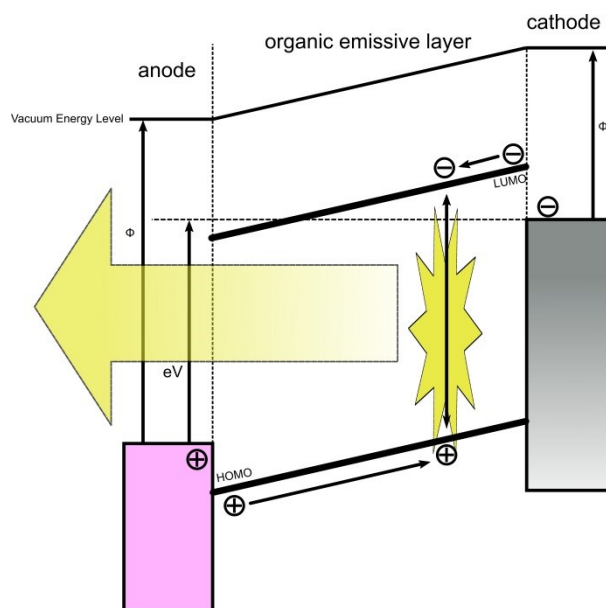Figure 2-2 Energy level diagram of a single-layer OLED with an applied positive bias. A yellow light emission is illustrated here.

As illustrated in Figure 2-3, in order to achieve high efficiency of OLEDs, multi-layer system is usually used [92,93]. Typically, the layer structure of high efficient OLEDs consists of a transparent anode, hole injection layer (HIL), hole transporting layer (HTL), electron blocking layer (EBL), emissive layer (EML), hole blocking layer (HBL), electron transporting layer (ETL), electron injection layer (EIL), and metal cathode. They have two main functionalities: 1) Adapt the energy band mismatch in order to improve the carrier injection and reduce the driving electrical potential; 2) balance and confine the injected carriers inside EML in order to maximize the recombination efficiency (γ). Depending on the energy level of the emitters, sometimes one material can provide the functionalities of two adjacent layers. For example, the hole-transporting and conductive polymer PEDOT:PSS is widely used as both hole-injection and transporting layers. The increasing conductivity of PEDOT:PSS allows for its development and implementation into a transparent electrode [94,95]. The first functionality is normally achieved via choosing appropriate materials to adapt the work function level layer by layer. The second functionality involves using the large work function mismatch for opposite carriers to prevent the carrier from escaping to the opposite electrode. For example, as indicated in Figure 2-3, there is a big work function barrier between LUMO (HOMO) level of EML and EBL (HBL) so that

the electrons (holes) cannot escape easily from the EML. Thus, the all injected electrons and holes have large possibilities to combine and emit light.
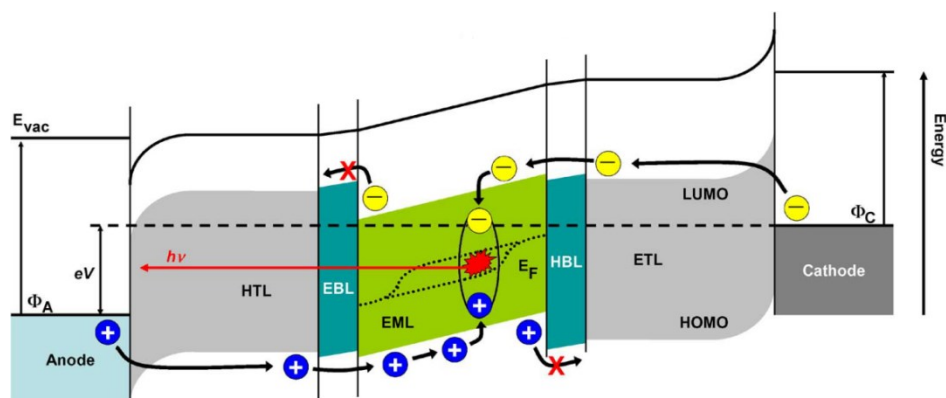

Figure 2-3 Energy level diagram and functionality of a p-i-n OLED, copyright (2009) IEEE, reprinted from literature with permission [93].

Currently, all commercialized OLED products are based on sputtered and pre-patterned ITO substrates. The rest of the layers such as EML, low work-function EILs (e.g. Ba, Mg, LiF), and reflective metal cathodes (e.g. Al, Ag) are deposited by the thermal evaporation method. This manufacturing technique brings outstanding thin film thickness control as well as surface uniformity, and therefore high device performance. However, this technique is costly because of high vacuum requirements, expensive fine metal masks, slow manufacturing speed, and material wasting [50]. Moreover, it has limited production abilities on large area OLED manufacturing [45]. Consequently, researchers have focused on replacing vapor evaporation-based method with solution-based deposition methods [46].

Three major issues have to be resolved for fully solution-processed OLEDs. Firstly, finding soluble materials for work-function adaptation layers such as EIL, ETL, HBL, and EBL, as depicted in Figure 2-3. At current stages, it is difficult to achieve both the target work function and high carrier mobility (or high electrical conductivity) via single material. Therefore, ultrathin layers (typically, 1–10 nm) of reactive materials such as LiF, Ba, and Mg are typically used to minimize the influence of electrical conductivity issues. Secondly, intermixing of layers is another outstanding issue for fully solution-processed multi-layer OLEDs. The solvent from the above layers can dissolve the layer deposited underneath. Hence, either cross-linkable materials or orthogonal solvent systems for adjacent layers have to be selected and processed. Finally yet importantly, ultrathin and homogeneous lay-ers are difficult for mask-free solution-processing methods such as printing methods. In

conclusion, fully or partly solution-processed OLEDs typically use much simpler layer structures and thicker layers. To achieve this, finding materials with high carrier mobility, appropriate work function, air stability, and solution-processing ability is imperative.

For most reported "fully" solution-processed OLEDs, a transparent pre-patterned ITO anode, thermally evaporated metal cathodes such as Al and Ag, and thermally evaporated EIL such as Ca, Mg, LiF are still used [46]. When it comes to inkjet printing, by far no all-inkjet-printed OLED has been reported in the literature regardless tremendous efforts on inkjet printing OLEDs. The most recently reported inkjet-printed OLEDs were only one or two layer inkjet printed such as EML [55,75,96], HTL [97], HTL + EML [98], and Ag cathode [29]. Today, large efforts are still focusing on fully solution-processing OLEDs using advantages of different solution-processing methods [99,100]. However, ITO anode and / or evaporated metal cathode(s) are still indispensable. For example, Hermerschmidt et al [101] reported a solution-processed OLEDs with an inkjet printed Ag grid, doctor-bladed PEDOT:PSS HTL, and doctor-bladed EML. However, the EIL (Ca) and cathode (Al) were still evaporated under high vacuum. A maximum brightness of > 6000 cd/m² and current efficiency of 1.34 cd/A can be achieved. Stolz et al [29] reported a solution-processed yellow OLED with a ITO anode, spin-coated PEDOT:PSS HTL, SuperYellow LEP, PFN EIL, and an inkjet printed Ag cathode. A maximum brightness of ~3000 cd/m² could be achieved. However, a very short maximum lifetime (LT70) of 4 h at 500 cd/m² resulted with an evaporated Ag cathode.

Zhou et al [102] introduce the air stable and solution-processable polymer containing simple aliphatic amine groups, such as polyethylenimine ethoxylated (PEIE) and branched polyethylenimine (PEI) as an universal, solution-processable EIL. The mechanism is the modification of interface work function via presence of the interfacial dipole from amine groups. The ultrathin layer (1−10 nm) can reduce the work function of various widely used OLED materials such as Al, Ag, ZnO, ITO and PEDOT:PSS. Since then, a great tool has become available to fully solution process high efficient OLEDs [24–30]. Recently, a first fully solution-processed OLEDs with a layer structure of PEDOT:PSS ‖ ZnO ‖ PEI ‖ EML ‖ WO$_3$ ‖ PEDOT:PSS + AgNW using solely the spin-coating method with adhesive tapes for patterning has been reported [24]. High efficiencies of 20.1 and 2.5 cd/A as well as maximum luminance of 4220 and 500 cd/m² has been achieved for yellow and blue fluorescent OLEDs. Even though, ultra-thin layer of PEI is still required, and high layer surface homogeneities are also required for high device performance. In an

effort to address this, Kaçar et al [103] reported a novel way to produce bright RGB OLEDs using a spin-coated ZnO:PEI nano-composite interfacial layer. Maximum brightnesses of ~12 000 cd/m² can be achieved for RGB OLEDs. However, all devices were dead immediately after achieving the maximum brightness. Furthermore, with exception to the EMLs that were spin-coated, the ITO anode, evaporated ultrathin HIL, and evaporated Al cathode were still used in this study. It can be concluded that no real fully solution-processed OLED using the inkjet printing technique as the exclusive electrode patterning method has been reported. There is no lifetime investigation of solution-processed OLEDs at high emission brightness (> 3000 cd/m²). The performance of solution-processed OLEDs reduced as more layers were inkjet printed.

2.3   Organic light-emitting electrochemical cell (OLEC)

Thanks to the pioneering work of Pei and co-workers [35], the light-emitting electrochemical cells were first introduced in 1995. They used a conjugated polymer (CP) as a light-emitting material–a combination of a lithium salt and a solid electrolyte as the mobile ion source for *in situ* doping. It is also commonly referred to polymer light-emitting electrochemical cells (PLEC) due to the emissive polymer. A year later Lee et al [104] reported that a LEC device can be also fabricated from a single component active material (i.e. an ionic transition metal complex, short for iTMC), which combines the light-emitting organic material and the mobile ions into one material. This introduced another dominant LEC component principle: iTMC-LEC. In spite of the claims of iTMC-LEC, an additional electrolyte, usually an ionic liquid, has to be added to reduce the turn-on time.

The principle of the OLEC operation is quite similar to OLEDs. It is also based on the sandwiched thin layer structure of heterojunctions. The injected electrons from the cathode and holes from the anode drift inside active layer meet each other, combining and forming excitons. Excitons partly undergo radiative decay and emit photons. However, OLEC has a slightly varied operation process due to the presence of mobile ions. The typically used organic light-emitting materials are undoped at their pristine state. Therefore, when an external electrical potential is applied between the anode and cathode, the ions which are pre-mixed inside active layer, drift towards the counter electrodes and form electric double layers (EDLs) at both electrodes (Figure 2-4a). The EDL has a typical thickness of less than 1 nm; the local electric field can be therefore as high as 10^9 V/m. High electric

field leads to high energy level bending at the electrode / active material interface. Once the applied external electric potential is higher than the energy gap of the active material, i.e. $V > E_g/e$, a large bent in the interfacial energy bands results in allowing electrons as well as holes to inject into active organic material via tunneling (Figure 2-4b). Electrons inject into LUMO layer and holes inject into HOMO layer of the organic active material. Consequently, the organic active material will be electrochemically doped because of injected space charges, which drives the surrounding mobile ions to diffuse further and neutralize the injected space charges. A cation compensates an injected electron and forms an n-type dopant, while an anion compensates an injected hole and forms a p-type dopant. Similar to inorganic semiconductor doping, the formed space dopants dramatically increase the electrical conductivity of organic active material [105]. The two doped-regions approach each other over time and eventually meet, which results in an organic p-n junction. Injected electrons and holes partly combine at the junction interface and form excitons. Some of generated excitons emit photons via radiative decay (Figure 2-4c).
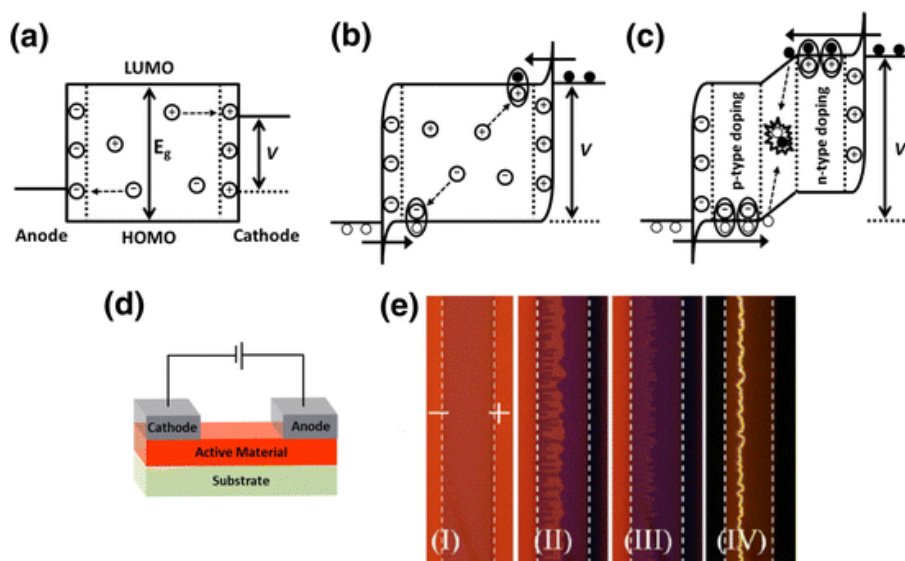
Figure 2-4 Energy-level presentation of the transient response at (a) $V < E_g/e$ and (b) $V = E_g/e$, as well as (c) the steady-state operation at $V > E_g/e$; the larger circles represent the ions, the small open circles represent the holes, and the small solid circles represent the electrons; (d) a schematic structure of an open surface cell device; (e) a set of time-lapse photographs depicting the turn-on process in a surface-cell device, where the emergence of dark areas corresponds to the formation of doped regions, copyright (2008) Elsevier B. V, reprint with permission from literature [36].

Thanks to the *in situ* doping principle, a relatively thick active layer can be used in OLECs, and OLEC can work in principle with a simple 3-layer structure of an anode, an active layer, and a cathode. It has been demonstrated that OLECs can work with > 10 mm

thick active layer [106], and therefore a planar device structure can be used to study the dynamic doping behavior of OLECs, as depicted in Figure 2-4d and e. The intrinsic LEP emit strong fluorescent light under UV irradiation, while this ability is quenched after electrochemical doping (see Figure 2-4e II and III). Thus, the N- and P-doping fronts can be optically observed under microscopes or high resolution cameras with UV irradiation. The light-emitting regions are also visible due to the electroluminance of LEPs (see Figure 2-4e IV). The planar structure has been a powerful tool to understand the mechanism of OLECs [107–109]. The influence of the dopant materials [110], dopant concentrations [111], LEPs [112], electrolytes [113,114], voltage biases [115], and electrodes [116] were investigated separately. On the other hand, the *in situ* electrochemical doping also results in long turn-on times, lower the emission efficiency/brightness, and shorten operational lifetime. OLECs have a typical lifetime of ~100 h at the brightness level of ~100 cd/m² [128], a typical turn-on time of a few minutes to hours, and a typical efficiency of ~10 cd/A [36].

Compared to OLEDs, most reported OLECs were partly solution-processed, and the most common used methods were spin-coating [35], slot-die coating [117], spray coating [118], gravure printing [119], and inkjet printing [120,121]. Even OLEC demonstrates high potential in fully solution-processing, an ITO anode and air-stable metal cathodes (Al, Ag and Au) were still used in most reported OLECs. Matyba et al [122] reports a metal-free and ITO-free OLECs by using PEDOT:PSS as an anode and Graphene as a cathode. A maximum emission brightness of 1200 cd/m² was achieved under 20 V bias. A fully solution-processed OLEC was reported by Liang et al [123]. The OLEC consisted of an anode from a rod-coated SWCNT/AgNW bilayer, a spin-coated/doctor-bladed active layer, and a doctor-bladed Ag cathode. A maximum brightness of 2080 cd/m² was achieved. It has been noticed that by a maximum brightness of 14 600 cd/m² was achieved by replacing Ag paste with evaporated Al cathode. Thus, device performance highly decreases with solution-processed layers. Another fully solution-processed OLEC was fabricated on a pre-coated paper via spray coating [124]. Due to the rough surfaces, up to 7 μm thicknesses of OLEC active layers and PEDOT/AgNW electrodes were used. Although it emitted a maximum brightness of 250 cd/m², it proved OLEC work with rough substrates and a 7.6 μm active thickness. Moreover, OLECs worked on curved and uneven substrates such as on stainless steel fibers via dip coating [125] and on textiles via spray coating [126]. However, both were not fully solution-processed.

2.4 Integrating OLEDs/OLECs in on-chip fluorescence sensing

Microfluidic Lab-on-a-chip (LoC) systems are widely used in chemistry, biology and medicine since they provide full sample analysis without the need for bulky and expensive laboratory equipment [127,128]. They provide short measurement times by requiring very low amounts of analyte. Through the use of cost-efficient replicated polymer chips and solution processing for the integrated functionalities, LoCs are disposable and suitable for point-of-care applications [129]. Within the last years, much effort has been devoted to increasing the degree of integration at reasonable costs and therefore the number and complexity of possible application cases via integrating multi-functionalities as well as bio-sensors onto microfluidic chips [3–5]. Some examples include: On-chip integrated micro-pumps integrated by fully inkjet-printed piezoelectric membrane pumps [6,7] for driving the fluid with analytes through micro-channels; inkjet-printed micro-heaters [8,9,130] integrated to achieve thermal control for analysis; inkjet-printed SERS pads integrated to increase Raman signals [131]. The analyte mixing and separating can be digitally controlled by inkjet-printed digital microfluidics [132,133]; even micro-channels can be directly printed on paper [134,135].

Fluorescence sensing is the most common analytical and diagnostic method in biological and medical applications because of its high sensitivity and selectivity properties [10,11]. However, very few examples of fully integrated, compact, and low-cost fluorescence sensing systems on microfluidic chips can be found. This is mostly because of widely used sensing units based on LASERs, LEDs, CCDs, and silicon photodiodes. These devices have relatively large dimensions, are relatively expensive and can only be integrated by means of assembly [12]. In contrast, organic electronics provide the advantages of direct on-chip integration, low-cost manufacturing via solution processing (e.g. inkjet printing, spin-coating), easy emission and detection wavelength tuning, and compatibility with flexible substrates [136]. Consequently, several integrated organic light-emitting diodes (OLEDs) in fluorescence sensing systems have been reported in recent years [17,18,137–141]. For example, Pais et al [137] reported a fluorescence sensor with a combination of an all-evaporated green OLED, an evaporated OPD and two linear polarization filters. A limit-of-detection (at S/N = 1) of 100 nM was projected for Rhodamine 6G, and 10 μM for fluorescein. Lefèvre et al [139] reported a Algal fluorescence sensor integrated into a microfluidic chip for water pollutant detection. Color filters based on acid/base dyes and a metal complex were used in this study. Concentrations of Diuron as low as 7.5 nM have

been tested and achieved for water pollution sensing. Similar to the previous case, an all-evaporated blue OLED was used as the excitation light source. When combined with high sensitive traditional photodetectors such as CCDs, spectrometers, and Photomultiplier tubes (PMT), partly solution-processed OLEDs were integrated in microfluidic chips as excitation light sources. Hofmann et al [142] and Scholer et al [141] both reported using polymer OLEDs with spin-coated HTL and EML, despite using slightly different emitters. The yellow OLEDs can emit a maximum brightness of 50 000 cd/m² and detect a concentration of urinary human serum albumin (HSA) as low as 10 mg/L.

There is no OLEC used as an excitation light source for fluorescence sensing applications. This is mainly due to the long turn-on time and relatively low maximum brightness of OLECs. However, OLECs show high potential in disposable applications due to the consistency of device architecture and manufacturing process; no modification is required for different emission wavelengths, i.e. colors, of different fluorescent dyes except changing of the light-emitting polymers or small molecules.

In conclusion, recently reported OLEDs used in on-chip sensing applications were manufactured either fully or partly by thermal evaporation in a high vacuum. No fully solution-processed OLEDs have been reported for on-chip fluorescence sensing applications. Furthermore, OLECs have never been connected with fluorescence sensing area.

3 Theoretical principle of using organic light sources for sensing applications

In this Chapter, theoretical concepts and a model of organic light-emitting devices have been formulated to provide a guideline of using organic light-emitting devices for on-chip fluorescence sensing applications. For OLEDs research and industries, displays and lighting are main application fields. Thus, several aspects of organic light-emitting devices are being intensively explored, including the improvement of light-emitting efficiency and reduction of driving voltages for energy saving, extending continuous operational lifetime at relatively low brightness ($\leq$ 1000 cd/m^2) for long term usage, covering RGB color for display application, and realizing white color emission for daily lighting application. However, in order to use organic light sources as excitation light sources for disposable microfluidic LoC sensing application, the following requirements are defined:

1)   *Suitable excitation light wavelengths to excite specific fluorescent dyes for sensing;*
2)   *high emission brightness to achieve appropriate sensitivity;*
3)   *reasonable operational lifetime at relative high brightness;*
4)   *good compatibility and integration ability on sensing chips;*
5)   *low manufacturing costs;*
6)   *stable and commercially available materials*

In this chapter, section 3.1 and 3.2 discusses the material selection to meet requirements (1) and (6). For requirement (5), solution-processing techniques are used in this dissertation to manufacture the organic light sources. More specifically, inkjet printing is used to realize direct integration and electrode patterning, and spin coating is selected to deposit homogenous active layers. The intrinsic properties of organic light sources combining with solution-processing techniques fulfill requirement (4). The details are discussed in section 3.1. The rest of this chapter focuses on the development of a necessary theoretical model for generating high brightness (in section 3.3) and reasonable operation lifetime (in section 3.4) for using organic light sources in on-chip fluorescence sensing applications.

3.1 Device architecture considerations

Device architecture considerations: two slightly different variants of organic light emitting devices are chosen here for targeted microfluidic LoC sensing applications. They are OLECs and OLEDs. Although both devices can be manufactured via cost-efficient solution process techniques and are compatible on various LoC substrates, they differ in the layer architecture and thicknesses.

Due to the dynamic doping mechanism of OLECs and thus improved electrical conductivity of active layers, OLECs have much higher tolerance on surface roughness then OLEDs. For the same reason, OLECs are insensitive to work function mismatch and have a "universal" three-layer structure for all visible emission light. With fewer layers and universal structures, the manufacturing cost is further reduced. Consequently, OLEC are proposed here to be a general cost-efficient solution for integrating organic light sources on microfluidic LoC systems. They show particular advantages of integrating on rough and flexible polymeric chips and blue emitters that have high carrier injection barriers.

On the other hand, OLEDs have much higher efficiency and emission brightness than OLEC. Therefore, OLEDs have higher potential in applications requires high sensitivity, especially when the chips have high surface flatness or with additional planarization layers. A slight modification of layer structures or interlayer material could be necessary to avoid unbalanced injected carriers. This is particularly important for achieving high emission efficiency and brightness (see section 3.3). To reduce the complexity of solution-processing multi-interlayers, a one-step, inkjet printable work function adaptation layer is introduced, and detail is described in section 4.1.2.

For scientific investigation purposes, a pre-patterned ITO electrode is chosen as the cathode and active layer is spin-coated instead of printed so that reproducible and highly controllable samples can be deeply investigated and compared. The ITO-free devices will be introduced in chapter 5.3, 6.2, and 7.1. PEDOT:PSS is chosen as the anode because of its high hole-injection ability, good electrical conductivity, air stability, high transparency as well as good inkjet printability. Most commercial PEDOT:PSS inks are water / alcohol based inks so that the interlayer-dissolving problem can be avoided, which is a typical issue for solution-processing multi-layer OLEDs. More information about the materials is present in the section 3.2. Furthermore, there is commercially available ink that embedded

silver nanowires (AgNW) into PEDOT:PSS solution. Thus, the printed thin film results in much higher conductivity of ~3000 S/m while remains high optical transparency of > 90%.

In summary, OLECs are proposed in this dissertation as a universal cost efficient solution to integrate organic light sources on microfluidic LoC systems. OLEDs with a one-step work function adaptation layer are proposed to be an alternative solution for higher detection sensitivity, in particular with low bandgap emitters such as yellow and green as well as on chips with high surface flatness. The investigated device architecture is: a) pre-patterned ITO as cathode; b) inkjet printable work function adaptation interlayer for OLEDs; c) spin-coated active layer; d) inkjet-printed transparent PEDOT:PSS layer as anode. For the final application, the ITO electrode can be replaced by a printed Ag, PEDOT:PSS or PEDOT:PSS & ZnO bilayer.

3.2 Material selection

In this section, the materials used in this dissertation for device manufacturing and demonstration have been discussed. Their chemical structures are illustrated in Figure 3-1.
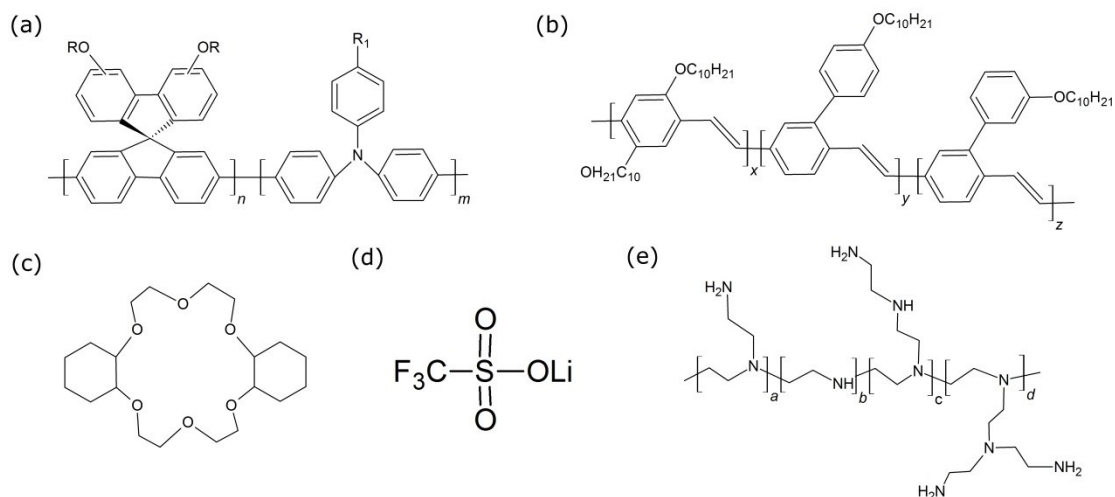

Figure 3-1 General chemical structure of materials used in light emitting layer and interlayers in this dissertation: (a) blue LEP Merck Blue (SPB-02T); (b) yellow LEP SuperYellow (PDY-132); (c) solid electrolyte DCH18C6; (d) metal salt $LiCF_3SO_3$; (e) work-function adaptation polymer PEI.

Light-emitting materials and dopants: For OLECs, according to section 2.3, although iTMC-LEC materials have much higher intrinsic efficiencies, most materials are still under development, devices shown still possess a low maximum brightness, and long

turn-on time [143]. Furthermore, due to a great deal of research in solution-processing polymer OLEDs, wide light-emitting wavelength coverage and commercially available LEPs are accessible in the market. As additional ionic donors and ionic solid electrolytes are needed for realizing doping of LECs, polymer-based LECs also provide the engineering flexibility by tuning the dopant materials and mass ratios (i.e. dopant concentrations). For the above reasons, polymer-based OLECs are chosen as an excitation light source for disposable on-chip fluorescence sensing applications. As mentioned in section 2.4, blue light is selected for functional demonstration for the reason that it is widely used in fluorescence sensing applications and more difficult to produce efficient OLEDs. Furthermore, for light emission within the visible spectrum, LEPs which has blue light emitting ($\lambda = 400 - 500$ nm) has the largest energy gap and therefore the largest work-function mismatch. Therefore, it is expected that the recipe can be transferred to other colors such as yellow, green and red with minor modifications.

For OLEDs, polymer based LEPs are chosen for the similar reason as OLECs. Although small molecule based LEPs have higher intrinsic quantum efficiency, they are still mainly deposited via vacuum-based thermal evaporation process. The reason is the intrinsic low solvent solubility and poor film formation ability via solution-processing techniques. Moreover, most small molecule base LEPs are much more instable under ambient conditions than polymer based LEPs, which increases the complexity and cost of the manufacturing processes.

The blue light-emitting polymer (product name: SPB-02T, general name: Merck Blue) is used in this dissertation to fabricate blue OLECs. It was purchased from Merck KGaA. As it is a commercial product, the detailed information is not available to the public. It is, in general, a poly-spirobifluorene copolymer (see Figure 3-1a). It has good thermal stability with glass transition temperature of 210 °C. The number average molecular weight (M_n), the weight average molecular weight (M_w) and Polydispersity index (PDI) of used polymer batch is 83 kg/mol, 308 kg/mol, and 3.7, respectively. This shows good solution-processing ability such as inkjet printing and spin-coating. The main reasons for choosing this polymer for research are: 1) electroluminescent wavelength is blue range (peak wavelength 480 nm), which is widely used in fluorescence sensing applications; 2) good solution-processing ability; 3) good thermal stability; 4) good air stability; 5) commercially available.

In additional, a yellow light emitting polymer (product name: PDY-132, general name: SuperYellow) was used for manufacturing fully solution-processed yellow OLEDs as well as OLECs. The polymers were received from Merck KGaA and has a molecular weight of Mw = 1 700 000 g/mol and M_n = 350 000 g/mol. The chemical structure is depicted in Figure 3-1b. The SuperYellow polymer was widely used in OLEC and OLED researches [26,144–149]. It has relatively high light-emitting efficiency, is chemically stable in air and easily solution processable. It has also good thermal stability as it can be annealed up to 200 °C [144].

The dopant mixtures used in this dissertation are salt Lithium trifluoromethanesulfonate ($LiCF_3SO_3$) as an ionic dopants and crown ether dicyclohexano-18-crown-6 (DCH18C6) as the solid electrolyte, which provides the ionic mobility for the salt. The chemical structure is illustrated in Figure 3-1c and d. They were both purchased from Sigma-Aldrich Corporation (Merck KGaA). The lithium salt was chosen as the ionic dopant is mainly due to its wide use in light emitting electrochemical cells research society since the first introduce by Pei [35,150] and long history of the lithium battery. It showed good electrochemical doping capabilities in the lithium battery. Two reasons to select DCH18C6 as the solid electrolyte: one is because it has good solubility in non-polar solvents, which is widely used solvents for solution processing of OLEDs, in particular inkjet printing; the other is that it shows high ionic conductivity at elevated temperature (> 60 °C) while low ionic conductivity at room temperature, which provides controls on doping profiles such as frozen P-N junction at room temperature [151]. Therefore, fast turn-on can be achieved, which is indispensable for on-chip fluorescence sensing applications.

Conductive materials: Besides the light-emitting organic materials, the conductive materials are required for depositing the electrodes and wiring. For sandwich structure light-emitting devices, at least one of the electrodes should be transparent so that the generated photons can escape from the LEP. Indium Tin Oxide (ITO) is predominantly used in OLED research and industrial as a transparent anode [152]. ITO has good transparency in the visible wavelength (> 90%) range and good conductivity (~ 5 000 – 6 200 S/cm [153]). It is mainly used as an electrode in this dissertation for scientific comparison. Because of OLEC's high tolerance toward work-function mismatch, it functions as a cathode instead of an anode. Patterned ITO on glass substrates with 6 and 8 pixels were purchased from Ossila Ltd.. Transparent conductive polymer PEDOT:PSS is mainly used for as an anode in this dissertation. It has been reported that even with much lower conductivity, OLEDs

using PEDOT:PSS as the anode instead of ITO shows slightly higher efficiency [154]. Inkjet printable PEDOT:PSS inks (Clevios P JET HC V2 and 700N) and silver-nanowire-embedded PEDOT:PSS (Clevios HY JET) were purchased from Heraeus Clevios GmbH. They were filtered through 0.2 μm-pore-size PP-membrane syringe filter before using. PEDOT:PSS P JET HC V2 ink shows slightly higher work function than PEDET:PSS P JET 700N, which is better option for the anode. However, PEDOT:PSS 700N is not acidic solution like HC V2 ink, so it shows better stability. Printed PEDOT:PSS thin films from Clevios HY JET ink had conductivity of ~2700 S/cm, which is much higher than normal PEDOT:PSS inks (both HC V2 and 700N, ~500 S/cm). Unfortunately, this ink is still under development and not stable. In some OLEC and OLED samples, silver nanoparticle dispersion (Cabot CCI-300, purchased from Cabot Printed Electronic Materials) or Suntronic EMD5603 inkjet-printable silver nanoparticle dispersion (20 w%, purchased from Sun Chemical Corporation) was inkjet printed as conductive wiring, reflective cathode, and / or reflective mirror. The ink was filtered through 0.2 μm-pore-size PP-membrane syringe filter before using.

Work-function adaptation materials: In some devices, the ZnO interlayer was integrated between cathode and active layer to improve the electron injection. Two different methods were used in this dissertation to deposit ZnO interlayer: A ZnO precursor and a Al-doped ZnO nanoparticle dispersion.

For some blue OLECs, the ZnO layer was deposited from a ZnO precursor ($Zn(acac)_2$) solution. $Zn(acac)_2$ hydrate powder was purchased from Sigma-Aldrich Corporation (Merck KGaA). The ZnO precursor solution was prepare from dissolving $Zn(acac)_2$ hydrate powder in ethanol with a volume concentration of 20 mg/mL. The dispersion was constant stirred at 400 RPM and heated at 60 °C on a hot plate. The ZnO layer can be generated and crystallized by annealing $Zn(acac)_2$ thin film at elevated temperature (120 °C was used here) at ambient conditions. The mechanism is thermal decomposition with water, as reported from Arii et al [155]. For yellow OLEDs, an Al-doped ZnO nanoparticle dispersion dissolved in 2-propanol / propylene glycol mixture, which was purchased from Nanograde Ltd (Nanograde N-21X-Slot), was inkjet printed to deposit the Al:ZnO interlayer. The ink has a solid content of 2.5 wt% and ZnO is doped with 3.15 mol% Al. The mean nanoparticle size is 12 nm. The ink has a viscosity of 3.1 mPa·s, which is in the good range for inkjet printing from DMC printheads. After printing, the thin film was thermal annealed at 150 °C for 30 min on a hot plate.

Thanks to the good work-function reduction of PEI (chemical structure in Figure 3-1e) on various materials, it was also used to further reduce the work function mismatch and improve the electron injection of solution-processed yellow OLEDs. A novel approach is introduced here to mix PEI with Al-doped ZnO nanoparticle dispersion so that a 0.5wt% PEI is dissolved in the dispersion. Thus, single work function adaptation layer with ZnO and PEI mixture can be direct inkjet printed.

Encapsulation materials: Although the LEPs used here are relatively stable in air and can be processed at ambient conditions, oxygen and moisture lead to serious degradation during the electrical operation, in particular when UV light is present [156–158]. Thus, at the last step, the processed OLEDs/OLECs have to be encapsulated in inert atmosphere or shortly after vacuum process. UV curable encapsulation epoxy from Ossila Ltd with glass coverslip was used as the device encapsulation. This encapsulation method has been reported to be sufficient not only for organic electronics [159] but also for OLECs [160].

3.3 Theoretical model of improving emission brightness

Similar to the inorganic light-emitting diodes, the physic mechanism of light-emitting of OLEDs/OLECs is spontaneous recombination of electron-hole pairs and simultaneous emission of photons. Following the law of conservation of energy and momentum, the emitted photon energy is given by the difference between the electron energies of holes and electrons, which are typically the HOMO (E_{HOMO}) and LUMO (E_{LUMO}) energy, i.e.:

$$hv = \frac{hc}{\lambda} = E_{LUMO} - E_{HOMO} \approx E_g \qquad (3.1)$$

For the simplified simulation, the peak emission wavelength is approximately equal to the bandgap energy of light-emitting organic materials (LEPs, in this dissertation). Table 1 lists some examples of commercially available LEPs. With broad light-emission spectra, the four LEPs almost cover the completely visible light range, i.e. from 400 to 700 nm. The relationship between emission colors and bandgap energies fits the equation (3.1) well. PEDOT:PSS is widely used as a hole-transporting layer or anode, and it has a work function of ~5.2 eV. Thus, PEDOT:PSS has relatively low hole injection barrier into RGB LEPs, because typical LEPs has HOMO level between 5.0 and 5.8 eV, which means maximum hole injection barrier of 0.6 eV. In contrast, the common air-stable cathodes of OLEDs have work function around 4.3-4.6 eV such as Al and Ag. The electron injection

barrier can be as high as 1.8-2.1 eV in case of a blue LEP. That is one important reason why blue OLED has lowest efficiency among the visible colors. As described in section 2.2, highly reactive metals such as Ba or ultrathin EILs such as LiF and PEI are typically used in modern OLEDs to balance the electron-hole recombination. In this dissertation, two different solution-processed approaches will be used to improve the electron injection efficiency: 1) the *in situ* generated p-n junction via electrochemical doping; 2) a one-step, inkjet-printed EIL via Al-doped ZnO nanoparticles and PEI mixture. Therefore, relatively efficient organic light sources can be fully solution processed.

Table 1 Photo-physics parameters of some commercial-available RGB LEPs.

LEPs	Emission color	LUMO level	HOMO level	Bandgap energy
Merck blue, SPB-02T [103]	Blue	-2.5 eV	-5.2 eV	2.7 eV
SuperYellow, PDY-132 [146]	Yellow	-3 eV	-5.4 eV	2.4 eV
F8BT [161]	Green	-3.5 eV	-5.8eV	2.3 eV
Merck Red, SPR-001 [162]	Red	-2.8 eV	-5.0 eV	2.2 eV

The external quantum efficiency of OLEDs is following the equation [44,163]:

$$\eta_{ext} = \eta_{int}\eta_{out} = \gamma \emptyset_f \chi \eta_{out} \qquad (3.2)$$

$$\gamma = \frac{\eta_R}{\eta_{IN}} \qquad (3.3)$$

η_{ext} is the external quantum efficiency of the OLED/OLEC, which is determined by internal quantum efficiency (η_{int}) and out-coupling efficiency (η_{out}). η_{int} consists of recombination probability of injected holes and electrons (γ), fluorescent quantum efficiency ($\emptyset_f$) and the fraction of radiative decay (χ). According to equation (3.3), the balance factor (γ) is determined by the ratio of the current density consumed by recombination of electrons and holes and the overall current density of electron and hole injections. Ideally, electron and hole injection and transporting are well balanced, where γ equal 1. That means, they combined at the center of emission layer without excessive carriers diffusing to the counter electrode. In reality, it is quite complicated to reach the ideal case. In OLED researches, tremendous efforts have been made to confine electrons and holes within emission layer, which typically via the multi-layer system includes carrier injection layers, carrier transporting layers, and carrier blocking layers. This strategy works well for relatively expen-

sive thermal evaporation deposition manufacturing method, because multi-ultra-thin layers with high layer homogeneity are required, which make high difficulty in low-cost solution-processing alternative. Due to the low mobility of the charge carriers in organic materials, $\emptyset_f$ is almost equal 100% in the most light-emitting materials. For the fluorescent light-emitting emitter, the χ is about 25%. Because only singlet state can form radiatively decay, and emit light while triplet states are forbidden. According to spin statistics, the fraction of singlets is about 25%, while triplets are about 75% [164]. For state-of-the art OLED material, phosphorescent emitters that contain heavy metal atoms can allow singlet to triplet energy transfer through intersystem crossing. It can lead to highly efficient devices of nearly 100% radiative decay. Besides, newly reported thermally activated delayed fluorescence (TADF) [165] allows both electro-generated singlet and triplet excitons to emit light through thermal up-conversion of the lowest excited triplets to singlets combined with fluorescence from the singlet state, meaning that nearly 100% of the excitons contribute to light emission. However, most solution-processed blue OLEDs and OLECs are still using fluorescent emitters due to the difficulties to synthesize stable and long lifetime phosphorescent emitters. Therefore, the blue fluorescent light-emitting polymers are used in this dissertation. Out-coupling efficiency (η_{out}) is the fraction of photons that can escape the device and is limited by refractive indices of different layers and the substrate. Because of the big refractive index different of glass substrate (n = 1.5) and air (n = 1), around 17% light can escaped from the organic emitters to the air [166]. There are numerous methods to improve the out-couplings of the organic light-emitting devices such as micro-/nano-structure on substrates, micro-lens array, orientation management [167]. No out-coupling technique has been demonstrated in this work, because the work here is mainly focused on on-chip sensing applications. On the contrary, to emit light into air in display and lighting applications, the light generated from organic light sources is guided into biological / chemical fluidic solutions. Fluidic solutions are either water based or solvent based, which typically has much higher refractive index (n > 1.33) than air (n = 1). This makes the out-coupling a less important issue and an application dependent parameter. To sum up, in order to develop low-cost organic light source in blue light range for disposable on-chip fluorescence sensing applications, the following parameters have been confined: $\chi \approx 25\%$ due to material limitation; $\eta_{out} \approx 17\%$ with no out-coupling strategy being used; $\emptyset_f \approx 1$ thanks to the high fluorescent quantum efficiency of the light emitting polymer. The maximum EQE $= \gamma\emptyset_f\chi\eta_{out} \approx \gamma\times100\%\times25\%\times17\% = 4.25\%\times\gamma < 4.25\%$. Hence, the maximum output efficiency is determined by recombination balance factor (γ).

The recombination balance factor (γ) can be analyzed and simulated by electrical model. Up to now, only one research group (group Prof. Martijn Kemerink from Eindhoven University of Technology, Netherlands) reported numerical model on the electrical simulation of polymer LECs [107,149,168,169]. The most experimental parts were performed by Prof. Edman's group from Umeå University, Sweden. Due to the high complexity, only 1D and simplified 2D model of active layer was built and simulated, and the simulated light-emitting polymer and dopant materials are widely used SuperYellow / MEH-PPV with PEO as the solid electrolyte and $LiCF_3SO_3$ as the metal salt. The numerical model was based on widely recognized drift-diffusion, continuity and Poisson equations for classic semiconductors. The main modification here is to treat ions and cations similar to electrons and holes that drift diffusing by applied potential cross the electrodes. As the anions and cations are separated from the initial isotropic distribution, there is no recombination of the anions and cations. These denote the main difference in the drift-diffusion and continuity equations. The basic numerical simulation model is described as following:

$$J_n = D_n q \mu_n \frac{dV}{dx} + kT \mu_n \frac{dD_n}{dx} \tag{3.4}$$

$$J_p = D_p q \mu_p \frac{dV}{dx} - kT \mu_p \frac{dD_p}{dx} \tag{3.5}$$

$$J_a = D_a q \mu_a \frac{dV}{dx} + kT \mu_a \frac{dD_a}{dx} \tag{3.6}$$

$$J_c = D_c q \mu_c \frac{dV}{dx} - kT \mu_c \frac{dD_c}{dx} \tag{3.7}$$

Where J and μ refer to the current density and mobility of the charge carriers; D represents the carriers' density, while subscripts of n, p, a and c refer to electron, hole, anion and cation charge carriers, respectively. q is the absolute electron charge, V is the electrostatic potential, k is Boltzmann's constant and T is the temperature (unit: K). Einstein's relation between the diffusion constant and the mobility is assumed to hold. The ion current is zero at the electrodes, for the electrodes are ionically blocking.

The recombination process of electrons and holes inside active layer follows a Langevin process:

$$R = \frac{q(\mu_n + \mu_p)}{\varepsilon_0 \varepsilon_r} D_n D_p \tag{3.8}$$

where R is the recombination rate; ε_0 and ε_r are the dielectric and the relative dielectric constant, respectively. The continuity equations for electrons, holes, anions and cations are:

$$\frac{dD_n}{dt} = \frac{1}{q}\frac{dJ_n}{dx} - R \tag{3.9}$$

$$\frac{dD_p}{dt} = -\frac{1}{q}\frac{dJ_p}{dx} - R \tag{3.10}$$

$$\frac{dD_a}{dt} = \frac{1}{q}\frac{dJ_a}{dx} \tag{3.11}$$

$$\frac{dD_c}{dt} = -\frac{1}{q}\frac{dJ_c}{dx} \tag{3.12}$$

The potential profile throughout the device is calculated from Poisson's equation:

$$\nabla(-\varepsilon_0 \varepsilon_r \nabla V) = q(D_p - D_n + D_c - D_a) \tag{3.13}$$

Initially, the LEC contains neither electrons nor holes, but it is filled with a constant concentration of ions. In their model, the *in situ* electrochemical doping affects two aspects: 1) the potential distribution over active layer, according to equation (3.13); 2) the doping dependent carrier mobility, see equation (3.14)

$$\mu_{p/n} = \frac{\mu_{p/n,1} - \mu_{p/n,0}}{1 + e^{\frac{(f_0-f)}{W}}} + \mu_{p/n,0} \tag{3.14}$$

Here f is the doping fraction which is equal to the carrier density divided by the density of states (= 0.3 nm^{-3}). This approximation of the doping fraction is justified by the observation that the net ion density always equals the net electronic charge density in the doped regions. Regarding the other parameters, $\mu_{p/n,1}$ is the mobility at maximal doping (f = 1), $\mu_{p/n,0}$ is the mobility in the absence of doping (f = 0), and f_0 and W are two parameters that set the transition from μ_0 to μ_1 : f_0 determines at which doping fraction the mobility increases and W determines the range of doping fractions over which this increase occurs. The f_0 and W were empirical parameters and set to fit the experimental results. The injection model of electrons and holes injected from cathode and anodes was based on a Modified Boltzmann injection model:

$$n(1) = N_0 e^{-(\frac{\Delta - [V(2) - V(1)]}{KT})} \tag{3.15}$$

where n(1) is the electron density at the first grid-point next to the electrode, Δ the injection barrier height, V(i) the potential at grid-point i (=1, 2), N_0 the electron density of states, k the Boltzmann constant and T the temperature. Hence, the Boltzmann factor is effectively evaluated at the 2nd grid point. The potential at the 1st grid point V(1) is taken as a boundary condition for the potential and is thus constant, i.e. $0+\Delta$ or $V_{bias}+\Delta$. The potential at the neighboring grid-point however changes due to space charge accumulated in the EDLs, which facilitates injection of electron or holes. In this model, injection is not affected by the grid-point spacing and thus thicker devices can be simulated while not having to alter the number of grid-points because of injection problems. The injection model is compared with classical Fowler-Nordheim [170] and Emtage O'Dwyer [171] injection models. They all showed similar results [169].

Even though the electrical model is much simplified and analyzes only 1D and simplified 2D geometric layer architectures, numerous input parameters are still required to be measured so that the model can as much as possible to reflect the real device physics. The important input parameters such as electron and hole mobility, ionic mobility of dopants, doping dependent carrier mobility, doping fraction (f) as well as range of doping fraction (W) are either non-known or hard to be measured. Even for well-known and heavily researched SuperYellow light-emitting polymer and dopant composite of PEO plus KCF_3SO_3, most of the parameters were either approximate values from literature or purely empirical value to fit the experimental results. For the active materials (Merck Blue LEP + DCH18C6 + $LiCF_3SO_3$) used in this work, few parameters can be found from literature. Shoji et al [115] reported to use time-of- flight secondary ion mass spectrometry (ToF-SIMS) to obtain ion depth profiles for both fixed- and dynamic-junction LECs. Although they used same light-emitting polymer and metal salt, a different ionic solid electrolyte (trimethylolpropane ethoxylate) and electrode (gold) were used, which had different ionic mobility and carrier injection. No electron and hole mobility of Merck Blue can be found in literatures. Therefore, the electron-hole recombination rate and emission zone profile cannot be numerically simulated in this dissertation. The equations are rather used for qualitatively analysis of device performance.

In this work, the out-coupling efficiency is fixed due to the glass substrates and fixed layer architecture. The fluorescent emission efficiency is also fixed due to the used

blue LEP (i.e. Merck Blue). χ is fixed to 25% as Merck Blue as well as SuperYellow is a fluorescent emitter. Therefore, the external quantum efficiency depends mainly on recombination efficiency (γ) in this work.
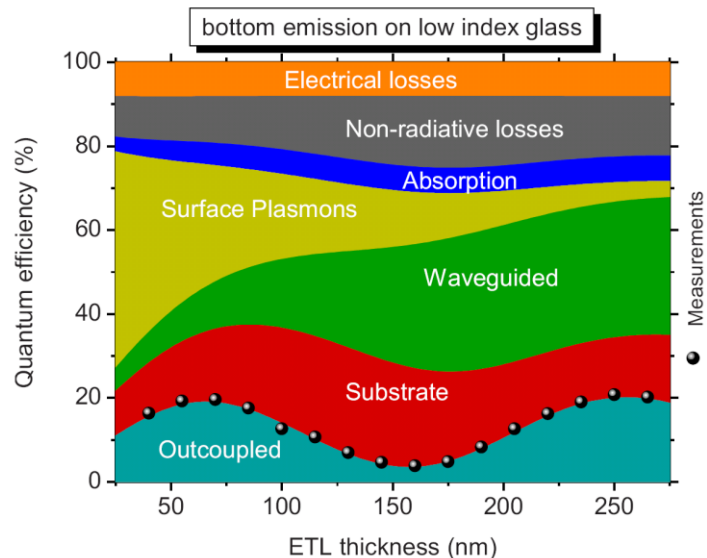

Figure 3-2 Measured EQE at 1.51 mA/cm^2 of the red bottom OLEDs as a function of the n-layer thickness and comparison to simulation results. At this current density, the highest EQE of 21% at 330 cd/m^2 brightness is reached in the second maximum. The figure also shows the distribution of all loss channels in the devices. Copyright (2010), AIP Publishing LLC, reprinted from literature [172].

In current OLED and LEC research community, display and lighting applications are the focus, which means the target brightness is lower than 1000 cd/m^2. After achieving the target brightness, tremendous efforts have been out on improving the efficiency by lowering the driving voltage and operation current as well as extending operation lifetime. It is known that OLED exponentially meets efficiency roll-off at high driving current density, i.e. high emitted brightness situation [173,174]. The similar efficiency roll-off has also been reported in OLECs [149]. Several reasons have been identified to describe the roll off of device efficiency at high operation current density: singlet-singlet annihilation and singlet-heat annihilation [19,175] , triplet-triplet annihilation and triplet-exciton quenching [176,177], dissociation of excitons induced by the electrical field, exciton concentration quenching [178], loss of charge carrier balance at high current density [179], or exciplex emission [180]. For our OLEC material and architecture, only fluorescent emitter is used and no lighting buffer layer or host material are used. Hence, triplet-triplet annihilation, triplet-exciton quenching, and exciplex emission are not applicable here. Consequently, the

generation and decay of exciton species equation [181] can be re-written in our case as following:

$$\frac{dS(z)}{dt} = \chi R(z) + \vec{\nabla} J_s(z) - \left(k_{rad}(z) + k_{nonrad}(z)\right)S(z) - k_{annihilation}S(z)^2 \qquad (3.16)$$

In equation (3.16), χ is the generation efficiency pre-factor (25% in our case), R(z) the position dependent electron-hole recombination rate, $J_s(z)$ exciton diffusion current density, $k_{rad}(z)$ the position-dependent radiative decay rate, k_{nonrad} the non-radiative decay rate and $k_{annihilation}$ a singlet-singlet annihilation rate. In OLEC, due to the additional ionic donor from metal salt and ionic transporter from solid electrode, additional quenching has been observed: Self-absorption effect of doping concentration and layer thickness [182], electrochemically induced "side-reaction" due to solid electrolyte [183], exciton quenching due to electrochemical doping [184–186], exciton quenching due to over-doping.

In summary, according to equation (3.2), (3.3) and (3.16), a balanced electron-hole injection should be target at high current density / voltage, optimized doping concentration and layer thickness to minimize doping induced quenching, and a relative broad intrinsic emission zone to avoid concentration, singlet-singlet quenching as well as exciton to doping quenching. Considering the high complexity of mathematical simulation model and difficulty in approaching physical device behavior, an experimental approach has been adopt to analyze light emitting behavior of recombination balance factor (γ). The detail is described in the next chapter.

3.4 Lifetime considerations

Organic semiconductor devices are well known to have poor lifetime compared to inorganic counterparts. The fundamental reason is the low thermal and mechanical stability of the organic materials. Thus, researching of synthesizing high thermal stable light-emitting organic material, in particular high glass transition temperature (T_g) and high decomposition temperature (T_d), is the one main key to extend organic light-emitting device lifetime. Besides, four main external factors that affects the device lifetime are moisture, oxygen, dust particles, and inhomogeneous thin film surfaces.

In general, the degradation of OLEDs due to moisture can be contributed to the dark spot formation at the metal cathode [158]. In order to achieve good electron injection

into emissive layers, low-work-function metal / metal alloy layers (Ca, Ba, Li, Li:Al, Mg:Ag, etc.), or ultra-thin (~ 1 nm) metal-halide or metal-oxide layers (LiF, CsF, etc.) are commonly used as the cathode and electron injection layers. However, most of them are air-instable and vulnerable to moisture. Without proper encapsulation with a desiccant inside a sealing canister, moisture insulating metal-oxide moieties can be generated via the oxidation of cathode metals at the metal-organic interface, which contribute to dark spots. Consequently, the modern OLEDs are finished with high vacuum evaporation of metal layers and immediately encapsulated under inert atmosphere. This process is part of reason for high manufacturing costs of OLEDs. Figure 3-3 shows the illuminated pixels of in-house fabricated blue and yellow OLEDs. The PEDOT:PSS HTL and active layer (10 mg/mL Merck Blue or SuperYellow in toluene) were spin-coated under ambient condition. After thermal annealing, 2 nm LiF EIL, 150 nm Al cathode, and 300 nm Al_2O_3 protective layer were deposited via sequence thermal evaporation method under high vacuum. Al_2O_3 protective layer was intended to avoid degradation of LiF and Al in air before encapsulation. Devices were then encapsulated with epoxy, glass coverslips and short UV irradiation. Nevertheless, many dark spots can be clearly observed in both blue and yellow OLEDs, which indicate that there were still moisture residual inside device and react with Al and LiF.

Apart from moistures, oxygen and UV light are other well-known detrimental substances for OLEDs. In principle, the oxygen molecules inside OLED device convert into reactive singlet oxygen radicals under UV irradiation (photo-initiation process). These radicals can easily react with carbon atoms of conjugated organic molecules [156,187,188]. One good example is the aliphatic double bond in conjugated phenylenevinylene polymers (PPVs), which is part of SuperYellow LEP. This double bond can be broken with singlet oxygen radicals and forms an aldehyde end-group, which is an exciton quencher and highly reduces the OLED efficiency. Consequently, OLEDs are mainly fabricated under inert atmosphere or high vacuum to avoid oxygen induced degradation. In order to reduce the manufacturing cost, the OLEDs can also be solution-processed under ambient condition as far as direct UV irradiation is avoided and devices are encapsulated in oxygen-free environment [157].
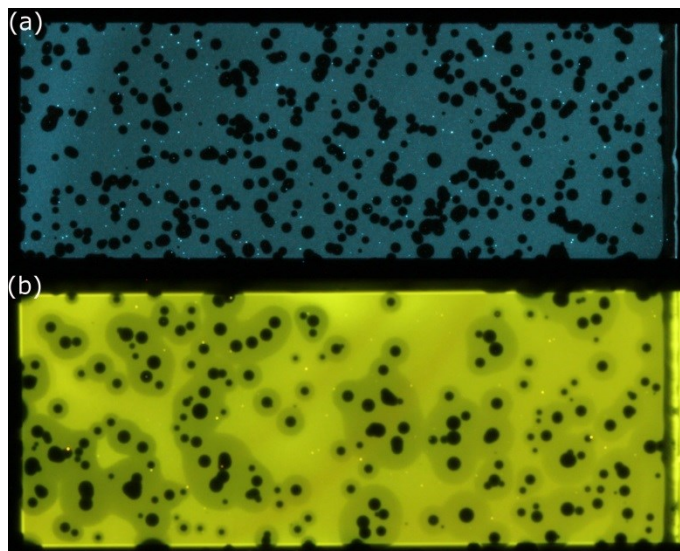
Figure 3-3 Photographs of illuminated (a) blue and (b) yellow OLED pixels (1.5× 5 mm^2) with dark-spots. Device architectures are: Glass substrate || patterned ITO (100 nm) || PEDOT:PSS (40 nm) || Merck Blue (blue) or SuperYellow (yellow) (100 nm) || LiF (2 nm) || Al (150 nm) || Al$_2$O$_3$ (300 nm).

Electrical stress-induced degradation is another lifetime issue for OLEDs. Especially, when dust and inhomogeneity presents in EML, extreme high current will flow through the inhomogeneous spot and generate burnout of organic material or electrical short [189]. High current density tends to generate material degradation due to the thermal effects of non-radiative emission. Hence, dust-free, homogeneous thin films, high thermal stability LEP, and good thermal management are crucial for organic light-emitting device operated at high current density. For this reason, low surface roughness and high EML homogeneity is crucial for OLEDs working under high current. On the other hand, due to the dynamic doping mechanism of OLECs, the surface roughness can be partly compensated during *in situ* P-N junction generating. Higher EML thickness also reduces the short-cut risk due to the impurities.

Compared to OLEDs, OLEC tends to have even shorter operation lifetime because of the intrinsic *in situ* electrochemical doping induced fluorescent quenching [190], typically ~ 100 h of OLECs compared to more than 10 000 h.

3.5 Doping propagation investigation

As described in section 2.3, OLEC can work with relatively large layer thicknesses. Thus, the planar structure can be fabricated to investigate the doping propagation property of OLECs. Consequently, the electrochemical doping can be imaged and recorded for

analysis to understand the doping behavior of much thinner devices with the sandwich architecture. An assumption is made here that the solution-processed active material composite (LEP, solid electrolyte and metal salt) has isotropic distribution, and thus they have no distinguish behaviors between sandwich and planar layer architecture. It has been also reported that the type of electrode combinations influences the doping profile of OLECs [191]. Hence, the corresponding electrodes should be used for doping propagating investigation.

For explaining the different phases of doping propagation, the fully solution-processed blue OLEC architecture is used here (see section 4.2.1). ITO (4.7 eV) has similar work-function as Ag (4.6 eV), which should limit the influence of electron injection due to work-function barriers. Therefore, the device with Ag and ITO as a cathode should behave similarly. The sandwich device performance is described in detail in section 6.2. Manufacturing detail of this planar device is described in section 4.2.3.

The doping process of blue planar OLEC device was recorded by a digital camera (Canon EOS 60D) with a 5X lens from 0 min till 45 min with 1000 V bias, at 85 °C, and under UV irradiation. The electrodes have a spacing of 300 μm. That means the electrical field across electrodes was approximately 3.33 MV/m. There were several distinguish doping propagation phases:
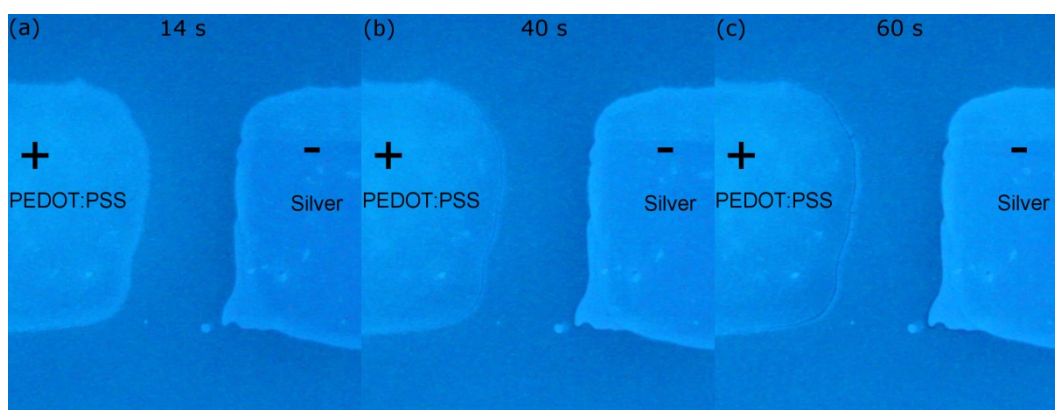
Phase 1: Double layer generation:

Figure 3-4 Photo-imaging of a planar blue OLEC which was driven at 1000 V voltage bias under UV irradiation. The sample was heated at 85 °C on a hot-plate. The images were taken at (a) 14 s, (b) 40 s, and (c) 1 min after voltage bias was applied.

As shown in Figure 3-4, the thin black lines were generated after less than 1 min at the interface between active material and electrodes, where anode side (40 s) is faster than cathode side (1 min), which could due to the less work-function mismatch at anode side than cathode side. After the double layer was generated by doping the interface material, the injection of the electrons and holes were enhanced and further doping could continue.

Phase 2: Propagating of p- & n-type doping:

As illustrated in Figure 3-5, the doping areas (active material losing photo-luminance and turn dark) were propagated towards to each other. Moreover, it can be clearly seen that the p-type doping was faster than the n-type doping. It also can be observed that the doping fronts reflected the edge shapes of the electrodes.
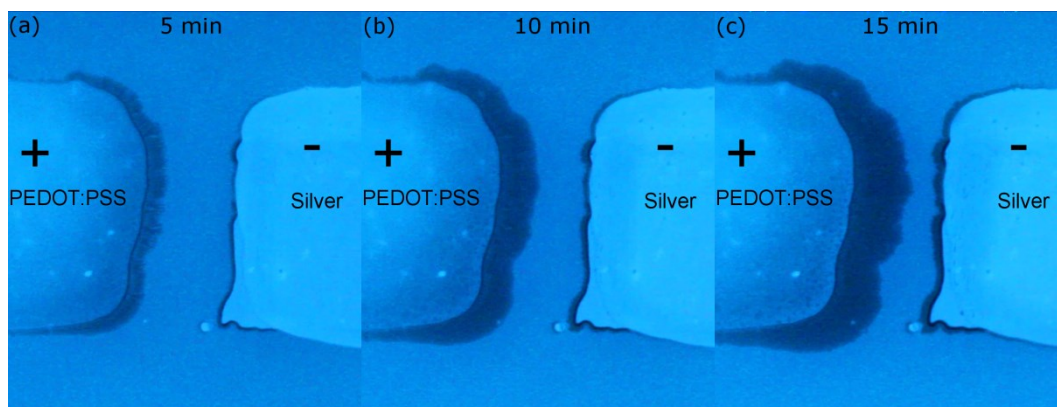

Figure 3-5 Photo-imaging of a planar blue OLEC which was driven at 1000 V voltage bias under UV irradiation. The sample was heated at 85 °C on a hot-plate. The images were taken at (a) 5 min, (b) 10 min, and (c) 15 min after voltage bias was applied.

Phase 3: p- & n-type doping areas meet each other and generate intrinsic light emitting area:

The pioneers of doping areas met each other after approximately 19 min. After about another 9 min, an intrinsic light-emitting thin line can be clearly seen. Therefore, a P-I-N junction was finally formed and the best performance should be achieved at this point. It should be pointed out that the light-emitting area / intrinsic part had a compensated shape of P-doping and N-doping fronts. Moreover, this compensation was favor towards the closer electrode (Ag, in this case). This phenomenon contributes the high surface roughness tolerance of OLECs.
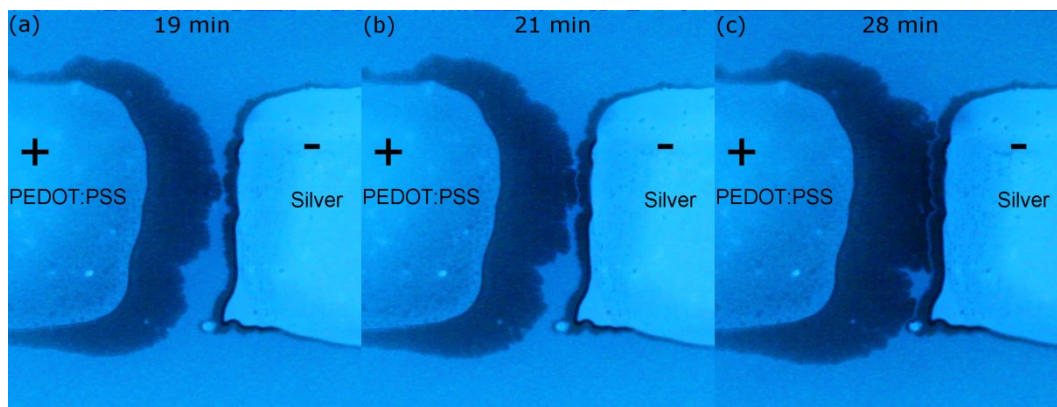
Figure 3-6 Photo-imaging of a planar blue OLEC which was driven at 1000 V voltage bias under UV irradiation. The sample was heated at 85 °C on a hot-plate. The images were taken at (a) 19 min, (b) 21 min and (c) 28 min after voltage bias was applied.

Phase 4: Over-doping and quenching of light

When the voltage bias was still on, the doping areas continued towards each other and penetrated each other. Emitted light (generated excitons) within the "intrinsic area" was quenched by electrochemical doping and then became weaker and weaker. It can be clearly seen that the doped area become darker and darker, which could also absorb emitted light from intrinsic area and contribute to reduction on emitted light intensity.
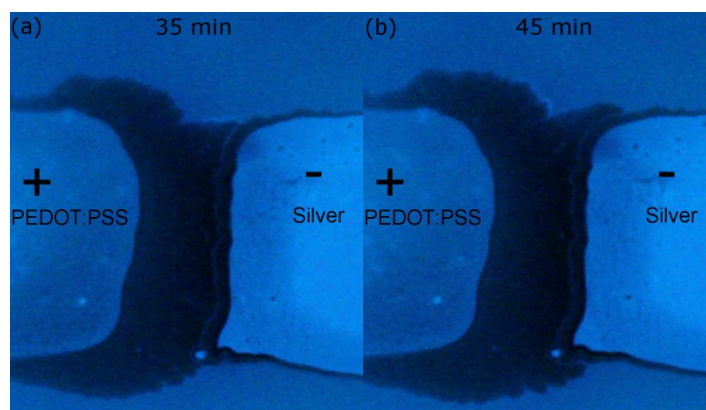

Figure 3-7 Photo-imaging of a planar blue OLEC which was driven at 1000 V voltage bias under UV irradiation. The sample was heated at 85 °C on a hot-plate. The images were taken at (a) 35 min and (b) 45 min after voltage bias was applied.

In summary, by applying voltage across the electrodes, LEP can be electrochemically doped and generate both P- and N-doping area (proved by losing photo-luminance ability). The doping area can propagate towards each other when solid electrolyte and ionic metal salt were well distributed inside active material. With the used materials, the P-

doping has faster propagation speed than N-doping. From the taken images, it can be calculated that the overall P-doping speed verse N-doping speed is about 5.3:1. This fits the theory as most LEPs have higher hole mobility than electron mobility, which is particularly true for Merck Blue and SuperYellow LEPs [192]. Additionally, a planar yellow OLEC between an ITO cathode and a PEDOT:PSS anode was also fabricated and characterized. The detail is described in the appendix section.

4 Experimental methods and procedure

In this chapter, solution-processing techniques of spin coating and inkjet printing were utilized for depositing functional thin films for organic light source manufacturing. The solution-processing parameters and surface treatments were examined and optimized to deposit homogenous thin films at targeted thicknesses for the device performance investigation in chapters 5 and 6. After the layer-by-layer parameter optimization, a full description of manufacturing procedures for a blue OLEC, yellow OLED and devices with planar structures were detailed in second section. The device characterization methods were described in the last section.

4.1 Solution-processing parameter optimization

4.1.1 Inkjet printing of the bottom electrode

For the device performance investigation, the pre-patterned ITO was used mainly as the bottom electrode (cathode). However, in order to replace the relatively expensive ITO electrode that was sputtered and patterned via a lithographic method, two approaches have been introduced in this work:

1) Inkjet printing silver electrode using a silver nanoparticle dispersion;
2) Inkjet printing transparent conducting polymer PEDOT:PSS as the bottom electrode and solution-processing ZnO layer or ZnO / PEI mixture as a work function adaptation layer to improve the electron injection.

The first method provides good electrical conductivity, simple layer structure and an additional light reflection from mirror property of silver. A higher efficiency was achieved with this method, thanks in part to the micro-cavity effect [193,194]. On the other hand, the light can only be top-emitted, which limits its application in integrated on-chip sensing applications. Moreover, a high sintering temperature of > 200 °C is normally required to realize good conductivity, good light reflectivity and low exciton quenching due to plasmonic effect [195]. The second method, printing a PEDOT:PSS layer, shows lower electrical conductivity (typically 500 S/cm). However, it provides fully transparent device with higher flexibility in chip integration, much lower processing temperature of < 120 °C.

Inkjet silver bottom electrode

For inkjet printing thin film deposition, good wetting of the surface is very important to form regular and controllable 2D structures. Figure 4-1 shows the photographs of inkjet-printed silver structures on non-activated and plasma-activated glass surfaces. Rectangular stripes (Figure 4-1b) were intended to be inkjet printed, while structures with irregular edges (Figure 4-1a) were formed because of "bad" surface wetting.
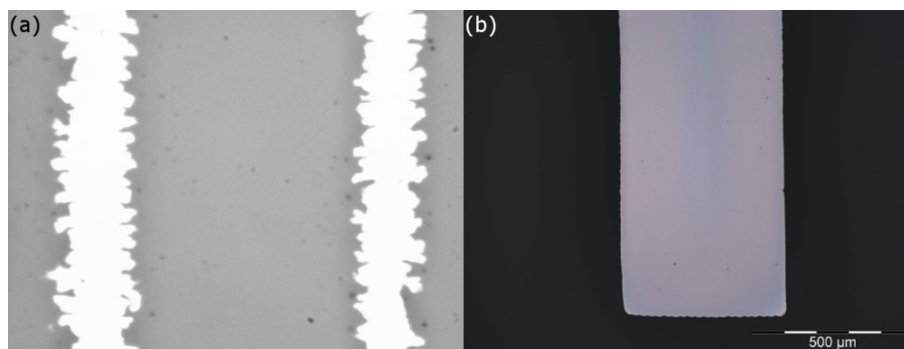

Figure 4-1 Inkjet-printed silver structures on glass with (a) no surface activation and (b) low-pressure argon plasma activation.

For inkjet printing, the silver nanoparticle ink was heated up to 35 °C at the printhead in order to reduce the viscosity and improve the jetting ability. The substrates were heated up to 60 °C to increase the drying speed of the inkjet-printed ink and prevent it from spreading. Before geometric profile measurement, the inkjet-printed silver structures were thermally sintered at 200 °C for 15 min in a convection oven. Thus, all remaining solvent were evaporated and silver nanoparticles were merged. According to the datasheet of the ink supplier, a conductivity of 100 000 S/cm, which is 16% of the bulk Ag conductivity, can be achieved. The conductivity of printed Ag structures under different sintering temperature was investigated. After 30 min sintering in a convection oven, the printed silver structure had a conductivity of 1.4, 36 386, and 123 856 S/cm, which means ~0.000 23%, 6%, and 20% of bulk Ag conductivity, respectively. It can be seen that the printed electrodes have much lower electrical performance compared to bulk material as well as evaporated materials. This is one crucial factor for lower device performance of solution-processed OLEDs/OLECs compared to all-evaporated devices.
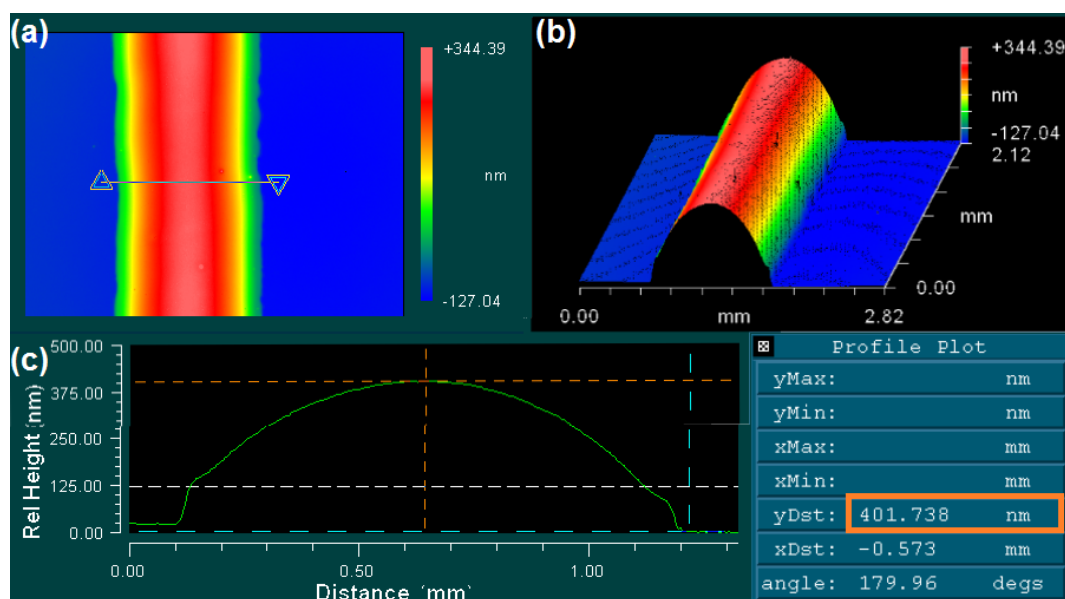
Figure 4-2 White light interferometer measurement of inkjet-printed and sintered Ag bottom cathode with 1 mm line-width: (a) Top view and (b) 3D view of an inkjet-printed Ag line, (c) cross-section of the inkjet-printed Ag line; The cross-section measurements were taken at the positions indicated by the line between two triangles on the 2D top view images. The peak height of the Ag line is indicated inside orange rectangular frame.

For an ITO-free, fully solution-processed blue OLEC (see section 6.1), 1 mm wide Ag stripes were inkjet printed as bottom electrodes and electrical wiring. The geometric profile was measured and the result is presented in Figure 4-2. Although a good 2D shape can be optimized by controlling the surface wetting and printed dot spacing, the printed Ag lines did not have ideal cuboid 3D shapes. From center to edge, there is as much as 275 nm difference in height with a peak height of 400 nm. This is highly related to the drying effects of printed ink and solvent systems of the ink. The silver nanoparticle dispersion contains a high boiling point solvent ethylene glycol (boiling point: 197.3 °C), which prevent the printed solution from fast drying. Although the top surface flatness can be further improved by optimizing the printing parameters such as dot spacing, printing temperature, printing speed, these printed silver lines were still used as a bottom electrode for ITO-free blue OLEC (see section 6.1). Consequently, it can be demonstrated that OLECs can work with relative high height deviation and roughness, and still emitted relative bright light.
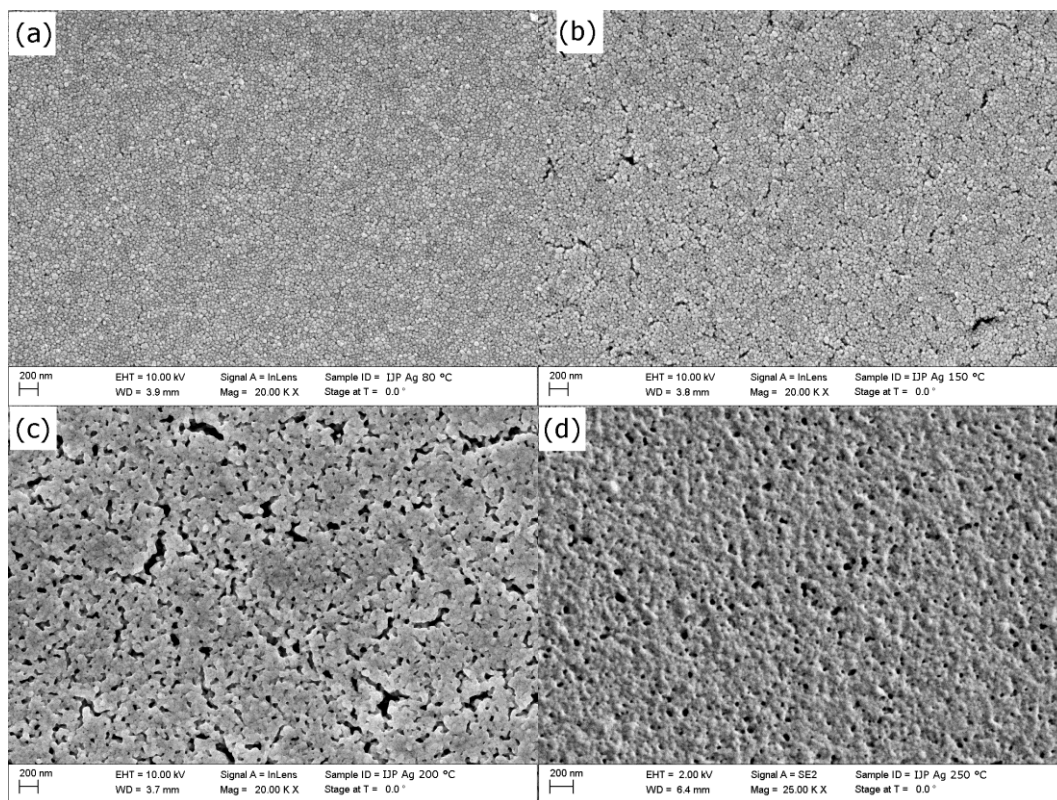
Figure 4-3 Electron scanning microscope (SEM) images of inkjet-printed silver layers that were sintered at (a) 80 °C, (b) 150 °C, (c) 200 °C, and (d) 250 °C for one hour in a convection oven.

One big drawback of depositing a silver electrode from a silver nanoparticle dispersion is the relatively high sintering temperature to obtain high conductivity and optical reflectivity. Figure 4-3 shows the nano-structures of inkjet-printed silver layers sintered at sintering temperatures of 80, 150, 200 and 250 °C by the SEM measurement. It can be seen that with increasing temperatures, the inkjet-printed silver nanoparticles merged better and grew to larger flakes, which not only increase the electrical conductivity but also limited the possible plasmonic effect on exciton quenching. For most organic light-emitting emitters and plastic flexible substrates, 150 °C is the critical temperature. Therefore, the sintering temperature should be lower than 150 °C to prevent device degradation and plastic substrate melting. However, even after one hour sintering at 150 °C, particles with a diameter of less 50 nm are well distributed over the surface of the inkjet-printed silver layer. Consequently, weak or no light emission is observed when using inkjet-printed and low temperature sintered silver as the top cathode. This problem can be highly relieved when a cross-linked interlayer is used [29]. Due to the microstructure or nano-structure of printed and sintered silver layers, the reflectivity of the silver layers also varies, as shown in Figure 4-4. It is also an indicator that some light were absorbed inside silver layers or scattered away due to the micro- and nano-structures. Therefore, inkjet-printed silver was used as a

bottom electrode instead of a top electrode due to high sintering temperatures and possible plasmonic exciton quenching effects.
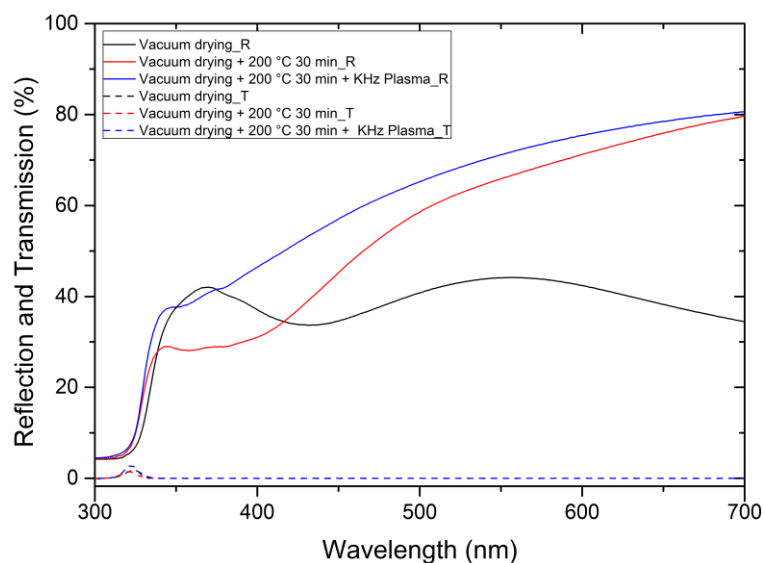

Figure 4-4 Reflection and transmission spectra of inkjet-printed silver mirrors that were sintered at different conditions: (1) No sintering, only vacuum drying (black); (2) thermally sintered at 200 °C for 30 min in a convection oven (red); (3) Additional KHz argon plasma sintering (240 W, 30 min) after thermal sintering (blue).

Inkjet printing PEDOT:PSS bottom electrode

For bottom electrode with PEDOT:PSS plus ZnO combinations, this strategy has an advantage of bottom emitting because of the high transparency of PEDOT:PSS layer and thin ZnO layer. For direct on-chip integration, the solution-processed OLECs/OLEDs should emit light from the bottom side and guided into the microfluidic channels for excitation of fluorescence dyes.

Figure 4-5 illustrates the geometric profile measurement of inkjet-printed PEDOT:PSS structures. As the PEDOT:PSS ink is water-based, no heating of printheads and substrates were performed to minimize the nozzle clogging risk. Before geometric profile measurement, the printed structures were dried at 100 °C for 15 min so that all the remaining solvents were evaporated. It can be seen that single printed droplets on a glass substrate, which was cleaned and activated by isopropanol, had a droplet diameter of ~85 µm and peak height of 24 nm. The inkjet-printed droplets had very clear coffee-ring effects. With a dot spacing of 50 µm, a well-structured single line with a line-width of ~90 µm and height of 32 nm was inkjet printed. By a dot spacing of 50 µm in both X and

Y direction, a 5×5 mm^2 pad with an average height of ~41 nm was inkjet printed. When comparing inkjet-printed PEDOT:PSS with silver stripes, PEDOT:PSS stripes have flatter top surfaces and better height control via multi-layer printing. Nevertheless, it has to be pointed out that for different surface activations and structure dimensions a slight modification in dot spacing is necessary to obtain uniform surfaces of inkjet-printed thin films.
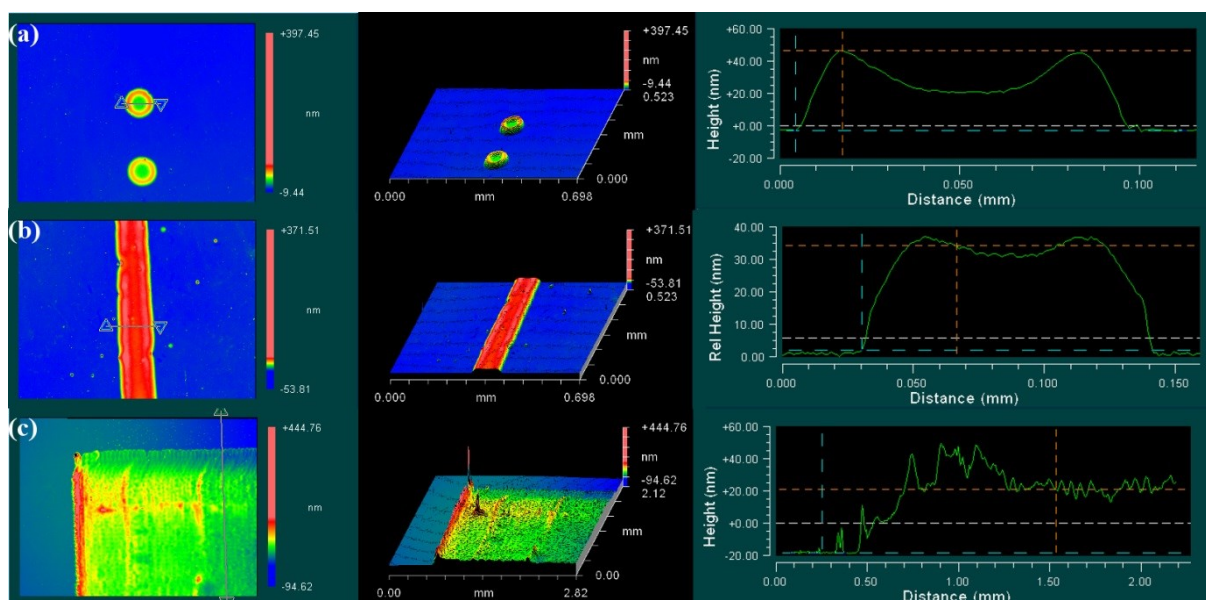

Figure 4-5 White light interferometer measurement of inkjet-printed PEDOT:PSS (a) dots, (b) single line, and (c) Pad. Left and middle images show the 2D top and 3D view of measured structures, while right images show the cross-section of corresponding structures. The cross-section measurements were taken at the positions indicated by a line between two triangles on the 2D top view images.

4.1.2 Solution-processing ZnO and PEI interlayer

For the ZnO layer deposition, there are two solution-processing approaches: Via a Zn(acac)$_2$ precursor ink or ZnO nanoparticles dispersion. The Zn(acac)$_2$ precursor ink has the advantage of low material cost, while ZnO nanoparticles dispersion has the advantage of easy inkjet printability, high reproducibility, and higher conductivity with Al doping.

For the Zn(acac)$_2$ precursor ink, the Zn(acac)$_2$ was dissolved in ethanol to form a volume concentration of 20 mg/mL. It was heated up to 50 °C and stirred at 400 RPM before spin-coating. The spin coating was performed at ambient conditions with a spin rate of 1600 RPM for 45 s. Afterwards; the samples were immediately transported onto a hot plate with a setting temperature of 125 °C for 45 s. Thus, the ZnO layer can be generated by thermal decomposition at ambient conditions. Figure 4-6 shows the profile measurement of

spin-coated and thermally sintered ZnO layer from the $Zn(acac)_2$ precursor ink via white light interferometer. The layer thickness is relatively thin (~10 nm) and has a surface roughness of ~1.7 nm

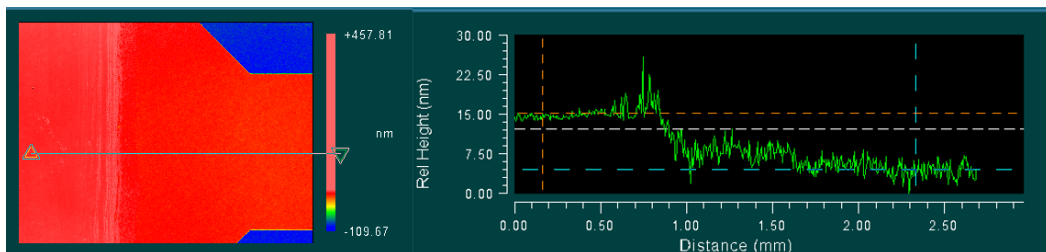

Figure 4-6 White light interferometer measurement of a spin-coated ZnO layer from 20 mg/mL $Zn(acac)_2$ ink with a spin rate of 1600 RPM for 45 s, and sintered at 120 °C for 45 s (a) the 2D top view of measured structures, (b) shows the cross-section of corresponding structures. The cross-section measurements were taken at the positions indicated by a line between two triangles on the 2D top view images.

Commercially available Al-doped ZnO nanoparticle ink provides a direct possibility of inkjet printing a ZnO interlayer. The inkjet-printed thin films can be sintered as low as 100 °C, which is beneficial for thin film deposition on polymeric substrates with low thermal stability. As reported in the literature [24], it is normally thermally sintered at 150 °C for 10 min for higher conductivity. A theoretical work-function of -3.9 eV should be realized on Al:ZnO (short for Al doped ZnO) thin films. This provides much better electron injection than commonly used cathodes such as Ag (-4.6 eV), Al (-4.3 eV), and ITO (-4.7 eV). Figure 4-7 (a) and (b) shows the inkjet-printed Al: ZnO layer from the nanoparticle ink on glass substrates with pre-patterned ITO electrodes. Before inkjet printing, the substrates were activated by short low-pressure argon plasma (100 W, 30 s) to obtain good wetting. Two different dot spacing of 40 and 60 μm in both x and y directions were used to realize two layer thicknesses. As it can be seen in Figure 4-7, both dot spacings result in relatively homogeneous thin films with some irregularities at the edges. Thus, the interlayer is normally slightly larger than the actual light-emitting pixel size to avoid the influence of the irregularities at the thin film edges. A dot spacing of 40 μm results in a thin film with an average layer thickness of 70 nm while 40 nm for dot spacing of 60 μm. They have a root-mean-square roughness of 14.7 and 12.8 nm for dot spacing of 40 and 60 μm, respectively. Because the Al:ZnO nanoparticle ink is alcohol-based solution and PEI has high solubility in alcohol-like solvents [102], another great advantage it has is that it can form a new inkjet-printable ink when mixed with PEI. As described in the theoretical part (section 2.2), the solution-processable PEI ultrathin layer can greatly reduce the work-

function of different electrodes (Ag, Al, ITO, and ZnO) by interfacial dipoles. However, the drawback is that it has to be ultrathin (< 10 nm) as it is in principle an electrical barrier layer. Such ultrathin layers are highly difficult to inkjet print, and typically result in high porosity and / or in-homogeneous layers. Consequently, a single layer printed from mixture of Al:ZnO nanoparticle ink and 0.5 wt% PEI aqueous solution simplifies the manufacturing process from two layers to one layer and is applicable for the low-cost and flexible inkjet printing technique. Figure 4-7 (c) and (d) presents the measured inkjet-printed thin films from the mixed ink. The process parameter is identical to pure Al-doped ZnO nanoparticle ink. With the same 40 and 60 μm dot spacing, slightly higher layer thicknesses of 89 and 25 nm were deposited on ITO.

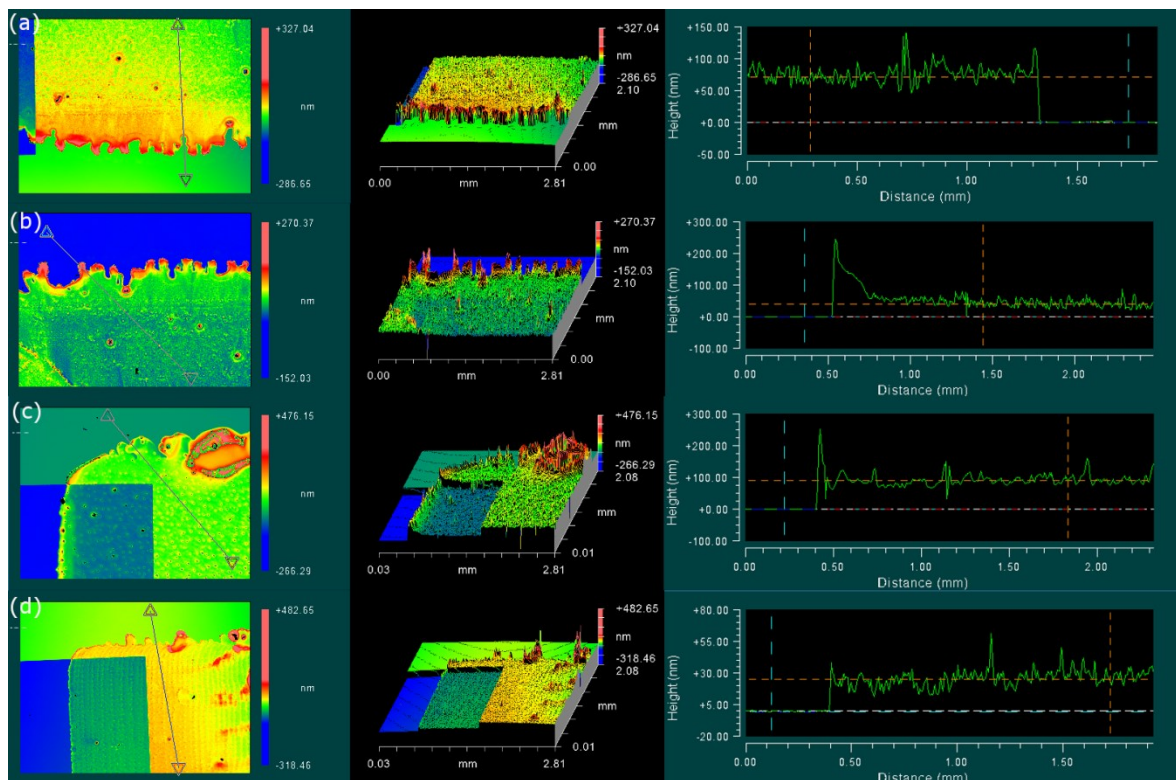Figure 4-7 White light interferometer measurement of inkjet-printed Al-doped ZnO thin film with dot spacing of (a) 40 μm and (b) 60 μm, and inkjet-printed thin films from Al-doped ZnO mixed 0.5 wt% PEI ink with dot spacing of (c) 40 μm and (d) 60 μm. All thin films were inkjet printed on pre-patterned ITO glass substrates. The substrates were activated by short low-pressure argon plasma (100 W, 30 s) before inkjet printing. Left and middle images show the 2D top and 3D view of measured structures, while right images show the cross-section of corresponding structures. The cross-section measurements were taken at the positions indicated by a line between two triangles on the 2D top view images.

In order to understand the influence of the thermal annealing, the inkjet-printed Al:ZnO and Al:ZnO:PEI thin films were scanned by SEM measurements. For these meas-

urements, Al:ZnO nanoparticle ink was inkjet printed on top of silicon wafers, whose surfaces were activated by low-pressure argon plasma with 100 W for 30 s. All thin films were inkjet printed with a dot spacing of 50 μm at 1500 Hz and at bi-direction printing mode. A PiXDRO LP50 inkjet printer with a DMC cartridge was used for inkjet printing. Printed Al:ZnO thin film was sintered at 150 °C for 30 min in a convection oven, while Al:ZnO:PEI thin films were sintered at 100 °C for 15 min and 150°C for 30 min, respectively. The SEM images are shown in Figure 4-8. By comparing the Figure 4-8a with b, polymer structures around partly merged Al:ZnO nanoparticles can be clearly observed. These are believed to be the mixed PEI polymer chains. Most literature reported thermal annealing temperature for PEI is 100 °C on a hot plate [26,27,30,102,148,196]. However, inkjet-printed ZnO thin films are typically sintered at higher temperatures, because the ZnO nanoparticles can be merged better, which results in a higher electrical conductivity. Thus, another inkjet-printed Al:ZnO:PEI thin film was sintered at 150 °C for 30 min in a convection oven. The SEM image (see Figure 4-8c) indicates that t there are more instances of particle merging while still surrounded by polymer structures. This proves that the Al:ZnO:PEI ink is compatible with Al:ZnO processing parameters. As described in section 2.2, the working mechanism of PEI is the work-function reduction induced by interfacial dipoles. Therefore, an ultra-thin layer is typically required because of the intrinsic high electrical resistance. However, thicker Al:ZnO:PEI layer is possible because the thin PEI is surrounding the sintered Al:ZnO structures and relatively high electrical conductivity of sintered Al:ZnO structures. This provides a novel, one-step, inkjet-printed work-function reduction interlayer. The detailed device performances are investigated and described in chapter 5.
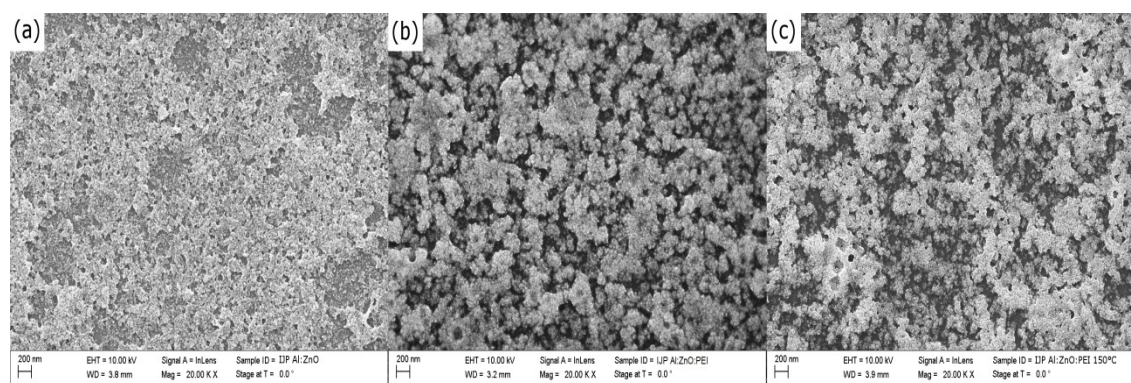

Figure 4-8 Scanning Electron Microscope (SEM) images of an inkjet-printed (a) Al:ZnO thin film sintered at 150 °C for 30 min, (b) Al:ZnO:PEI thin film sintered at 100 °C for 15 min, and (c) Al:ZnO:PEI thin film sintered at 150 °C for 30 min. All thin films were inkjet printed on top of silicon wafers.

4.1.3 Spin coating organic emissive layers

As described in chapter 3, a spin-coating method is used for in this dissertation for depositing active layers for both OLEDs and OLECs. The advantages of the spin coating technique are that a very thin and homogenous thin film can be quickly deposited, and the layer thickness can be controlled relative well by varying the spin-rate. It is good for scientific understanding and investigation of material properties.

To produce the blue OLEC ink for spin-coating, Merck Blue LEP was dissolved into toluene so that a LEP solution with a volume concentration of 10 or 12 mg/mL was produced. Dopant solutions were simultaneously prepared by dissolving DCH18C6 and LiCF$_3$SO$_3$ in toluene with various concentrations but always kept at the same mass ratio of DCH18C6 and LiCF$_3$SO$_3$ to 5:1 (e.g. 40 mg/mL DCH18C6 and 8 mg/mL LiCF$_3$SO$_3$). Both inks were stirred at 400 RPM and heated to 50 °C overnight. Afterwards, proper portions of both inks were mixed together to obtain a polymer volume concentration of 10 mg/mL in toluene and different mass ratios of LEP, DCH18C6 and LiCF$_3$SO$_3$ to 1:1.35:0.27, 1:0.5:0.10, and 1:0.10:0.02. The mixed inks were again stirred at 400 RPM for more than 4 h and heated at 50 °C on a hot plate. The pure LEP ink was filtered through a PTFE membrane syringe filter with a pore size of 1 μm before mixed with dopant inks.

For spin coating the OLEC active layer, in order to obtain different layer thicknesses, spin rates of 500, 1000 and 1500 RPM were adopted to achieve the layer thickness around 300, 150 and 100 nm. However, it has to be pointed out that always the same concentration of LEP (i.e. 10 mg/mL) was used for spin coating to investigate the influence of the active layer thickness. That means that for different dopant concentrations, there is different total mass of LEP, DCH18C6 plus LiCF$_3$SO$_3$. Slightly different actual active layer thicknesses were generated for three dopant concentrations. The active layers at the side of substrates were wiped away by a Q-tip with toluene for later top electrode deposition. Samples were then thermally annealed at 80 °C overnight in the dark atmosphere.

For fully solution-processed yellow OLEDs, the SuperYellow LEP was dissolved in toluene with a volume concentration of 4 mg/mL. The ink was stirred at 400 RPM overnight and filtered through a PTFE-membrane syringe filter with a pore size of 1 μm before spin coating. The prepared solution was spin-coated on top of inkjet-printed EIL layer or on ITO with a spin-rate of 1000 RPM for 60 s. The active layer at the side of substrates was wiped away by a Q-tip with toluene for later top electrode deposition. EML was then

thermally annealed at 80 °C for more than 1 h. A typical layer thickness of 80 nm was deposited. Depending on the EIL layer below, a slight thickness deviation (±5 nm) was observed. Figure 4-9 shows geometric profile of spin-coated SuperYellow EML on glass and on inkjet-printed ZnO layer. On the cross-section image, the left part is pure EML, while the right part is the EML on ZnO layer. As it can be seen, the spin coating method results in a uniform and flat thin film with a RMS of ~1.2 nm for 80 nm thickness.
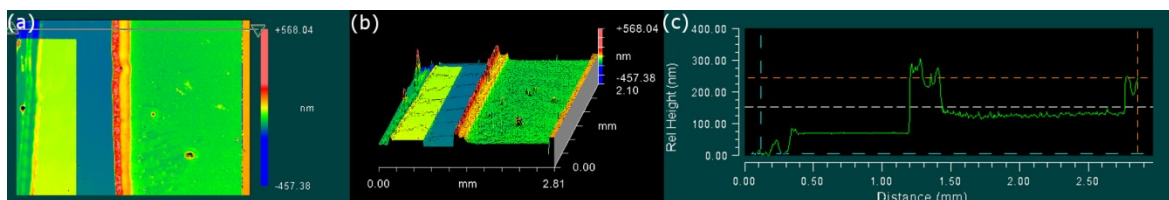

Figure 4-9 White light interferometer measurement of spin-coated SuperYellow LEP on inkjet-printed ZnO on a pre-patterned ITO glass substrate: (a) Top view, (b) 3D view, and (c) cross-section measured the thin film; The cross-section measurements were taken at the positions indicated by a line between two triangles on the 2D top view images.
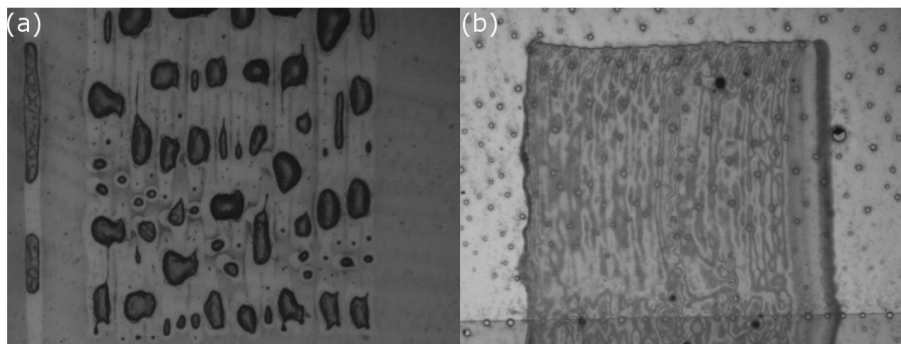
4.1.4 Inkjet printing top electrodes

Figure 4-10 Camera images of inkjet-printed single line and stripe of PEDOT:PSS with a dot spacing of 40 μm on (a) non-activated OLEC/OLED layer and (b) argon plasma activated OLEC/OLED layer.

For top electrode deposition, relatively high work-function is preferred to obtain better hole injection into the LEP. PEDOT:PSS has a work function around -5.1 eV, and the HOMO level of Merck blue LEP is -5.15 eV [197] and of SuperYellow is -5.4 eV [146]. This makes PEDOT:PSS a very good hole injection layer. Typically, the conductivity of PEDOT:PSS is really low and not sufficient to be electrode alone. Thanks to the past tremendous efforts on improving the PEDOT:PSS conductivity [31,33,34,94], it can reach the conductivities greater than 3000 S/cm [33], which is comparable to the wide-

ly used transparent anode ITO (sputtered on glass, conductivity of 6250 S/cm [153]). Commercially available inkjet-printable PEDOT:PSS (Clevios PJet HC V2) can achieve around 500 S/cm by simply inkjet printing and drying at low temperature such as 80°C. As seen in Figure 6-1, PEDOT:PSS thin films have high transparency of > 90% over the whole visible range (see Figure 6-1), which makes it a good transparent electrode.

As PEDOT:PSS ink is water-based, the inkjet-printed solution does not dissolve the underneath organic active layer, which is typically dissolvable in non-polar solvents. On the other hand, inkjet-printed organic layers yield "bad" surface wetting for inkjet printing PEDOT:PSS. As illustrated in Figure 4-10a, a single line and 1 mm wide stripe were inkjet printed from PEDOT:PSS HC V2 ink on top of spin-coated and dried OLEC/OLED active layers. However, the printed ink did not spread well to the intended areas, instead they were merged into small drops due to the low surface energy to the PEDOT:PSS ink. Thus, surface activation of active layer through short and low power argon plasma (50 W, 10 s) was necessary. Afterwards, regular lines and stripes of PEDOT:PSS can be inkjet printed on top of OLEC/OLED active layer, as illustrated in Figure 4-10b.
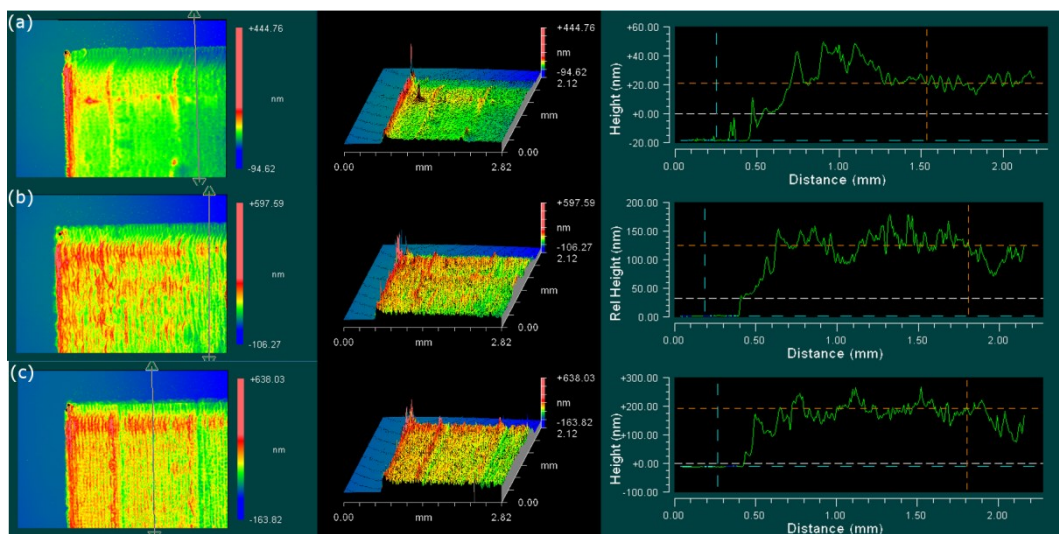

Figure 4-11 White light interferometer measurement of inkjet-printed PEDOT:PSS thin films (a) single layer, (b) two layers, and (c) three layers. Left and middle images show the 2D top and 3D view of measured structures, while right images show the cross-section of corresponding structures. The cross-section measurements were taken at the positions indicated by a line between two triangles on the 2D top view images.

Top electrodes were typically inkjet printed at 500 Hz with a dot spacing of 40 µm. The printed layer thickness is typically 40 nm, and it can be slightly deviated according to the surface wetting of underneath organic layer. In order to reduce the resistance of

PEDOT:PSS electrode and reduce the driving voltage of organic light sources, multilayer of PEDOT:PSS can be inkjet printed on top of each other. Figure 4-11 shows the geometric profile measurement results of multi-layer printed PEDOT:PSS thin films. One, two, and three layer printed thin films have layer thicknesses of 40, 95, and 124 nm, respectively. Therefore, approximately one third of resistance can be realized by three-layer printing compared to single-layer printing. Although multi-layer printing leads to a slightly rougher surface, it should have limited influence when used only for top electrodes. The same strategy can be used for PEDOT:PSS bottom electrodes, especially when OLEC devices are manufactured.

4.2 Manufacturing procedures

4.2.1 ITO-free, fully solution-processed blue OLEC manufacturing process
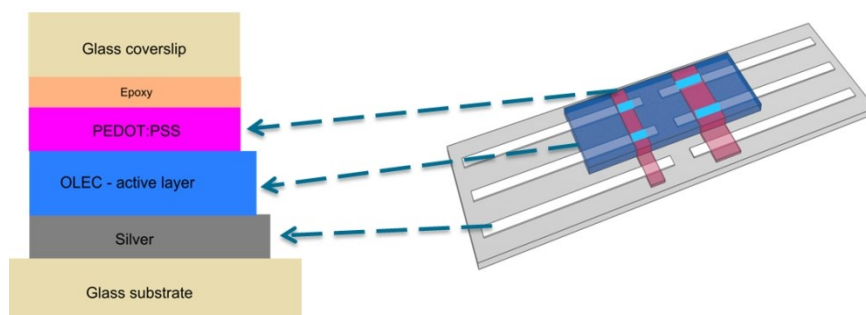

Figure 4-12 fully solution-processed OLEC layer structure diagram and 3D scheme. It has a layer stack of inkjet-printed Ag (150 – 400 nm) || spin-coated OLEC layer (410 nm) || inkjet-printed PEDOT:PSS (40 nm). Four active pixels with dimensions of 1×2 mm^2 and 1×5 mm^2.

Microscope glass slides were cleaned in a series of ultra-sonication baths with tenside agents. Afterwards, the surface was activated by low-pressure oxygen plasma (200 W, 2 min). Ag bottom cathode was inkjet printed with a dot spacing of 35 µm, and thermally sintered in a convection oven at 200 °C for 15 min. Then, 12 mg/mL OLEC ink was spin-coated with 1000 RPM, 60 s and wiped with Q-tips. The sample was then treated by low-pressure argon plasma (50 W, 30 s) to achieve good wetting for PEDOT:PSS layer deposition. A transparent conductive PEDOT:PSS layer was deposited with a dot spacing of 40 µm on top of active layer. As the device was fully fabricated in air, it was first vacuumed (5 Pa) for 15 min to get rid of diffused oxygen and water, and then encapsulated with

a UV curable epoxy, UV irradiation and a glass coverslip to prevent device degradation in air. Alternatively, the device can be encapsulated in a N_2 or Ar glovebox so that a short vacuum process can be avoided. The detailed process parameters and material are listed in Table 2.

Table 2 Overview of process parameters for manufacturing ITO-free, fully solution-processed blue OLEC

Ink formulations	Surface activation and Printing parameters	Post-treatment
Silver nanoparticle dispersion in ethanol /ethylene glycol	Acetone and isopropanol rinsing, dried by N_2 flow Inkjet-printed with dot spacing of 35 µm @ 1000 Hz	Sintered in convection oven 15 min @ 200 C
12 mg/mL Blue OLEC in toluene (LEP:DCH18C6:LiCF$_3$SO$_3$= 1:1:0.18)	Spin-coated @ 1000 RPM for 60 s	Thermal annealing on hot-plate 10 min @ 80 °C
PEDOT:PSS (Clevios PJet HC V2)	Surface activation by Ar Plasma 10 s @ 100 W Inkjet-printed with dot spacing of 40 µm @ 500 Hz	Thermal annealing on hot-plate 15 min @ 140 °C

4.2.2 Blue OLEC on ITO manufacturing process

The pre-patterned ITO coated glass substrates were used as cathodes. They were cleaned through a series of ultrasonic baths with different tensides. Afterwards, they were further cleaned and surface activated by a low-pressure oxygen plasma (2.45 GHz, V55-GKM, Plasma finish GmbH) at 200 W for 10 min [198]. The active layers were spin-coated at various spin rates (i.e. 500, 1000, and 2000 RPM) for 60 s to achieve different layer thicknesses. They were then annealed at 80 °C on a hot-plate in a nitrogen glovebox (MBRAUN Labstar, O_2 < 1 ppm, H_2O < 1 ppm). Active thin films at the sides of glass were carefully wiped away by Q-tips with toluene so that the top electrode can be later deposited. Afterwards, the OLEC was transferred outside of the glovebox, and the samples were shortly activated by low-pressure argon plasma (50 W, 10 s). The top electrodes were inkjet printed from a PEDOT:PSS ink via Uni-Jet OmniJet-100 printer (UniJet Co. Ltd, South Korea) with a Dimatix DMC printhead with 10 pL nozzles (Fujifilm Holdings Corporation). The top electrodes were inkjet printed via single nozzle at dot spacing of 45 µm. Light-emitting (over-lapped) pixels with sizes of 1×1 mm^2 or 1.5×1.5 mm^2 were realized. The PEDOT:PSS layer was then dried under vacuum (< 10 Pa) for 15 min. Alternatively, it can also be dried at 80°C on a hot-plate in a nitrogen glovebox. The samples were encapsulated with 0.7 mm thick glass coverslips, UV-curable epoxy and UV irradiation (bluepoint 2 easycure, 5000 mW/cm², 3 s). As the both electrodes are transparent, silver

mirrors were inkjet printed on the rear side of cover glass to increase the overall output light intensity. The silver mirrors were inkjet printed from silver nanoparticle with a dot spacing of 35 µm. They were then dried and sintered at a KHz low-pressure argon plasma at 240 W for 15 min [38]. For some samples, a ZnO interlayer was spin-coated on top of ITO substrates before active layer deposition. A 20 mg/mL $Zn(acac)_2$ in ethanol solution was spin coated at 1600 RPM for 45 s [155,199]. The edge was wiped away by Q-tips with DI-water to avoid electrical shortcutting. Then, the samples were thermally annealed at 120 °C for 45 s on a hot plate. These processes were under the ambient conditions unless stated.
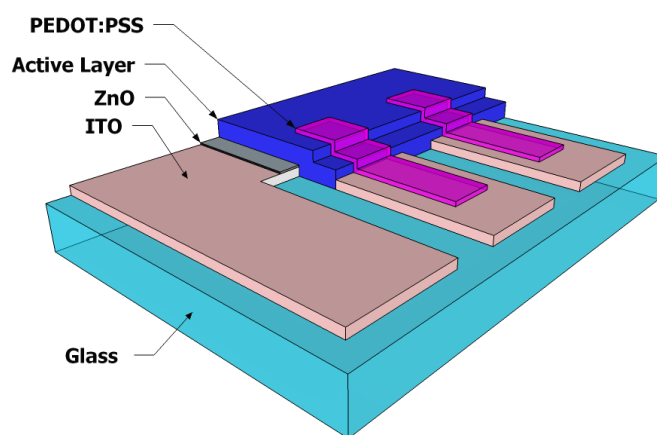

Figure 4-13 Layer architecture diagram (quarter part of full device) of fully solution-processed blue OLEC on ITO glass substrate. OLEC has an inverted layer structure of: ITO (100 nm) ‖ ZnO (20 nm) ‖ Active layer ‖ PEDOT:PSS (40 nm). Some devices have no ZnO interlayer. The active layer consists of blue LEP Merck Blue, solid electrolyte DCH18C6, and dopant $LiCF_3SO_3$.

4.2.3 Planar OLECs manufacturing process

Planar OLECs with silver and PEDOT:PSS as electrodes: Microscope glass substrates were cleaned in a series of ultrasonic baths and surface activated using low pressure oxygen plasma at 200 W for 10 min. Newly prepared OLEC inks (with Merck Blue or SuperYellow LEP) were either spin-coated (1000 RPM, 60 s) or drop-casted on substrates. Afterwards, the samples were thermal annealed at 80 °C on a hot plate for 10 min. In order to improve the surface wetting for inkjet printing, the samples were activated by low pressure argon plasma at 50 W for 30 s. Afterwards, PEDOT:PSS anodes were inkjet printed from a commercial ink (PEDOT PJet HC V2) with a dot spacing of 40 µm. Silver cathodes were inkjet printed from Suntronic silver nanoparticle dispersion with a dot spacing of

30 µm. The samples were then transferred to nitrogen glovebox and thermally annealed at 80 °C overnight before performing doping propagation experiments. The layer architecture is illustrated in Figure 4-14(a). Printing silver and PEDOT:PSS electrodes on top of active layer are to avoid the impact of electrode thickness. It has been also noticed that no doping propagation took place when printing the silver cathode first. The reason could be the thin oxidation layer on the silver surface that prevents the electrochemical doping of LEPs.
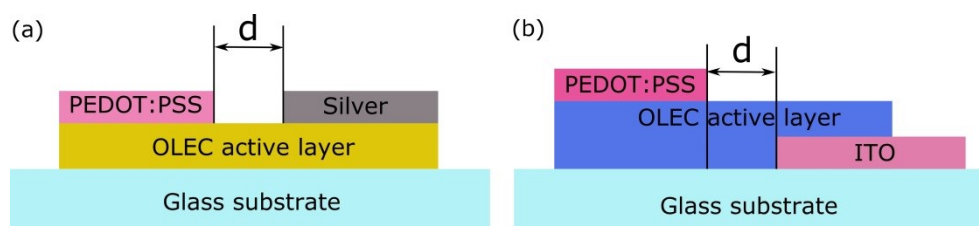

Figure 4-14 Layer architecture diagrams for planar OLECs with different electrodes: (a) Inkjet-printed PEDOT:PSS and silver; (b) inkjet-printed PEDOT:PSS and pre-patterned ITO; the active layers were drop-casted from OLEC inks based on either Merck Blue or SuperYellow LEPs; d represents the spacing between two electrodes.

Planar OLECs with ITO and PEDOT:PSS as electrodes: The pre-patterned ITO substrates were cleaned in a series of ultrasonic baths and surface activated using low pressure oxygen plasma at 200 W for 10 min. Newly prepared OLEC inks (with Merck Blue or SuperYellow LEP) were either spin-coated (1000 RPM, 60 s) or drop-casted on substrates. Afterwards, the samples were thermally annealed at 80 °C on a hot plate for 10 min. In order to improve the surface wetting for inkjet printing, the samples were activated by argon plasma with 50 W for 30 s. PEDOT:PSS anodes were inkjet printed from a commercial ink (PEDOT PJet HC V2) with a dot spacing of 40 µm. The samples were then transferred to a nitrogen glovebox and thermally annealed at 80 °C overnight before performing doping propagation experiments. The layer architecture is illustrated in Figure 4-14(b).

For both planar OLECs, d is around 300, 500 or 1000 µm. The widths of PEDOT:PSS and silver electrode strips are 1 or 1.5 mm. Pre-patterned ITO strips have a width of 1.5 mm.

4.2.4 Fully solution-processed yellow OLED manufacturing process

The pre-patterned ITO-coated glass substrates were used as cathodes, and the cleaning and activation is the same as blue OLECs. For some samples, a work-function adaption layer was inkjet printed from an Al-doped ZnO nanoparticle ink or Al:ZnO:PEI mixture. It

was printed from a PiXDRO LP50 inkjet printer (Meyer Burger B.V.) with a Dimatix DMC printhead with 10 pL nozzles. Dot spacings of 40 and 60 µm were used to produce different layer thicknesses. The Al:ZnO layer was thermally annealed at 150 °C for 30 min in a convection oven, while the Al:ZnO:PEI layer was at 110 °C. The SuperYellow LEP was dissolved in toluene with a volume concentration of 4 mg/mL. The ink was stirred at 450 RPM overnight before using. The active layers were deposited via spin-coating at a spin-rate of 1000 RPM for 60 s. They were thermally annealed at 120 °C for 15 min on a hot-plate (in the nitrogen glovebox). It resulted in a layer thickness of 80 nm. Active thin films at the sides of substrates were carefully wiped away by Q-tips with toluene so that the top electrode can be later deposited. The samples were shortly activated by low-pressure argon plasma (50 W, 30 s), and the top electrodes were inkjet printed from a PEDOT:PSS ink via the Uni-Jet OmniJet-100 printer with a Dimatix DMC printhead with 10 pL nozzles. The top electrodes were inkjet printed via single nozzle at dot spacing of 45 µm. Light-emitting (overlapped) pixels with sizes of 1×1 mm^2 were realized. The PEDOT:PSS layer was dried at 120°C on a hot-plate in a nitrogen glovebox. Some samples were encapsulated with 0.7 mm thick glass coverslips, UV-curable epoxy and UV irradiation (bluepoint 2 easycure, 5000 mW/cm², 3 s). The whole processes were under the ambient conditions except stated.

The ITO-free yellow OLEDs were fabricated on microscope glass slides. They were cleaned in a series of ultrasonic baths and surface activated using low-pressure oxygen plasma at 200 W for 10 min. For increasing conductivity and improving the electrical contacting, silver wirings were inkjet printed from silver nanoparticle dispersions with a dot spacing of 35 µm. The wirings were thermally sintered at 200 °C for 30 min in a convection oven. For low processing temperature, the thermal sintering can be replaced by the argon plasma sintering with a KHz generator. Afterwards, bottom electrodes were inkjet printed from a silver-nanowire-embedded PEDOT:PSS ink (Clevios PEDOT HY) with a dot spacing of 40 µm. A layer thickness of 100 nm was achieved from two-layer printing. The printed PEDOT:PSS electrodes were thermally annealed at 120 °C for 15 min. The rest of manufacturing process is the same as solution-processed yellow OLED on ITO substrates.

4.2.5 Tandem OLED and OLEC manufacturing process

The patterned ITO was first cleaned by a series of tenside ultrasonic baths. It was then activated by low-pressure oxygen plasma for 2 min at 200 W. The ZnO precursor was dissolved in ethanol with a concentration of 20 mg/mL, and it was stirred overnight at 60 °C. A 40 nm thick ZnO layer was deposited by spin-coating at 1500 RPM for 60 s, and followed by a thermal annealing of 130 °C for 30 s on a hot-plate. The 0.4 w% PEI was dissolved in ethanol and spin-coated at 5000 RPM to form an ultra-thin layer (~10 nm). Thermal annealing took place on a hot-plate set to 120 °C for 10 min. 4 mg/mL SuperYellow LEP was dissolved in toluene, and a 80 nm thick EML was deposited by spin-coating at 1000 RPM for 60 s. An approximately 40 nm thick PEDOT:PSS top electrode is deposited by inkjet printing with a dot-spacing of 40 μm. It was thermally annealed at 120 °C for 15 min on a hot-plate. Afterwards, another ZnO layer and PEI were spin-coated as described above. A 300 nm thick active layer is deposited on top of ITO by spin-coating a 10 mg/mL Merck Blue OLEC ink (mass ratio of $LEP:DCH18C6:LiCH_3SO_3 = 1:0.1:0.028$) at 1000 RPM for 60 s. The PEDOT:PSS top electrode was inkjet printed with the same parameters. Finally, the device is encapsulated with epoxy and glass coverslip after a short vacuum drying. This entire manufacturing process is operated under ambient conditions.

4.3 Device characterization methods

4.3.1 Electrical characterization method

The current – voltage characterization was measured via a YOKOGAWA GS610 source measure unit. The samples were driven at DC voltage mode and currents were measured. The voltage was swept from 5 to 10 V with a resolution of 50 mV three times and average results were used for analyzing. The currents measurement had a 500 μs delay to avoid initial electrical spikes due to voltage changes.

The OLEC/OLED devices were driven at constant voltage pulse to achieve relatively high brightness. In spite of constant current driving mode, the constant voltage-driving mode was decided for easy usage for standard mobile power supplies. A HAMEG HMP2020 power supply was used to source voltage pulse with arbitrary function. It has time resolution of 10 ms and max voltage output of 32 / 64 V (two channels in series connection) with a one mV resolution. Trek's Model 2210 power amplifier was used to

achieve fast high voltage / power output. 100 V/V voltage gain and 150 V/μs slew rate can be achieved. The current was measured by a pico-amperemeter (Keithley 6485 picoammeter) with resolutions of 2 ms and 10 fA.

The pulse driving power supply was characterized by an oscilloscope (WaveJet 354A, Teledyne LeCroy) to observe the initialization speed of the driving electronics and OLECs. As the HAMEG HMP2020 power supply has intrinsically programmable voltage/current waveform function, it was tested first in open-circuit mode. It can be seen from Figure 4-15 that the power supply has very slow voltage increasing and return rate, even at open-circuit mode, at 20 V and 60 V voltage pulses. The set 80 ms pulse turned into 220 ms (35 ms at 20 V) and 285 ms (13 ms at 60 V) pulses. To generate a 60 V pulse, the power supply has only 0.78 V/ms rising ratio and 0.31 V/ms return ratio, which is far away from the requirement.
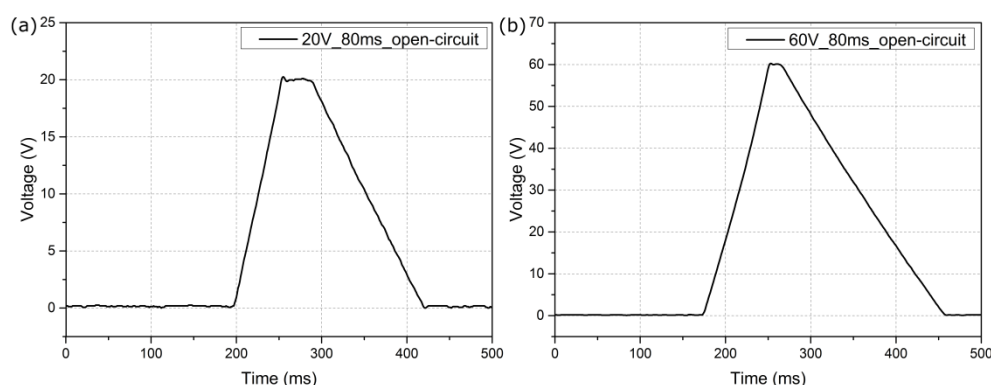

Figure 4-15 The recorded oscilloscope waveform images of 80 ms electrical voltage-pulse generated by HAMEG HMP2020 power supply at (a) 20 V and (b) 60 V at open-circuit.

Therefore, a combination of power supply and power amplifier was selected to drive the OLECs. As the power amplifier has a voltage gain of 100 V/V, only 0.6 V pulse should be set up to realize a 60 V voltage pulse. From Figure 4-16, it can be seen that the new driving setup has a 20 V/ms rising rate and 14.9 V/ms return rate, which is sufficient to provide a precise voltage pulse in 10 ms to 200 ms range. When an OLEC sample is driven by the setup at a 40 V pulse, it shows a rising rate of 2.2 V/ms and return rate of 3.5 V/ms. It is clearly demonstrated that OLEC samples are slower than driving electronics, which are sufficient to drive the samples for characterization.
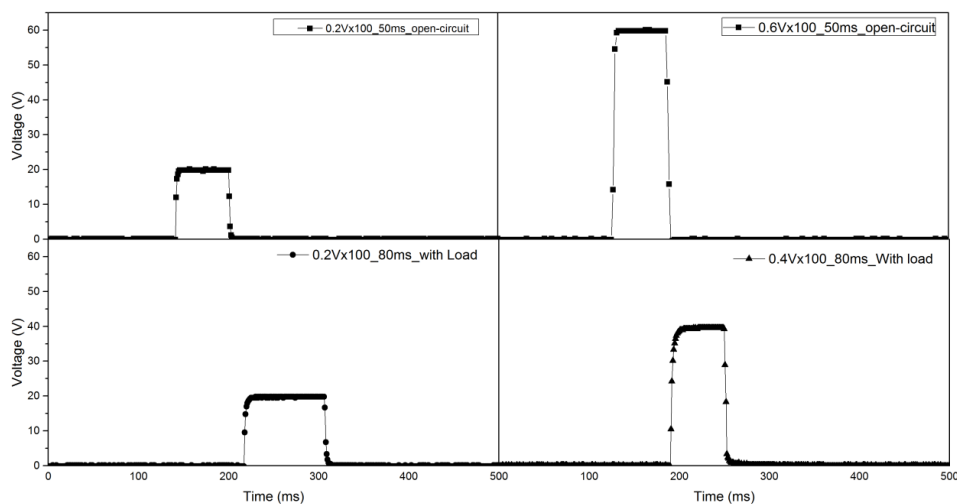
Figure 4-16 The recorded oscilloscope waveform images of electrical voltage pulse generated by HAMEG HMP2020 power supply and power amplifier. The first row show 50 ms pulses with open-circuit mode and the second row shows 80 ms pulses loaded with an OLEC sample.

4.3.2 Optical measurement method

The light brightness was measured by a silicon photodiode (Centronic OSD50-E) with an eye filter (Schott OG515) to simulate the visible light sensitivity of human eyes. The photocurrent was recorded by a Keithley 6485 picoammeter with a self-made Lab-VIEW program. Due to the limitation of the picoammeter, the measurement has a maximum time resolution of 2 ms and measurement duration of five s (maximum 2500 measurement points). The Si-photodiode with an eye filter was calibrated with a green Laser diode. The brightnesses calculated followed the principles described in light measurement handbook [200]. For verifying the measurement results, some samples were measured by a luminance camera luca (opsira GmbH). Same brightnesses have been measured for both measurement methods. The electroluminescent spectra were measured by an optical fiber coupled calibrated spectrometer (SD2000, Ocean Optics Inc., wavelength resolution of 2 nm). For I-V-L curve measurement, I-V curves of the samples were measured as described in section 4.3.1 while the light-emitting photocurrents were simultaneously recorded via a silicon photodiode with an eye filter. The brightnesses were then calculated and synchronized with I-V curve measurement.

5   Fully solution-processed OLED investigation

In this chapter, device characterization of solution-processed yellow OLEDs with inkjet-printed interlayers of Al-doped ZnO mixed with PEI (Al:ZnO:PEI) was demonstrated. As described in the theoretical section, the work-function adaptation from both the anode and cathode sides as well as electron and hole confinement within the active layer are very important to realize high-performance OLEDs. The traditional multi-layer system and ultrathin-layer manufacturing of OLEDs are not practical for cost-efficient on-chip sensing applications. Hence, to meet application needs, I introduce a directly inkjet-printed interlayer from Al-doped ZnO nanoparticle ink mixed with PEI. This one-step EIL deposition method has never been reported in literature. Therefore, with layer architecture of ITO ‖ Al:ZnO:PEI ‖ LEP ‖ PEDOT:PSS (see Figure 5-1), I provide a novel solution for the application-oriented requirements:

1.   Simplified layer architecture for full solution processing
2.   Mask-free inkjet printing
3.   Vacuum-free manufacturing
4.   Low temperature ($< 120\ °C$) for thermal sensitive substrates
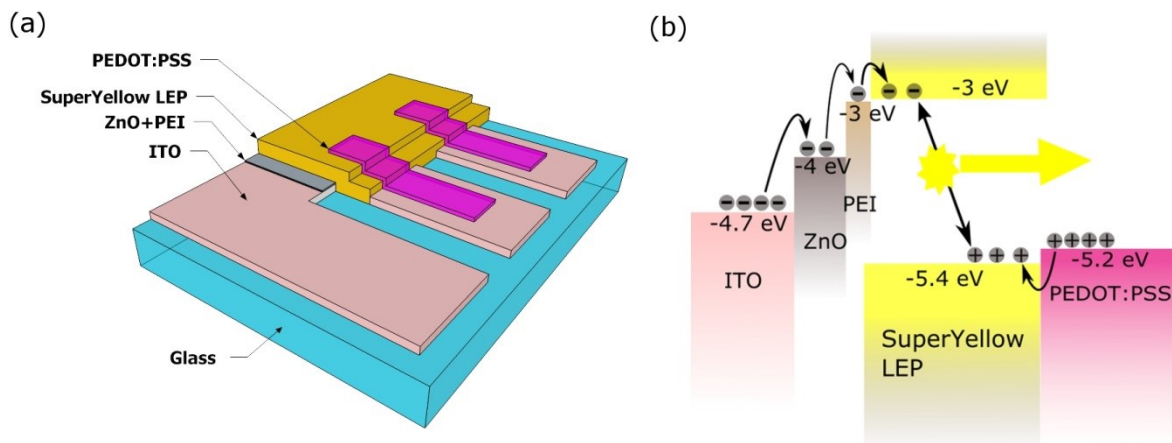
5.1   Electrical and optical characterization

Figure 5-1 (a) Layer architecture and (b) energy level diagram (quarter part of full device) of fully solution-processed yellow OLED on pre-patterned ITO glass substrate. It has inverted layer structure of ITO (100 nm) ‖ EIL (various) ‖ SuperYellow LEP (80 nm) ‖ PEDOT:PSS (40 nm).

In order to investigate the influence of different EIL layers on device performance, several OLEDs were fully solution processed with an EIL layer consisting of: a) inkjet-printed Al-doped ZnO layer; b) inkjet-printed Al-doped ZnO mixed with PEI layer, 21 nm thick; c) inkjet-printed Al-doped ZnO mixed with PEI layer, 53 nm thick; and d) no EIL for reference. That same pre-patterned ITO (100 nm) and inkjet-printed PEDOT:PSS (40 nm) were used for bottom cathode and top anode. SuperYellow LEP was used for the active layer with the same processing parameters. The detailed manufacturing process is described in section 4.2.4. Table 3 summarizes the layer architectures of four OLED devices used in this chapter.

Table 3 Layer architecture, driving voltage and current efficiency at 500 cd/m^2 of OLED devices with different inkjet-printed EIL layers, investigated in this chapter.

	Layer architecture	Driving voltage (at 500 cd/m^2)	Current efficiency (at 500 cd/m^2)
Device A	ITO ‖ Al:ZnO (40 nm) ‖ SY LEP (85 nm) ‖ PEDOT:PSS	10 V	0.62 cd/A
Device B	ITO ‖ Al:ZnO:PEI (53 nm) ‖ SY LEP (93 nm) ‖ PEDOT:PSS	6.84 V	2.55 cd/A
Device C	ITO ‖ Al:ZnO:PEI (21 nm) ‖ SY LEP (84 nm) ‖ PEDOT:PSS	6.9 V	1.53 cd/A
Device D (Reference)	ITO ‖ SY LEP (84 nm) ‖ PEDOT:PSS	-	-

Figure 5-2 illustrates the V-L curve and J-V curve of the fully solution-processed OLED samples. As no light emission can be detected at driving voltage of 10 V, device D is not plotted in Figure 5-2a. From the current - voltage characterization, it can be seen that there is a dramatic increase of current by Al-doped ZnO EIL only. Device B and C with Al:ZnO:PEI EIL show even higher current density at the same driving voltage as device A, which means better electron injection (lower work function barriers) from the cathode side compared to pure Al-doped ZnO EIL. This fits the theory of the work-function adaptation for electron injection from cathode side very well. More specifically, SuperYellow LEP has a LUMO level of -3.0 eV [146], while ITO, ZnO and PEI on ZnO have work functions of -4.7, -4 and -3 eV, respectively (see Figure 5-1b). Hence, work-function barriers for devices A, B&C and D are 1.0 and 0.0, and 1.7 eV. Thus, much more electrons can be injected into device though a ZnO layer and furthermore through a ZnO and PEI mixed layer. A higher electron injection rate also means a higher electron and hole combination rate. According to equation (3.2) in theoretical section 3.1, this ultimately means higher emission efficiency can be achieved. The plotted results of V-L characterization in Figure 5-2

meet the prediction from the theory: No light can be emitted from reference device D; modest light can be emitted from device A with ZnO EIL only; close to 3000 cd/m^2 brightness at 10 V can be emitted by device B and C.
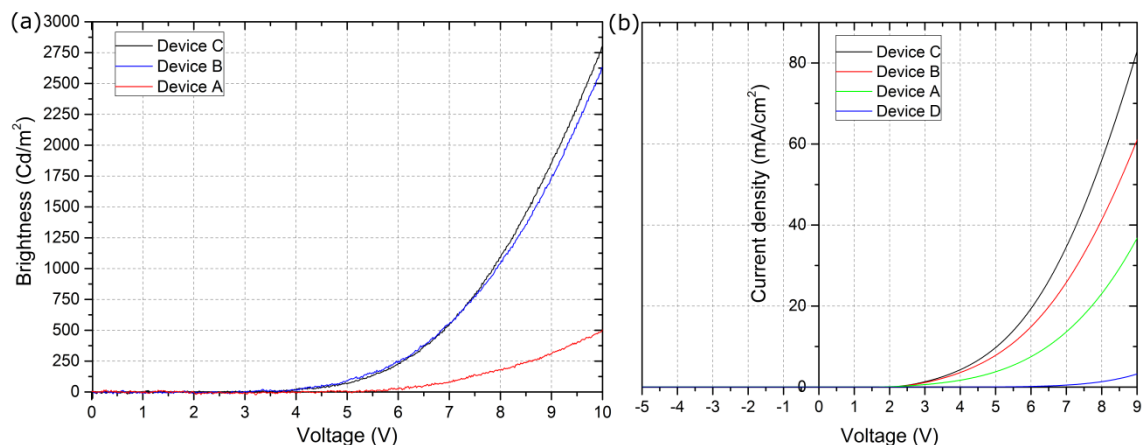

Figure 5-2 (a) Voltage-brightness (V-L) curve and (b) voltage - current density (V-j) curve of fully solution-processed yellow OLEDs (device A, B, C and D) with different inkjet-printed electron injection layers. The light-emitting brightness was measured from the top electrode PEDOT:PSS only.

In contrast to the traditional requirement of ultrathin PEI interlayer, the inkjet-printed Al:ZnO:PEI interlayer as thick as 53 nm shows close performance to 21 nm thin layer. Device B even has better current efficiency than device C with thinner Al:ZnO:PEI EIL. The reason for this could be the good electrical conductivity of EIL, thanks to the Al doping and better electron and hole injection balance due to thick EIL, in particular at low driving voltage.
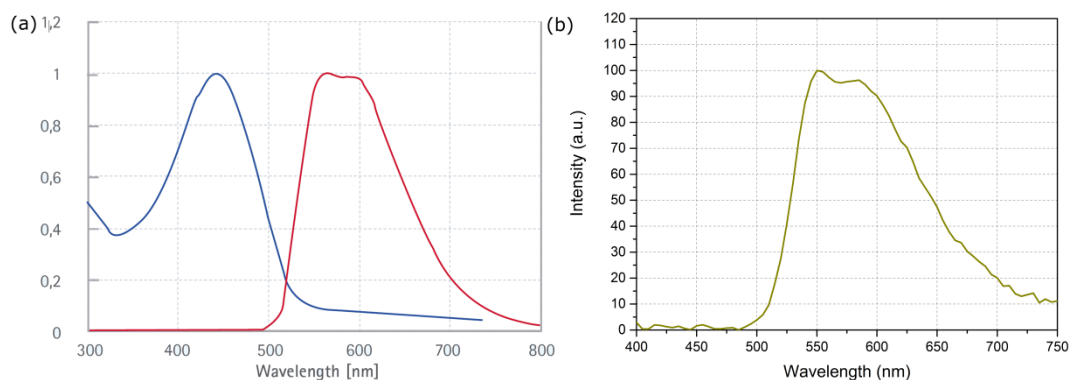

Figure 5-3 (a) Electroluminescent emitting spectra (red) and photoluminescent absorption spectra (blue) of OLEDs with layer architecture of ITO || PEDOT:PSS (20 nm) || SuperYellow LEP (80 nm) || Ba (6 nm) || Ag (150 nm) [201]; (b) Electroluminescent emitting spectra of fully solution-processed transparent SuperYellow OLED fabricated in Fraunhofer IOF.

       The electroluminescent spectrum of fully solution-processed OLEDs was also measured in-house. The spectrum is plotted in Figure 5-3 as well as the spectra from the datasheet provide from Merck. The spectra provided from Merck were measured from an OLED with layer architecture of ITO ‖ PEDOT:PSS (20 nm) ‖ SuperYellow LEP (80 nm) ‖ Ba (6 nm) ‖ Ag (150 nm). The PEDOT:PSS layer and LEP were spin-coated, while Ba and Ag layers were thermally evaporated under high vacuum. The spectrum of the fully solution-processed transparent SuperYellow OLEDs is almost the same as the reference OLEDs from Merck. This indicates that the light was generated from the light-emitting polymer and all the other layers have almost no substantial influence on the light-emitting spectrum.
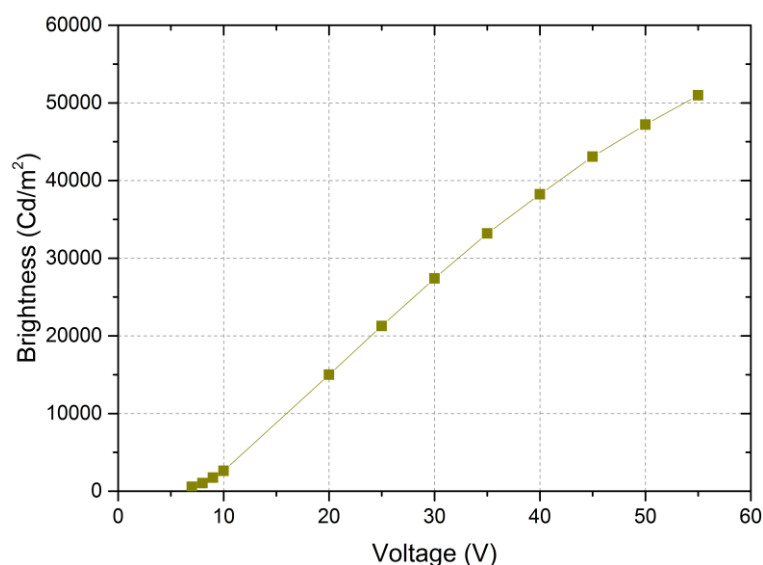

Figure 5-4 Voltage – brightness curve of fully solution-processed yellow OLED device B (1×1 mm^2 pixel size) operated at voltage-pulsed mode. The voltage pulses have a pulse-width of 20 ms and 1% duty cycle. The light-emitting brightness was measured from the top electrode PEDOT:PSS only.

       Due to its relatively high current efficiency, OLED Device B was pulse-operated at a high voltage to obtain a high brightness (Figure 5-4). An emission brightness driven at up to 10 V was taken from the continuous V-L curve measurement. From 20 to 55 V, the sample was operated at voltage-pulsed operation mode with pulse-width of 20 ms and a 1% duty cycle. With 1×1 mm^2 pixel size, the fully solution-processed transparent yellow OLED can emit extremely high light intensity with more than 50 000 cd/m^2. This is comparable with solution-processed OLED with evaporated Al/Ag electrode [28], and much better than the literature-reported device with similar layer stack (ITO ‖ ZnO ‖ PEI ‖ SuperYellow LEP ‖ MoO$_3$ ‖ PEDOT:PSS) [27]. It has to be pointed out that the device is

also transparent and with PEDOT:PSS top electrode, an HIL made of MoO_3 was still used and thermally evaporated. The highest emission brightness that reported in literature [19] is 1.86×10^6 cd/m^2, however the OLED was fully evaporated and has a tiny round pixel with a radius of 50 μm. Moreover, the pixel was pulsed at a pulse-width of 5 μs and 10% cycle duty to avoid fast degradation.

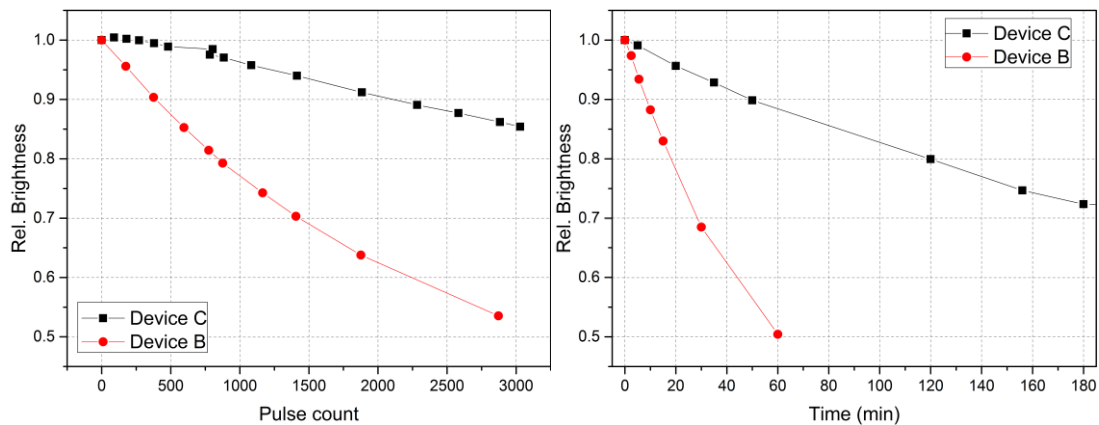## 5.2 Lifetime characterization

Figure 5-5 Lifetime characterization of fully solution-processed transparent yellow OLEDs (device B and C). Both OLEDs were (a) pulse-driven at 20 V with a pulse-width of 20 ms and 5% duty cycle, and (b) DC driven at a current density of 20 mA/cm^2.

In order to use the fully solution-processed yellow OLEDs as the excitation light source for on-chip fluorescence sensing applications, appropriate operational lifetime is required. As the device with an Al:ZnO:PEI EIL has much better emission efficiency, they were operated at stressed conditions to test the operational lifetime. In the target applications, the OLEDs will be operated in pulsed mode in order to get high brightness and high sensitivity. Thus, the OLEDs device B and C were first operated continuously at voltage-pulsed driving conditions of 20 V with a 50 ms pulse-width and 5% duty cycle. The results are illustrated in Figure 5-5a. At a 20 V driving voltage, Device C has an initial brightness of 13 600 cd/m^2, while OLED device B has an initial brightness of 11 800 cd/m^2. After 3000 pulses, the device C has more than 85% of its initial brightness, while Device B can only emit slightly more than 50% of its initial brightness. To confirm the results, the different pixels of both devices were driven in DC current mode with a current density of 20 mA/cm^2, and emission brightnesses were measured over time. The results are plotted in Figure 5-5b. It was found that the device lifetime in DC mode shows the same trends as the

pulsed mode. Device B with a thinner EIL has better lifetime than device C with a thicker EIL. More specifically, device B has LT50 of 60 min, while Device C has LT85 of 3 h. The reason for this could be the leakage current difference for the two devices with different EIL thicknesses. Nevertheless, both devices exhibited enough operational lifetimes for disposable on-chip sensing applications at an emission brightness of more than 10 000 cd/m^2.

5.3 ITO-free, fully solution-processed OLED

As discussed in section 4.1.1, it is possible to replace the ITO bottom electrode with the combination of a PEDOT:PSS electrode and a work-function adaptation layer. In the previous sections, the Al:ZnO:PEI interlayer has demonstrated significant work-function reduction and emission brightness improvement. Hence, in this section, I replace the pre-patterned ITO electrode with a transparent PEDOT:PSS electrode. Consequently, the OLEDs can be directly printed on microfluidic chips without any costly patterning techniques and vacuum-based manufacturing techniques. The manufacturing process is described in section 4.2.4. Compared to the OLED samples in the previous section, the ITO bottom electrode was replaced with a PEDOT:PSS electrode. In order to reduce the influence of lower conductivity of PEDOT:PSS, an inkjet-printable silver-nanowire (AgNW) embedded PEDOT:PSS ink was used to deposit bottom and top electrodes. A conductivity of ~3000 S/cm was measured from an inkjet-printed thin film.

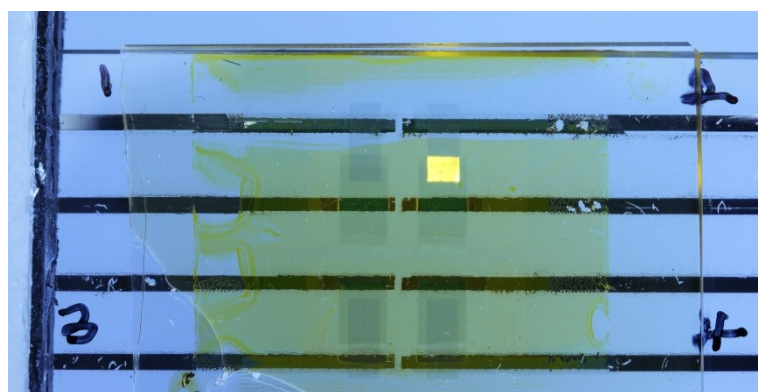Figure 5-6 Photographs of an ITO-free, fully solution-processed yellow OLEDs with four pixels (2 × 1.5 mm^2). The pixel is illuminating by driving at 10 V. It has a layer structure of PEDOT:PSS + AgNW ‖ Al:ZnO:PEI ‖ SuperYellow LEP ‖ PEDOT:PSS + AgNW.

Figure 5-6 depicts the photograph of an ITO-free, fully solution-processed yellow OLEDs on glass substrates. Pixel 2 with an active area of 2×1.5 mm² illuminates bright yellow light under a driving voltage of 10 V. Except the active layer was spin coated, all the other layers were inkjet printed. It clearly demonstrates that, with inkjet printing technique, OLED can be directly integrated onto substrates with flexible design and locations. For characterizing the electrical and optical performance, the j-V curve and V-L curve were also measured. The results are illustrated in Figure 5-7. Compared to the OLED samples on ITO (Figure 5-2), the ITO-free sample had much higher current density at the same driving voltage. It is because of high dark current, which can be seen under the reverse-biased mode. At the driving voltage of -5 V, the OLED sample had a current density of -4.66 mA/cm², while device C had -0.016 mA/cm². The reason for this high dark current density is the high roughness of inkjet-printed PEDOT:PSS layer. The ITO-free OLED sample was also tested at voltage-pulsed mode to achieve high emission brightness. A brightness of >10 000 cd/m² can be emitted at 30 V voltage pulse, while 16 000 cd/m² at 40 V. It has to be pointed out that a significant current density (e.g. ~800 mA/cm²) was measured at high voltage pulses (e.g. 30 V). Consequently, a much higher brightness could be realized when a bottom electrode with higher surface homogeneity can be inkjet printed.
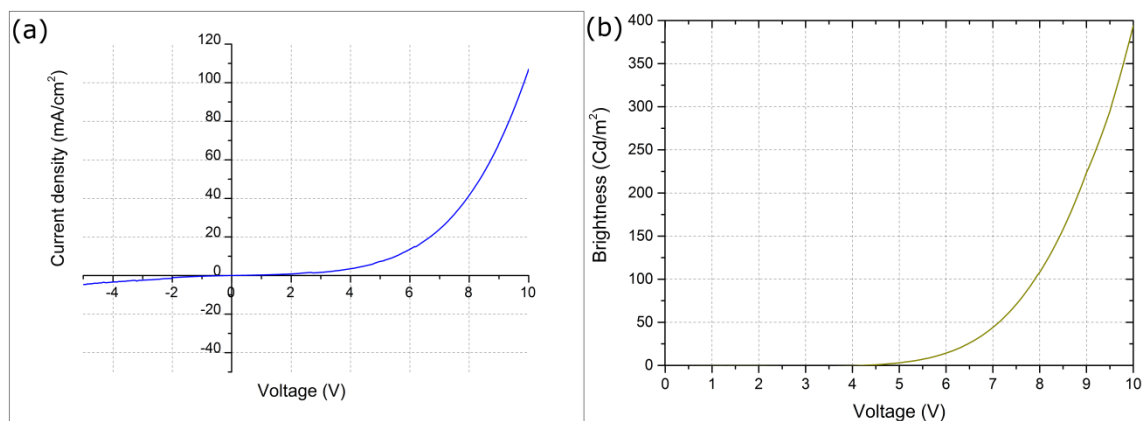
Figure 5-7 (a) Voltage - current density (V-j) curve and (b) voltage-brightness (V-L) curve of the ITO-free, fully solution-processed yellow OLEDs. The light-emitting brightness was measured from the top electrode PEDOT:PSS only.

To summarize this chapter, I have demonstrated that fully solution-processed transparent yellow OLEDs with a simple layer stack can be realized via inkjet-printed EIL, PEDOT:PSS top electrode and spin-coated EML. Moreover, a simple mixture of PEI into Al-doped ZnO nanoparticle ink can be directly inkjet printed and used as an efficient EIL. This method provides several advantages: 1) simplified manufacturing as a single layer is

required instead of two; 2) mask-free inkjet printing that avoids creating an ultrathin PEI layer; 3) cost-efficient production due to low processing temperatures (< 120°C) and vacuum-free processes. Although the devices were fabricated at ambient conditions and solution processed, light as bright as > 50 000 cd/m^2 can be emitted at pulsed driving conditions and lifetime of more than 3000 pulse (LT85) can be realized at a brightness of >10 000 cd/m^2. For the target application of providing an excitation light source for disposable lab-on-a-chip systems, the device brightness and operation lifetime are sufficient. Finally, an ITO-free, fully solution-processed yellow OLEDs was also fabricated by replacing ITO with an AgNW-embedded PEDOT:PSS electrode. A brightness of >16 000 cd/m² can be realized driving under a 40 V voltage-pulsed mode.

6 Pulsed blue OLEC device performance investigation

In this chapter, a fully solution-processed blue OLEC with a layer stack of an inkjet-printed Ag ‖ a spin-coated OLEC layer ‖ an inkjet-printed PEDOT:PSS was first demonstrated. It proved that a fully solution-processed OLEC could be a good light excitation light source on rough and less homogeneous surfaces. The influences of the material composition and layer thicknesses on pulse driving mode and light brightness were further investigated. For comparability and reproducibility, inkjet-printed silver electrode was replaced by an ITO electrode. Furthermore, a ZnO layer was also investigated for improving the light brightnesses and a strategy for replacing ITO.

6.1 Material characterization
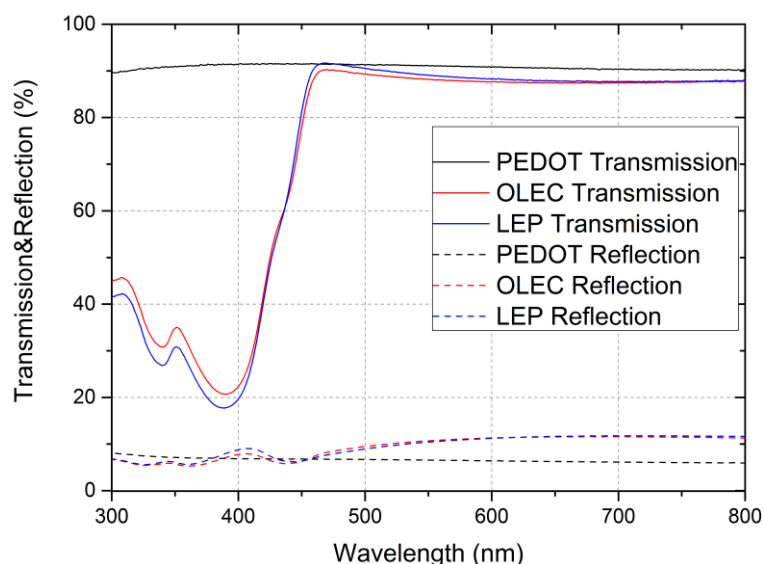
Figure 6-1 Transmission (strange lines) and reflection (dashed lines) spectra of spin-coated PEDOT:PSS (black), blue LEP (blue) and blue OLEC (red) thin films on fused silica glass. The thicknesses of PEDOT:PSS, blue LEP and blue OLEC thin films are: 46 nm, 119 nm, and 115 nm, respectively. The measurement was performed at an incident light angle of 6 degree.

First of all, material properties were examined to understand if there is intrinsic difference in optical performance between OLED and OLEC. Hence, pure blue LEP (Merck Blue) solution and blue OLEC solution (LEP : DCH18C6 : LiCF$_3$SO$_3$ = 1:1:0.2) were spin-coated on top of glass substrates. PEDOT:PSS ink was also spin-coated for reference. The spin-coated PEDOT:PSS, blue OLEC and blue LEP had thin film thicknesses of 46 nm, 119 nm, and 115 nm, respectively. The optical transmission and reflection spectra were

measured by a spectrometer and are plotted in Figure 6-1. The PEDOT:PSS thin film demonstrates high optical transparency (> 90% light transmission) over visible range. OLEC and LEP thin films have almost identical spectra, while the small difference could be due to the thin film thickness difference and mixed dopants. Nevertheless, the additional dopants have limited influences on the optical spectra. The refractive index (n) and the extinction coefficient (k) were measured and calculated. As shown in Figure 6-2, OLEC and LEP thin films have rather close refractive index and extinction coefficient. They both have refractive index of ~1.75 between 400-500 nm, which is fitting the theory of n = 1.7 for most organic materials. As both LEP (119 nm) and OLEC (115 nm) had similar thin film thickness, the slightly lower extinction coefficient clearly shows the less LEP material due to the additional dopant materials. For this reason, the investigation in section 6.4, the same spin-rates were used to ensure the same LEP contents between different dopant concentrations instead of same actual layer thicknesses. Besides, the PEDOT:PSS layer has close refractive index to glass (typically, 1.5), in particular at the wavelength close to 500 nm. Large refractive index different between PEDOT:PSS and LEP could result in low light out-coupling efficiency from LEP to PEDOT:PSS. On the other hand, ITO has much higher refractive index that helps light traverses into ITO from LEP, but it could have an out-coupling issue between ITO and glass interface.
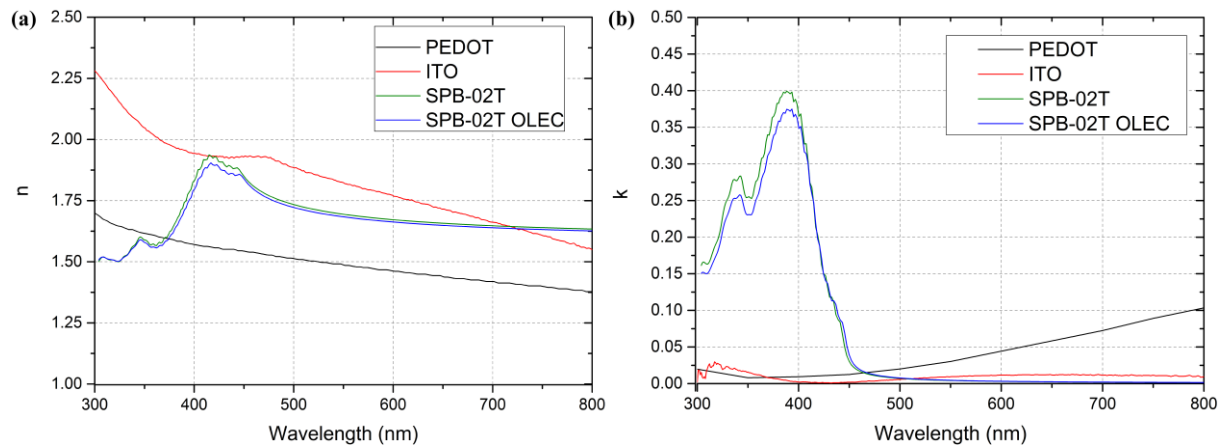

Figure 6-2 (a) Refractive index n and (b) extinction coefficient k spectra of PEDOT (black), ITO (red), blue LEP Merck Blue (green) and blue Merck Blue OLEC (blue) thin films. The data of ITO was provided by substrate supplier Ossila, Ltd..

6.2 ITO-free, fully solution-processed blue OLEC

As described in section 2.3, OLEC has the advantages of relatively simply three-layer architecture, possibilities of using air-stable cathodes such as Ag and Al, and fully solution-processing ability at ambient conditions. Consequently, a blue OLEC can be fabricated with a layer stack of an inkjet-printed Ag cathode ‖ a spin-coated OLEC layer ‖ an inkjet-printed PEDOT:PSS anode. The processing parameters are listed in Table 2 and detailed described in section 4.2.1. The details of optimization of manufacture process and material are detailed in section 4.1.
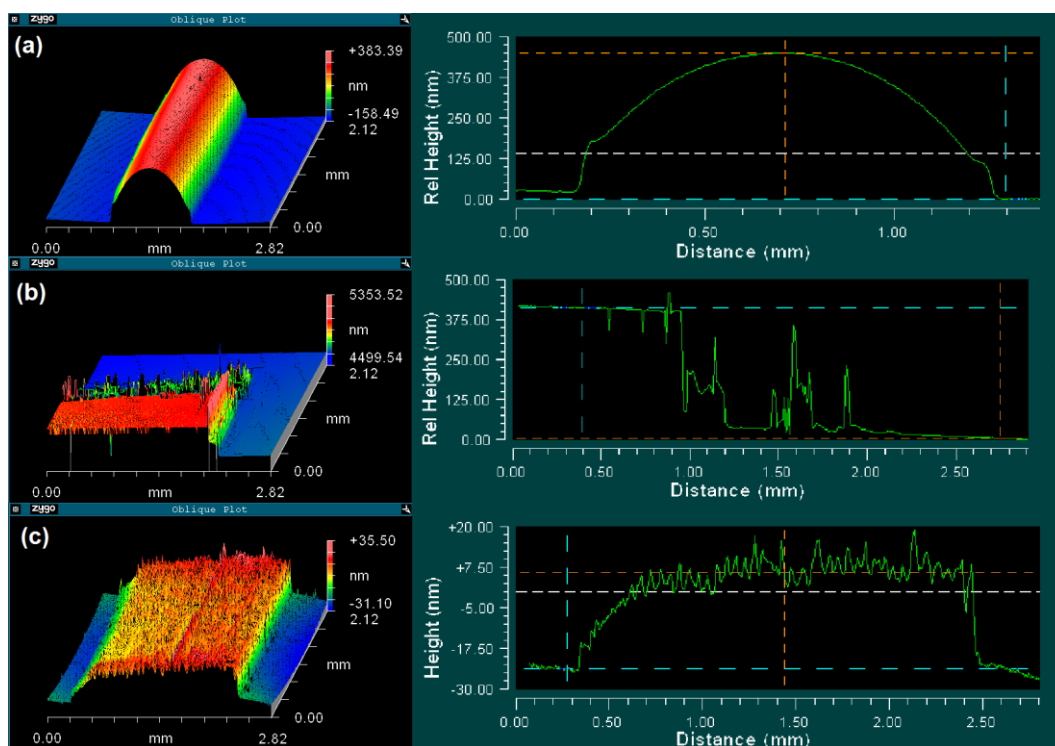
Figure 6-3 White light interferometer measurement of (a) an inkjet-printed Ag bottom cathode, (b) a spin-coated OLEC active layer, and (c) an inkjet-printed PEDOT:PSS top anode.

After each layer deposition and curing, their surface profiles were scanned by a white light interferometer (see Figure 6-3). It can be seen that the bottom cathode, which was inkjet printed from a silver nanoparticle ink, has a line-width of about 1 mm and peak height of 450 nm. Moreover, it has a thickness deviation from 125 to 450 nm from edge to center. The surface profile was not optimized so that a more flat surface was deposited in order to demonstrate that OLEC has relatively high tolerance in active layer thickness and underneath surface flatness. After spin coating the OLEC ink under ambient condition, a homogeneous layer with ~410 nm thickness was deposition on top of silver cathode. Com-

pared to typical OLED devices which require EML thinner than 100 nm, OLEC devices can work with much higher thickness (e.g. 410 nm in this case). Thus, it has higher tolerance in dust, defects and surface roughness. The top transparent anode was deposited by inkjet printing and had a relatively good thin film with about 40 nm height.

In order to make the OLEC work, the P-i-N junction within active layer should be *in situ* generated by electrochemical doping. Thanks to the solid electrolyte DCH18C6, which only has ions mobility at temperature higher than 60 °C, the P-i-N junction can be generated by heating the sample at 80 °C and biased at 7 V. Afterwards the generated junction can be frozen via cooling the sample to room temperature while keeping the electrical bias [202]. After doping, the OLEC showed similar behavior like OLEDs, i.e. fast turn-on. Figure 6-4 shows the optical imaging of working pixels for both pixel dimensions (i.e. 1 × 2 and 1 × 5 mm^2). The whole pixel areas were able to emit blue light and no large brightness difference, although there is a big thickness deviation due to the silver cathode printing. The J-V curve from Figure 6-5 conforms that OLEC shows typical diode behavior after doping. In addition, the electro-luminescence spectrum of blue OLEC shows it has peak wavelength of 475 nm, which fits the typical excitation light wavelength for common chemical-/biological fluorescence sensing application, e.g. PH value detection by probe Carboxyfluorescein.
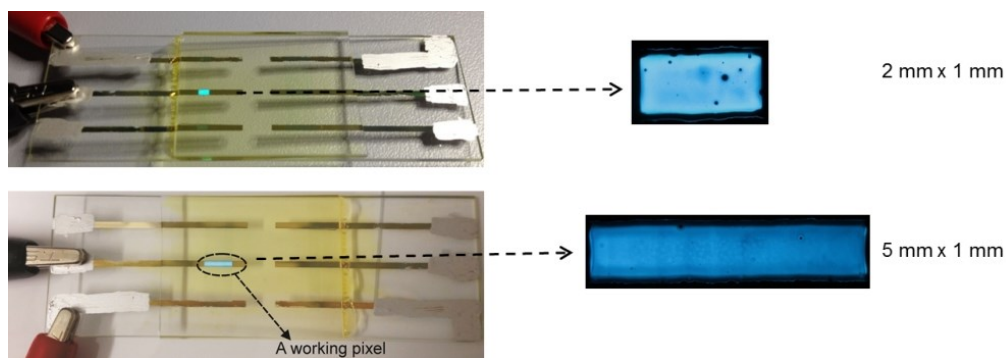
Figure 6-4 Photographs of a fully solution-processed blue OLEC with two illuminating pixels (2 × 1 and 5 × 1 mm^2).

The brightness measurement showed that the maximum brightness was 377 cd/m^2 (at 15 V) when the device was operating at the continuous mode. It had a current efficiency of 0.31 cd/A. This is however not bright enough as an excitation light source for basic on-chip fluorescence sensing applications.
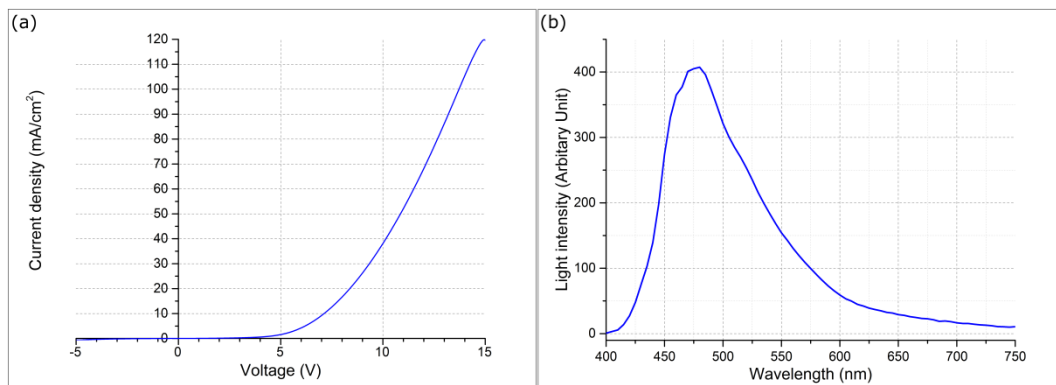
Figure 6-5 (a) J-V curve and (b) electro-luminescence spectrum of fully solution-processed OLECs.

Instead of driving the device at DC mode, the OLEC device can also be driven at voltage-pulsed mode. Especially for the target applications, the excitation light source for disposable lab-on-a-chip system is not necessary to have high emission brightness over a long period. On the contrary, a short and intense excitation light is required for on-chip fluorescence sensing. For this reason, voltage-pulsed driving mode is preferred. In addition, this brings the benefits of longer operation lifetime and higher brightness. Therefore, the ITO-free, fully solution-processed blue OLEC was pulsed at high voltages (up to 50 V) with a pulse-width of 100 ms and 1% duty cycle. The results are plotted in Figure 6-6a. Even with a relative large pixel area of 5 mm^2, a brightness of > 1100 cd/m^2 can be emitted at 50 V. It has to be emphasized that the device has higher leakage current due to the inhomogeneous Ag electrode and therefore lower overall emitting brightness at high voltages. Running the device at high voltages causes the current to flow mostly through the thinnest sections of the active layer, resulting in greater deviations in brightness (Figure 6-6b).

Figure 6-6 (a) V-L curve of fully solution-processed blue OLEC operated at the voltage-pulsed mode. The pulsed pixel has an area of 1 × 5 mm^2. The voltage pulse had a pulse-width of 100 ms and 1% duty cycle; (b) the luminance camera photograph of emitted pixel driven at a 50 V pulse.

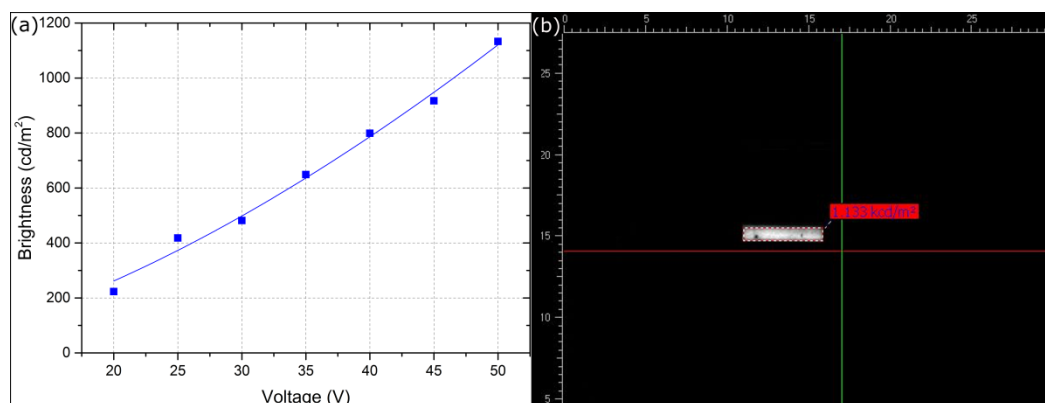## 6.3 Solution-processed blue OLEC on ITO for device performance investigation

As described in the previous section, the fully solution-processed OLEC has limited geometric profile reproducibility. It is mainly because the surface morphologies of the inkjet-printed bottom silver electrode deviated from sample to sample. For this reason, pre-patterned ITO glass substrates were chosen in order to investigate systematically the influence of active material compositions and active layer thicknesses on emission brightnesses at the pulsed mode.
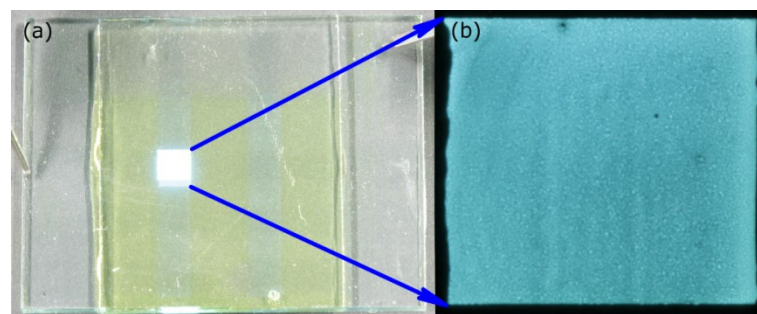
Figure 6-7 (a) Photograph of a blue OLEC on a ITO glass substrate with an illuminated pixel; (b) Photograph of an illuminated pixel (1.5×1.5 mm^2).

The device architecture of solution-processed blue OLEC is depicted in Figure 4-13. Compared to layer structure depicted in Figure 4-12, only the Ag bottom electrode was replaced by pre-patterned ITO electrode. Thanks to the high transparency of ITO (see Figure 6-2), fully transparent blue OLECs were fabricated. In order to increase emission brightness for on-chip sensing applications, an additional silver mirror can be inkjet printed on the top of the glass coverslip, as described in section 4.1.1. The similar manufacturing process parameters were used and detailed described in section 4.2.1.The photograph of fabricated blue OLEC sample with one illuminated pixel is depicted in Figure 6-7b. It can be seen that the illuminated pixel has higher emission uniformity than the blue OLEC sample with Ag electrode. The device did not have higher emission brightness at relatively low driving voltage (< 15 V). it could be due to the high work-function of oxygen-plasma activated ITO (up to -5.5 eV [203]), which hinders the electron injection speed. Similar to the blue OLEC sample with Ag electrode, a much higher brightness was achieved (see Figure 6-8a), when the blue OLEC on ITO sample was driven at pulsed mode with a much higher voltage (e.g. 45 V). A brightness of > 2000 cd/m^2 can be realized when the sample was pulsed at > 40 V. The first reason could be the more homogeneous surface of ITO elec-

trode and smaller pixel size, which led to more homogeneous active layer and higher current density (see Figure 6-7). The second reason could be the lack of metal electrode that quenches the excitons and then reduce the emission brightness. The electroluminescence spectra of the blue OLEC were measured at different driven voltage level to check if there is any energy shift due to high current density at high voltages. As shown in Figure 6-8b, there is almost no deviation of the spectra between continuous driving at 10 V and pulsed at 40 V. The slight difference on the long wavelength tail is because of high noise level when the device was driven at 10 V.
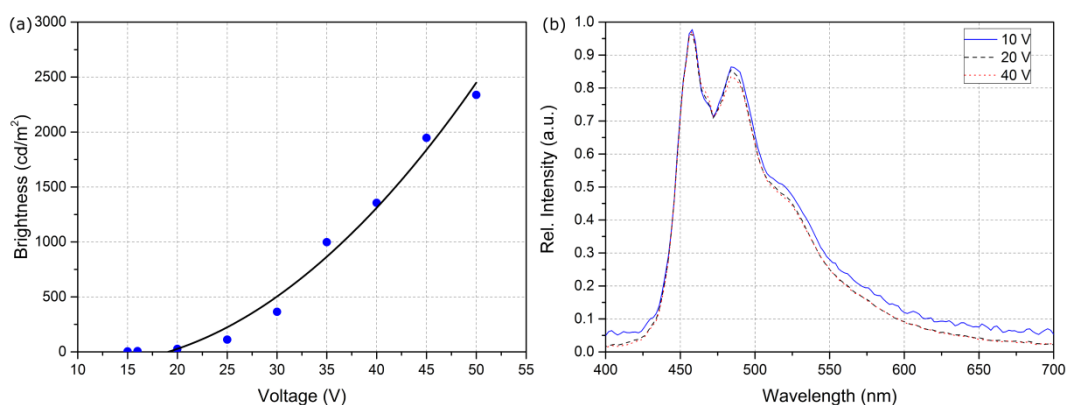
Figure 6-8 (a) V-L curve of a blue OLEC sample driven at voltage-pulsed mode; (b) electro-luminescence spectra of solution-processed blue OLECs on ITO. The spectra were taken when the sample was continuously driven at 10 V (blue line), pulsed at 20 V (black dash line), and pulsed at 40 V (red dot line).

For disposable lab-on-a-chip fluorescence sensing applications, brightness higher than 2000 cd/m^2 and a moderate lifetime are required [204]. The basic requirement of brightness can be fulfilled by driving at high voltage pulses, therefore the lifetime measurement was also tested at the driven condition to have an emission brightness of > 2000 cd/m^2. For comparison, another pixel was driven at DC mode with an initial brightness of 100 cd/m^2. The both results are plotted in Figure 6-9. Even though the device emitted constantly only a brightness of ~100 cd/m^2, the sample had relatively fast degradation at DC driving mode. It had 25, 33, and 90 min lifetime when the brightness reduced to 80%, 75%, and 50% of its initial brightness. This confirms the current short lifetime issue of OLECs. On the other hand, the sample was relatively stable after 1000 pulses at voltage-pulsed operation with emission brightness of > 2000 cd/m^2.
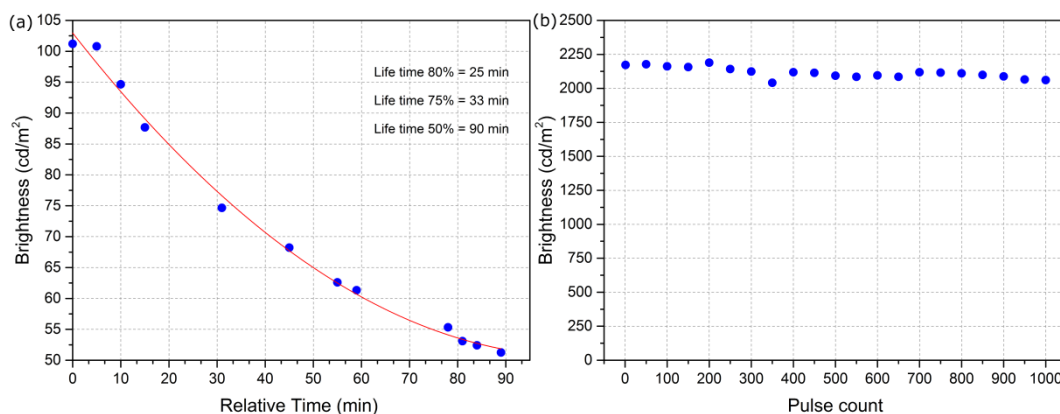
Figure 6-9 Plot of lifetime tests of solution-processed blue OLECs on ITO. They were driven at (a) DC mode to emit an initial brightness of 100 cd/m^2, and (b) voltage-pulsed driving mode to emit an initial brightness of 2200 cd/m^2 (pulse-width 100 ms, 3.3% duty cycle).

6.4 Material composition and layer thickness investigation

Although it has been demonstrated that the solution-processed transparent blue OLEC on ITO can achieve a brightness > 2000 cd/m^2 and a lifetime > 1000 pulses in the previous section, the device was fabricated with dopant concentration and layer thickness reported from the literatures [151,205]. However, the material and processing parameters were optimized for display or lighting applications, and they were not intended for voltage-pulsed driving operation. Consequently, in this section different material compositions (mass ratio) of LEP and dopants as well as active layer thicknesses were tested and ana-lyzed for the first time to understand the influence on emission brightness under voltage-pulsed driving mode.

In the previous section, the widely-used mass ratio of 1:1:0.2 was used for produc-ing the blue OLEC devices, and it gave relatively good performance. However, it has been reported that the high concentration of the electrolyte and dopants can reduce the emitted light intensity by the excitons quenching [183,206]. On the other hand, too low dopant concentration leads to long *in situ* doping time, which means slow turn-on and limits its applications [207]. It has also been intensively reported that higher light intensity can be realized by balanced the hole and electron injection and transporting [205]. One feasible and simple method is to modify the active layer thickness [208]. That is mainly due to the large leakage current in non-balanced devices, joule-heating induced degradation by non-radiative decay, and excitation quenching to the electrodes. Most research has been done to date was concentrated on improving performance on DC driving mode at relatively low

brightness (mostly 100 cd/m^2). Currently, no material and layer thickness investigation has been found on OLECs driven at voltage-pulsed mode.

For this investigation, a series of blue OLEC samples were solution-processed on pre-patterned ITO substrates following the procedure described in Chapter 0. The selected mass ratios of LEP, CE, and LiCF$_3$SO$_3$ were 1:1.25:0.27, 1:1:0.50:0.10, 1:0.10:0.02, respectively. The mass ratio of CE and LiCF$_3$SO$_3$ was always kept at 1:0.20 to ensure good ionic mobility of dopants [205]. The highest dopant concentration of 0.25 was chosen because it is widely used with rough surfaces and from literature reports [209]. The lowest dopant concentration of 0.02 was selected due to good performance from literature and theoretical model [205]. To understand the influence of the active layer thickness, the thicknesses of around 100, 150, and 300 nm were chosen. It has been confirmed in reserach that 10 to 20 nm thick emission layer is thick enough to make high efficient OLEDs [210]. However, the results are based on small molecule OLEDs, which has much small geometric dimensions, and they are mostly deposited by vacuum evaporation or vapor deposition to obtain thin and homogeneous layers. For polymer OLEDs, the typical active layer thickness is 80 to 100 nm [43]. Long polymer chains and non-fully-controlled chain lengths result in inhomogeneous layers at thinner layer thickness. Based on this reason, 100 nm was chosen for the lowest OLEC active layer thickness and 300 nm for the highest.

The V-L characterization of solution-processed blue OLECs with different dopant mass ratios and active layer thicknesses is depicted in Figure 6-10. Different lines and symbol colors represent different mass ratios of dopant to LEP: 0.27:1 (black), 0.10:1 (red), and 0.02:1 (blue). Different symbols of ■ , ● , ▲ represent the active layer thickness of 100, 150, and 300 nm, respectively. First, we look at the emission brightness of samples with different dopant mass ratios (curves with different colors in Figure 6-10). It can be seen that the emission brightness increased with decreasing dopant concentration at same driving voltage , in particular at high driving voltages. That means OLEC samples with lowest dopant ratio (0.02, blue color in Figure 6-10) emitted the highest light intensities, while samples with the highest dopant concentration (0.27, black color in Figure 6-10) emitted the lowest light intensities. As all devices were pre-doped with constant low driving voltage of 10 V right before the V-L measurement, the influence of different turn-on times due to dopant concentrations can be neglected. The exciton quenching effect due to the additional solid electrolyte and dopants can be one part of the reason for this trend. The higher the dopant concentrations are, the more excitons will be quenched, which results in

non-radiative relaxation. Besides exciton quenching, the lower dopant concentrations leads to PN junctions with slightly lower electron and hole mobility. That brings lower leakage current and more hole and electron combinations which results in higher emission light intensity. That is also the reason why low hole and electron mobile blocking layers are designed in modern OLEDs architecture, so that less holes and electrons are transduced to the counter electrodes and have time to combine to emit light [211–213].
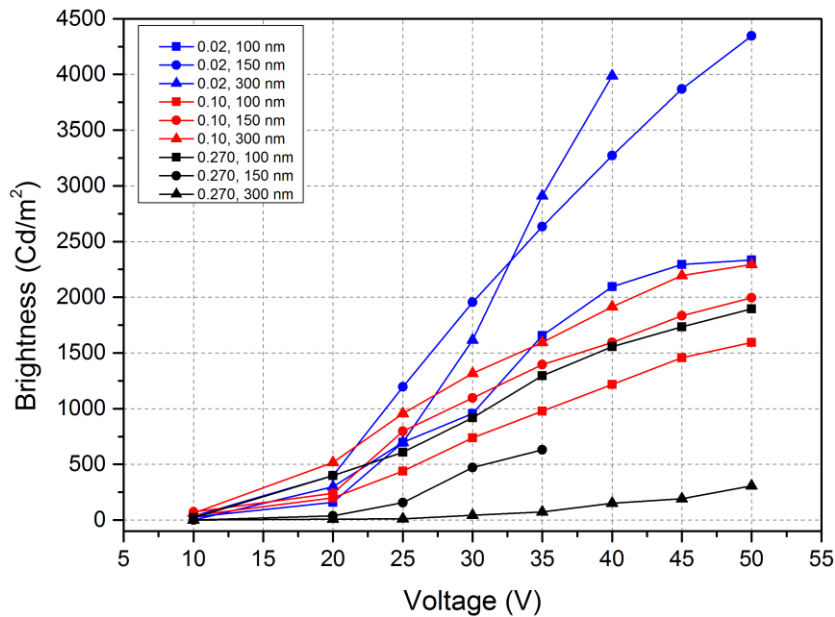
Figure 6-10 Voltage – brightness curve of various blue OLEC samples operated at pulsed driving mode. The different color represents the dopant mass ratio of 0.02 (blue) 0.10 (red), and 0.27 (black), compared to LEP. Within all the different dopant concentration, the samples with active thickness of 100 nm (■), 150 nm (●) and 300 nm (▲) are also characterized.

Then, we focus on analyzing the influence of active layer thickness on emission brightness (comparing the curves with different symbols in Figure 6-10). Compared to the dopant mass ratio, the influence of the thickness is much more complicated. First we observe the V-L curves with the lowest dopant mass ratio 0.02 (blue color in Figure 6-10), at high pulsed driving voltage (40 V), the thicker the active layer is, the higher the emission brightness will be. That could be explained that, during the short pulse duration of 20 ms, the sample with a thicker active layer probably results in a thicker intrinsic area during pre-doping. Therefore, it has less over-doping and thus exciton quenching, which results in higher light-emitting efficiency. For the dopant mass ratio 0.10 (red color curves in Figure 6-10), the curves clearly fit the trends that samples with higher light intensity results in thicker active layer. However, for much higher dopant concentration (dopant mass ratio

0.27), the opposite situation can be observed. The samples with higher active layer thickness emit lower light intensity. The reason would be that the fast doping due to high concentration leads to great extent of over-doping during short operation pulses regardless of the layer thickness. Therefore, the higher the dopant mass ratio is, the more exciton quenching will be.

To further understand the light emitting behaviors of solution-processed blue OLECs under voltage-pulsed driving operations, the measured brightness values from brightness detector were recorded over time when OLEC samples were driven at 40 V with different pulse duration. The variation of pulse duration here is mainly to prevent device from fast degradation at high operation voltages. The results are plotted in Figure 6-11. The samples with dopant ratios to LEP of 0.02 (blue color curves), 0.10 (red color curves), and 0.27 (black color curves) as well as active layer thickness of 100 (curves with ■), 150 (curves with ●), and 300 nm (curves with ▲) are compared.
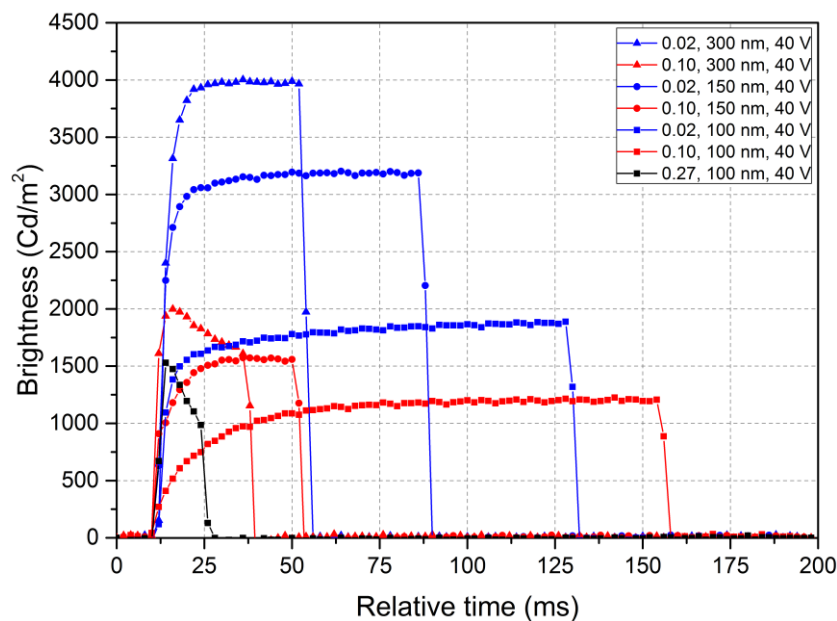
Figure 6-11 Brightness pulse waveform over time from various blue OLEC devices with 40 V pulsed driving voltage. The different color represents the dopant mass ratio of 0.02 (blue) 0.10 (red), and 0.27 (black), compared to the LEP. The solution-processed devices with active thickness of 100 nm (■), 150 nm (●) and 300 nm (▲) are also characterized.

As illustrated in Figure 6-11, for the OLEC samples with high dopant mass ratio 0.27 (black color curve), the emission brightness reduces over time. It clearly indicates that the efficiency of OLEC decreases dramatically with high voltage driving, even for short duration. It has to be emphasized here that the decreasing of efficiency (or brightness) over

time is not due to the material degradation. Because the same brightness pulse waveform can be observed with voltage-pulsed driving mode, that is 10 ms pulse-width and 0.5% duty cycle, as depicted in Figure 6-12. The slightly deviation of the brightness between the three pulses can be related to the measurement resolution of the pico-amperemeter. It has a maximum time resolution of 2 ms, and therefore the brightness values could be varied depends on at which specific time the pico-amperemeter taken the measurement. Consequently, the reduced brightness over time can be only explained to the quenching of the over-doping and leakage current. When the active layer getting thicker, the more active material turned darker, i.e. losing its fluorescent light ability. This reduces the overall emission light intensity.
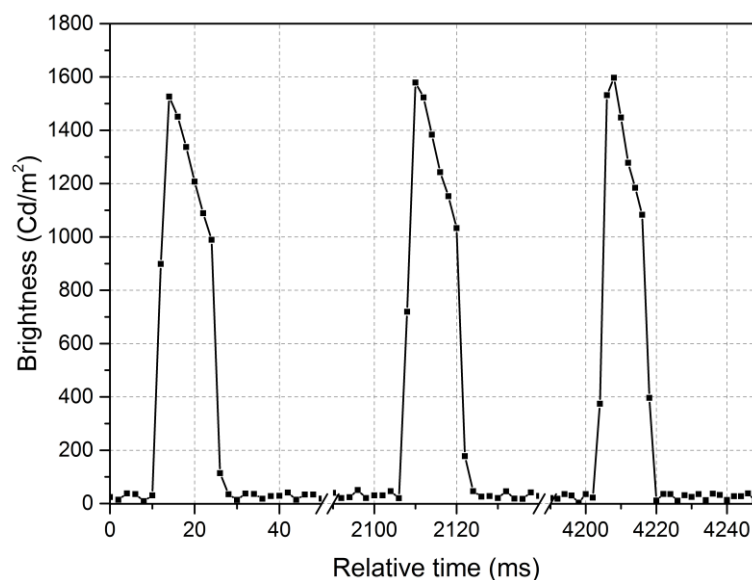
Figure 6-12 Three brightness pulse waveforms over time from solution-processed blue OLEC device with 40 V pulse driving voltage, 20 ms pulse duration and 3 s pulse interval.

For the OLEC samples with lowest dopant mass ratio 0.02, for all the active layer thickness, it has a relatively stable waveform, which has a gradually increasing brightness at the beginning of the pulse and then becomes stable over the rest of the pulse. The interesting part of the samples with lowest dopant mass ratio of 0.02 is that contrary brightness trends can be observed between low driving voltage (e.g. 20 V) and high driving voltage (e.g. 40 V). At low driving voltage of 20 V, the OLEC sample with the thinnest active layer emits highest light intensity, while the thickest emits highest at high driving voltage of 40 V. Low dopant concentrations leads to low electron and hole mobility and injection rate but with wider intrinsic part. Hence, the samples do not have sufficient electron-hole pairs

at low driving voltages to emit high brightnesses, in particular with thicker active layers. On the contrary, the injection rate of electrons and holes is highly increased under high voltage bias. Because of the relatively low carrier mobility at thicker active layer, electron and holes have more opportunity to combine and emit photons. Thus, the sample with a low dopant concentration and a thicker active layer has a higher emission brightness at a high driving voltage.

For the OLEC samples with dopant mass ratio of 0.10, a clear transition behavior between low and high dopant concentrations can be observed. In principle, it follows the same trends on the influence of active layer thickness as the OLEC samples with dopant mass ratio of 0.02: A thicker active layer leads to a higher emission brightness at a high pulsed voltage. However, the OLEC sample with active layer thickness of 300 nm shows the similar brightness pulse waveform as the OLEC samples with dopant mass ratio of 0.27. This indicates that the light emission efficiency reduce when the total dopant reach certain level. At this level, the over-doping takes part in and quenching the combined excitons.

6.5 ZnO interlayer investigation for blue OLECs

Theoretically, because of the *in situ* doping, work-function adaptation will not place a role here. Therefore, simply manufacturing OLEC between two PEDOT:PSS layer should work, and electrons and holes can direct inject into active layer without barriers (so-called Ohmic contact). However, in practice, the doping is not high enough to achieve Ohmic contact, in particular for high work-function mismatch. It has also been found out that certain work function adaptation is still necessary to realize good performance [214]. That is also the reason why most reported PLECs are between two different electrodes such as ITO, PEDOT:PSS, carbon black, evaporated Al/Ag [215]. As PEDOT:PSS has relatively high work function (around 5.2 eV), it serves a good anode but a bad cathode. In order to realize a relatively low work-function cathode by solution processing, A ZnO interlayer is introduced here between active layer and the ITO electrode in order to investigate the influence of additional ZnO interlayer. ZnO layer has a work function around 4.1 eV, which is much lower than PEDOT:PSS (-5.2 eV) and ITO (-4.7 eV). Theoretically, it leads to a better electron injection rate. As most LEPs are hole-transporting materials, samples with additional ZnO interlayer should have better balance of hole and electron combinations.
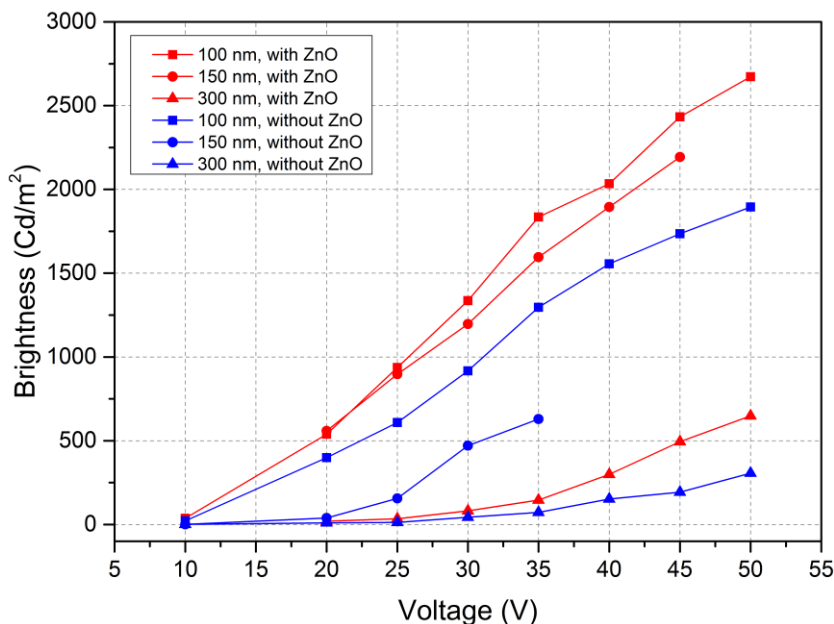
Figure 6-13 V-L curve of blue OLEC samples driven at voltage-pulsed mode. Device layer structures are ITO ‖ ZnO ‖ OLEC layer ‖ PEDOT:PSS or ITO ‖ OLEC layer ‖ PEDOT:PSS. Various active layer thicknesses of 100 nm, 150 nm, and 300 nm were tested for both structures.

The Figure 6-13 illustrates the V-L characterization of solution-processed blue OLECs with and without ZnO interlayer. In this investigation, a mass ratio of 1:1:0.27 between LEP, CE and $LiCF_3SO_3$ was used. Devices with active layer thicknesses of 100, 150, and 300 nm were also compared. It can be clearly seen that devices with ZnO interlayer emits higher brightness at the same pulsed driving voltages. This trend keeps the same for all the tested voltages. It confirms the theory that lower work-function barriers due to ZnO leads to higher injection of electrons from cathode side as well as faster N-doping. Consequently, a more balanced P-N junction can be *in situ* generated, which brings higher device efficiency, i.e. higher emitted light intensity in this case. Furthermore, the ZnO interlayer has the same improvements on all three active layer thicknesses. It indicates that the results are not dependent on active layer thickness.

The OLEC sample with ZnO interlayer and 100 nm active layer thickness was used to test the operation lifetime under pulsed mode. The measurement results are plotted in Figure 6-14. It was pulsed driven with a pulse-width of 20 ms, 0.67% duty cycle and had an initial brightness of 2800 cd/m^2. The plot shows that the sample had no degradation after continuous 10 000 pulses and only decreased to 90% of its initial emission brightness after 25 000 pulses. It is sufficient stable as the excitation light source for lab-on-a-chip fluorescence sensing systems.
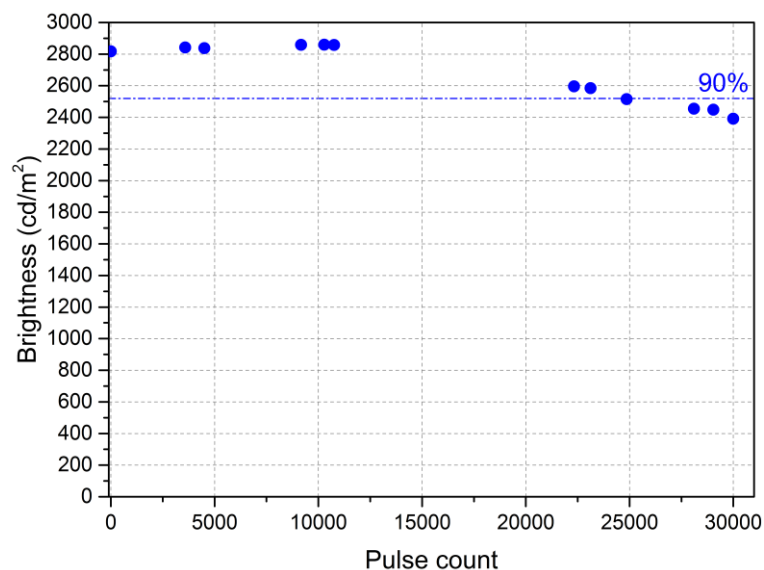
Figure 6-14 Lifetime characterization of solution-processed blue OLEC on ITO. Device has a layer structure of ITO ‖ ZnO ‖ OLEC layer (mass ratio of 1:1:0.27, 100 nm) ‖ PEDOT:PSS. OLEC was operated at high pulsed-voltages to emit an initial brightness of 2800 cd/m^2 with a pulse-width of 20 ms and 0.67% duty cycle.

In summary, this chapter described a novel approach to use fully solution-processed blue OLEC as an excitation light source for disposable lab-on-a-chip systems. It was first demonstrated that an ITO-free, fully solution-processed blue OLEC can be produced via combination of inkjet printing and spin coating. Moreover, a brightness of > 1000 cd/m^2 can be emitted at voltage-pulsed driving mode. By replacing the printed silver electrode with a pre-patterned ITO electrode, the active material composition along with active layer thickness of OLECs was investigated to improve the maximum emission brightness. It has been demonstrated that the OLECs with lowest dopant concentration and relative high active layer thickness can emit highest brightness (~4000 cd/m^2 at 40 V) among the test samples. Furthermore, it has been shown that the light brightness can also be improved by insert a ZnO interlayer, which reduces the electron injection barrier and then improve the efficiency. A lifetime test under voltage pulsing operation shows that the blue OLEC samples can maintain 90% its initial brightness after 25 000 pulses. All these demonstrate that blue OLECs with pulse driving mode could be sufficient stable and bright as an excitation light source for disposable lab-on-a-chip fluorescence sensing systems.

7   Demonstrator and applications

In this chapter, three different demonstrator cases are presents. First, OLEC can be fabricated on top of the PEDOT:PSS electrode plus ZnO interlayer combination instead of ITO electrode on an ultrathin glass. Therefore, ITO-free, fully solution-processed OLEC can direct integrate on microfluidic chips for sensing applications. In this case, the SuperYellow LEP was used instead of Merck Blue LEP to demonstrate that the OLEC working principle can be easily transferred to another LEP with a different emitting color. Next, tandem OLEC and OLEC combination was demonstrated in the second section. Tandem device structures are another strategy to increase the overall light emitting brightness via adding two or more samples on top of each other and driven at same voltage or current. Last, a demonstrator with integrated fully solution-processed blue OLEC and OPD on a glass chip was presented. This combination is first reported in the literature. A model fluorescent dye FAM was used to show the high optical sensitivity of this integrated organic sensor.

7.1   ITO-free, fully solution-processed OLECs

In order to achieve fully integration organic light sources directly on microfluidic chips, ITO electrodes need to be replaced because it is non-solution-processable and high cost. The most straightforward method is simply to replace ITO layer by a PEDOT:PSS layer, however it does not work well. It has also been found out that certain work function adaptation is still necessary to realize good performance [214]. Therefore, a solution-processable buffer layer is necessary. As demonstrated in previous section 4.1.2, ZnO layer can be solution-processed via $Zn(acac)_2$ precursor or nanoparticle dispersions. Moreover, electron injection can be reduced, which results in working devices. Consequently, in principle, ITO electrodes can be replaced by an inkjet-printed PEDOT:PSS layer and a solution-processed ZnO layer. On the contrary, to chapter 5, ZnO layer was spin-coated from a $Zn(acac)_2$ solution on top of inkjet-printed PEDOT:PSS layer in this section, but both methods work. In order to demonstrate the easy transfer of emitters in OLECs, yellow LEP SuperYellow was test in this ITO-free layer stack.

Thin glass was chose as the substrates by its good encapsulation capability (low water and oxygen transmittance rate) and better flexibility compared to normal glass. Especially, Schott AG has demonstrated that their chemically toughened ultrathin glass

(70 μm) can be bent with a radius of ~5 mm, which enables a huge potential in flexible electronics [216]. The 70 μm thin glasses using in this work were not chemically toughened. Therefore, produced OLEC samples had limited bending capability but demonstrated the proof-of-concept.

The manufacturing process is similar to the solution-processed blue OLEC on ITO substrates, which is describe in section 4.2.1. Here, the bottom electrode was replaced by a PEDOT:PSS plus ZnO bi-layer. The ZnO layer was spin-coated from 20 mg/mL $Zn(acac)_2$ in ethanol with a spin-rate of 1600 RPM for 45 s. It was then thermal annealed at 120 °C for 45 s on a hot-plate. The rest was the same except the LEP was SuperYellow in order to demonstrate the same OLEC principle can be transferred to another LEP. Another commonly used electrolyte PEO was used in this device instead of DCH18C6.
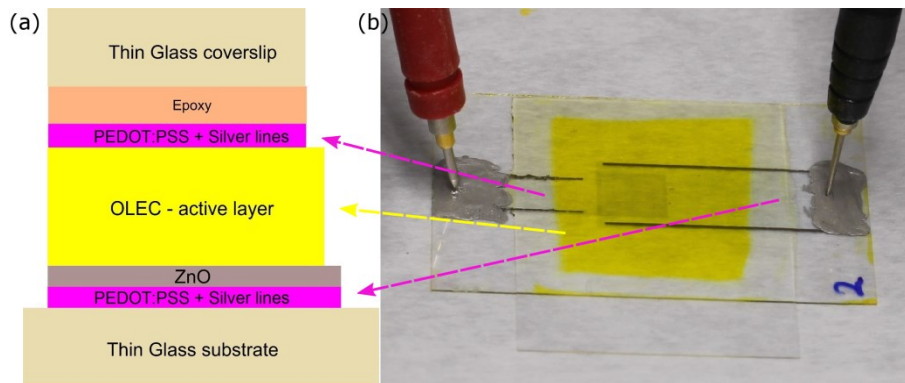
Figure 7-1 (a) Layer architecture diagram of a ITO-free, fully solution-processed yellow OLEC on thin glass; (b) photograph of a fully solution process yellow OLEC with a 5 × 5 mm² pixel size on a thin glass substrate.

Figure 7-1a illustrates the layer structure of this ITO-free, fully solution-processed yellow OLEC device. Figure 7-1b shows the fabricated samples. It can be seen that the PEDOT:PSS layers are quite transparent and only shows slightly greyish at the area where two PEDOT:PSS are overlapped. After electrical connecting, the yellow OLEC illuminated the yellow light when voltage was higher than 7 V. The photo of the illuminated pixel at 15 V can be seen from Figure 7-2a. The maximum brightness was 150 cd/m^2 at 20 V and the current efficiency was 1.32 cd/A at 15 V (brightness ~108 cd/m^2). The current-voltage characterization (Figure 7-2b) indicates the diode behavior of the doped OLEC. However, compared to the typical diode behavior, the OLEC gave much higher current at the reverse bias. That is because of the intrinsic *in situ* doping mechanism of the OLEC, which can be doped at the forward and reverse bias. The OLEC can work at both bias but with much lower performance at reverse bias. It can be seen that although the driving voltage was

relatively high, the current density was quite low compared to a normal OLED. The reason could be the relatively low conductivity of PEDOT:PSS compare to metal such as silver and aluminum. That could also explain why the sample worked stable at 15 V, which no degradation in brightness has been observed after 10 min continuous driving.
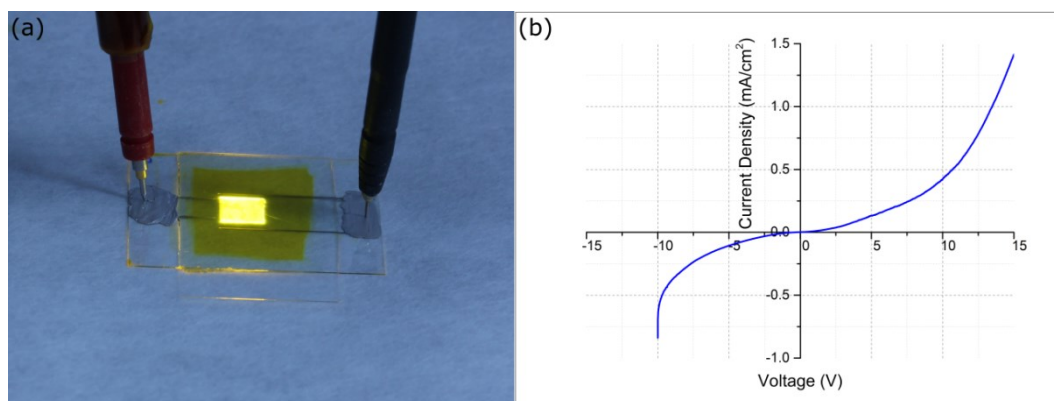
Figure 7-2, (a) photograph of a fully solution process yellow OLEC with an illuminated 5 × 5 mm² pixel on a thin glass substrate, driven at 15 V; (b) I-V curve characterization of the yellow OLEC.

There is an tendency to produce relative thicker active layer in flexible and fully solution-processed light-emitting devices [215], in the μm range instead of less than 100 nm of typical OLEDs. It is mainly because of the high roughness of the substrates, high roughness of solution-processed bottom electrode as well as the bending of the flexible substrates, which all vulnerable to the short-cut between top and bottom electrodes. Typically, the thinner the active layer is, the lower the driving voltage is required. That is one reason for high driving voltage of demonstrated flexible yellow OLEC here. Another reason is high resistance of PEDOT:PSS electrodes used here. Although PEDOT:PSS shows good combination of transparency, printability and conductivity, the volume conductivity is still much lower than widely used transparent electrode ITO (5000 S/cm) and metals such as Al (350 000 S/cm) and Ag (630 000 S/cm). Producing silver bottom electrode by inkjet printing silver nanoparticle dispersion meets the challenge of high inhomogeneity, while printing on top of active layer has the wetting problem and diffusion of the nanoparticles. Nevertheless, metal induced exciton quenching is another low efficiency issue. Inkjet-printed silver grid and multi-layer printed PEDOT:PSS combination [101] could be a good solution of reducing resistance and then driving voltage. On the other hand, for the simply three layer structure, normally the thick active layer thickness brings higher maximum brightness (luminance). It is simply because more electrons and holes will combine to exciton and convert to light instead of diffuse to the counter electrode. Combination of higher

dopant concentration and thicker active layer shows tendency of lower driving voltage and maintain or increase the brightness.

7.2 Solution-processed tandem OLEDs and OLECs on ITO
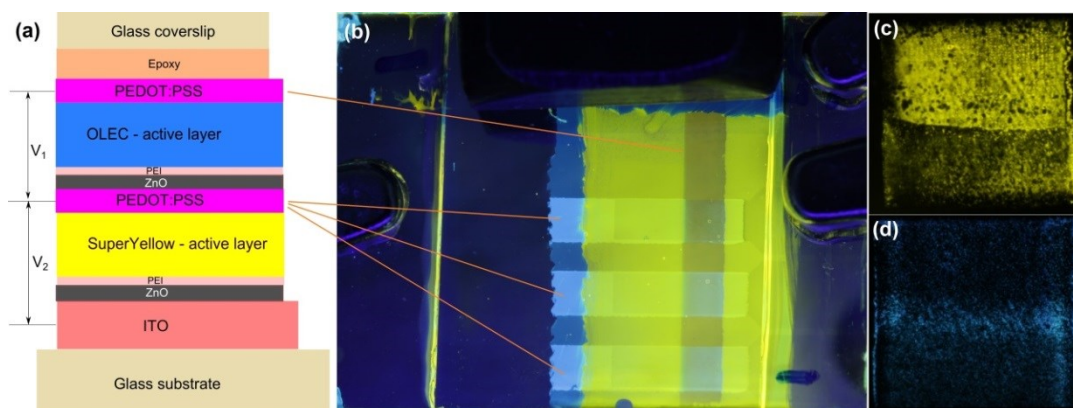
Figure 7-3 (a) layer structure scheme of a fully solution-processed tandem SuperYellow OLED and blue OLEC sample; (b) photoluminescent imaging of the fabricated sample. The orange lines indicate the location of inkjet-printed PEDOT:PSS layers. The top PEDOT:PSS layer is shared by all three light-emitting pixels while each pixel has their own PEDOT:PSS electrode between SuperYellow and blue active layer; (c) electroluminescent imaging of the SuperYellow OLED in fully solution-processed tandem device driven at 6 V (V_2); (d) electroluminescent imaging of the blue OLEC in fully solution-processed tandem device driven at 12 V (V_1).

As ITO electrodes are rarely solution-processed and normally relatively expensive, an alternative bottom electrode is required to reduce the manufacturing costs. Although the OLEC is not sensitive to a work function difference and theoretically both electrodes can be PEDOT:PSS, a slight work function adaptation is still recommended for better performance [214]. Hereby, I demonstrate spin-coated ZnO and ultrathin PEI layer on top of PEDOT:PSS electrode to achieve a working device. An ultrathin PEI layer on top of electrodes such as Ag, ITO, ZnO and PEDOT:PSS can dramatically reduce the surface work function and improve the electron injection [214]. A tandem SuperYellow OLED and blue OLEC was fabricated on the same ITO substrate. All layers are spin-coated except PEDOT:PSS electrodes are inkjet-printed, and the manufacturing process is described in the experimental section 4.2.5. Figure 7-3c and d illustrate that both solution-processed SuperYellow OLED and blue OLEC are working. As the blue OLEC is only driven between PEDOT:PSS electrodes (i.e. V_1 in Figure 7-3a), it is proven that the PEDOT:PSS plus ZnO and PEI layers can replace ITO electrodes to achieve ITO-free, fully solution-

processed blue OLEC samples. Furthermore, the tandem device is demonstrated here not only to show that the PEDOT:PSS, ZnO and PEI combination can replace the ITO electrode but also that the tandem structure is another method to improve the light brightness for on-chip fluorescence detection. At the moment, the manufacturing parameters are not fully optimized. That is the reason why both yellow OLED and blue OLEC do not have homogeneous light emitting and high brightness.

7.3 Integrate blue OLECs for on-chip sensing

In this section, the first integrated fluorescence sensing system based on a fully solution-processed OLEC with a solution-processed OPD on a glass chip was introduced. Selecting polarization filters makes the LoC utilizable for a variety of applications. Blue excitation light and Fluorescein amidite (FAM) fluorescent dye were selected for demonstration as they are widely used in fluorescence bio-/chemical sensing. The demonstrated integrated fluorescence sensor is able to measure a low concentration of fluorescent dye, i.e. FAM in water in this case, as low as 1 μM. Furthermore, thanks to the fully solution-processing and vacuum free manufacturing and easy tuning of the excitation light color, fluorescence sensors based on OLEC, OPD, and linear polarization filters enable a bright future for low-cost, disposable, multi-usage point-of-care applications.

7.3.1 Chip-integration and characterization
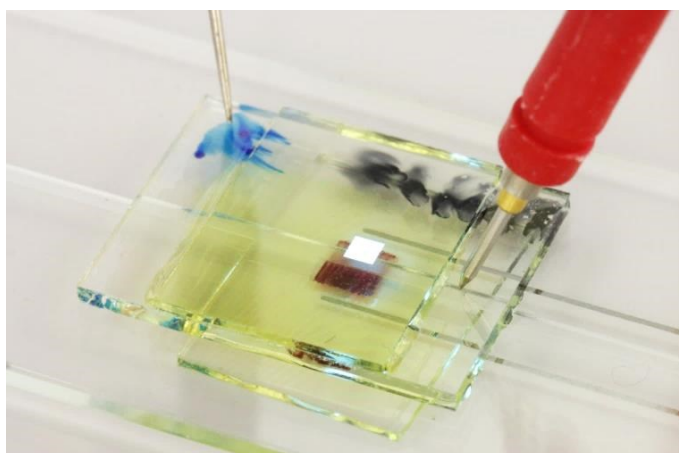
Figure 7-4 OLEC excitation and OPD detection system with a glass microfluidic device. For illustration reasons, the linear polarization filters are not integrated. The blue illuminating square is the illuminating blue OLEC pixel; the dark reds square is the active layer of OPD; the glass channel is in-between the OLEC and the OPD.
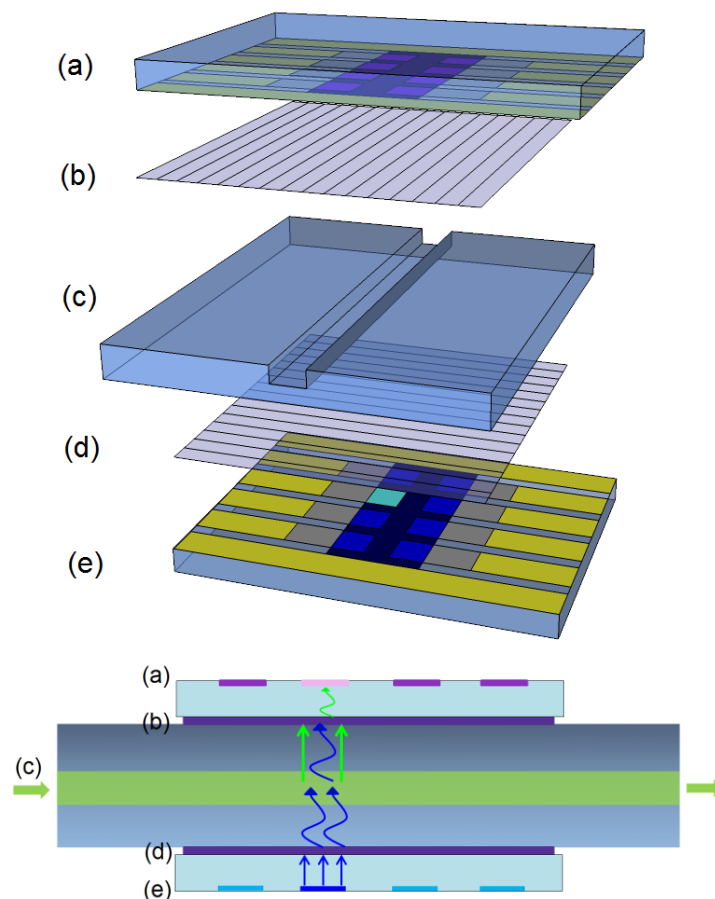
Figure 7-5 (top) Schematic exploded view and (bottom) 2D edge view of OLEC excitation and OPD detection system with a glass microfluidic device and polarization filters: (a) fully solution-processed OPD; (b) first linear polarization filter oriented at 0 degree; (c) glass microfluidic chip; (d)) second linear polarization filter oriented at 90 degree; (e) fully solution-processed blue OLEC.

Figure 7-4 shows a photograph and Figure 7-5a scheme of the integrated fluorescence detection system. The test chip was made of sodium borosilicate glass, and a 1 mm wide and 1 mm deep channel was cut by wafer dicing. The channel was sealed by a glass cover with UV curable optical adhesive (Norland Optical Adhesive 65, Norland Products, Inc.). The same glue was used to attach the two polarization filters (Thorlabs, Inc.) at orthogonal orientations onto the top and bottom side of the channel. Fully solution-processed blue OLEC was manufactured as described in section 0. The used blue OLEC ink had a concentration of 10 mg/mL in cyclopentanone and a mass ratio of 1:1:0.27 (LEP:DCH18C6:LiCF$_3$O$_3$). The active layer had a layer thickness of ~100 nm and ZnO interlayer a thickness of ~20 nm. The used OPD here had a layer stack of ITO ‖ ZnO (20 nm) ‖ P3HT:PCBM (200 nm) ‖ PEDOT:PSS (40 nm). Then the fully solution-

processed blue OLEC and OPD were glued on top of each filter, and the 1 mm^2 light-emitting pixel was aligned with the channel as well as the 1 mm^2 OPD pixel. Different concentrations of the fluorescent dye FAM were dissolved into distilled water and injected into the channel for fluorescence sensing testing. The OLEC driving method and the OPD measuring method are described in section 4.3.

7.3.2 Characterizations of OLEC and OPD

Organic light-emitting electrochemical cells
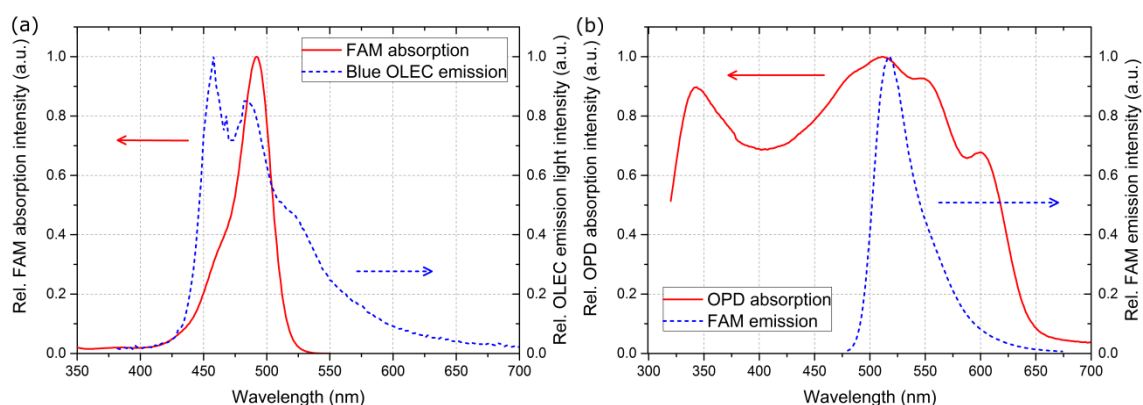
Figure 7-6 (a) Emission spectrum of fully solution-processed blue OLEC and the absorption spectrum of FAM; (b) Absorption spectrum of fully solution-processed blue organic photodiode and the emission spectrum of FAM.

One advantage of using OLEDs and OLECs as a fluorescence sensing excitation light source is that the emission peak wavelength can be tuned relatively easily by selecting different light emitting polymers or small molecules. However, the layer structure of OLEDs has to be slightly modified, e.g. a different electron transporting layer, when emitting a different light color via different emitters due to different energy band gaps. OLECs have the advantage of keeping exactly the same layer structure for different emitted colors due to the *in situ* doping mechanism. This provides great benefits in integrating several fluorescence sensing applications into one microfluidic chip via exactly the same, simple, and low-cost manufacturing methods. In this paper, a blue emitter emitting in the range of 450 to 485 nm was chosen for demonstration due to its wide applications in chemical or biological fluorescence sensing. Figure 7-6a illustrates the normalized emitted light spectrum of the fully solution-processed blue OLEC and the absorption spectrum of the fluorescent dye FAM. It can be clearly seen that the absorption wavelength range of FAM fluo-

rescent dye is well overlapped with blue OLEC emission light, and therefore this blue OLEC is a suitable light source for FAM fluorescent excitation.

Organic photodiodes

An OPD was used to detect fluorescent light intensity. Figure 7-6b shows the absorption spectrum of the active material used within the OPD. The P3TH:PCBM blend absorbs in a broad spectral range from 350 to 650 nm, due to the PCBM absorption from 350 to 450 nm and the P3HT absorption from 450 to 650 nm. However, the charge carriers contributing to the detectable photo current are only generated within the P3HT, limiting the detectable spectral range. The emission spectra of the selected fluorescent dye FAM is entirely covered by the absorption spectra of the OPD. At the maximum FAM emission peak at 518 nm the OPD shows a sensitivity of 0.11 A/W while the dark current density at 0 V was lower than 10 pA/mm².

The wide spectral detection range of the OPD makes it compatible with many different fluorescent dyes. However, the combination with the wide emission range of the OLEC causes wide spectral overlap of OLEC and OPD (see Figure 7-6b). In addition, the fluorescent light intensity is orders of magnitude lower than the emitted light of the OLEC and not all of the OLEC light is absorbed by the FAM [217]. Therefore, polarization filters are included into the chip. These filters can transmit polarized light within the full visible light spectrum. They are included on each side of the channel and with 90° rotation. Thus, no light of the OLEC should pass through the second filter.

7.3.3 Characterization of the fluorescence sensor

The extinction property of the linear polarization filters was first characterized with a sky blue inorganic LED and a silicon photodiode. With a single linear polarization filter, only 41.3 % light intensity can be transmitted. Since the excitation light has to pass the first filter and the fluorescent light has to pass the second filter and assuming 50 % of the fluorescent light emitted from the fam is emitted toward the detector, only ~8 % of the emitted fluorescent light will reach the detector. When the two linear polarization filters were aligned orthogonally to each other, merely 0.012 % of the light can be transmitted. This corresponds to a nominal extinction ratio of 38.5 db.

The photocurrent response of the fully solution-processed OPD for various FAM concentrations in water from 1 to 200 μm was measured in the integrated chip with filters

as well as the fully solution-processed blue OLEC. The blue OLEC was pulsed at 20 and 40 V to emit a light brightness of 500 and 2000 cd/m^2, respectively.
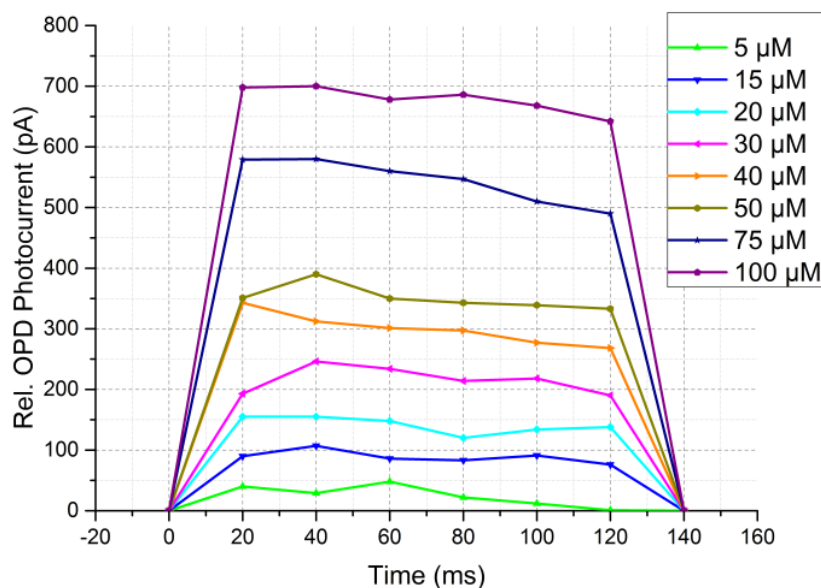
Figure 7-7 FAM fluorescence responses measured with the OPD at different FAM concentrations.

Figure 7-7 shows the fluorescence signals at different FAM concentrations as a function over pulse duration, which was excited by OLEC with 140 ms 20 V voltage pulse and detected by the OPD. The current values of the OPD were measured every 20 ms, which corresponds to six different measurement values for each light pulse. The background noise, which was measured using pure distilled water instead of FAM solution, was subtracted from the measurement values. It consists of the dark current of the OPD and the passing light from the blue OLEC through two orthogonally-oriented polarization filters. The measured background photocurrents for measurement with 500 cd/m^2 and 2000 cd/m^2 excitation light intensity was as low as 57 pA and 348 pA, respectively.

For all curves in Figure 7-7, a gradual decrease in the measured current can be observed over time. This is related to the excitation light intensity of the OLEC used. OLECs tend to have a higher light intensity when turned on, while decreasing to a saturated value after few seconds. Therefore, for pulsed operation of the OLEC is preferred rather than continuous driving for measurements. To evaluate the dependency of the fluorescence response on the FAM concentration the 6 data points per light pulse were averaged. The results can be seen in Figure 7-8a and b, respectively.
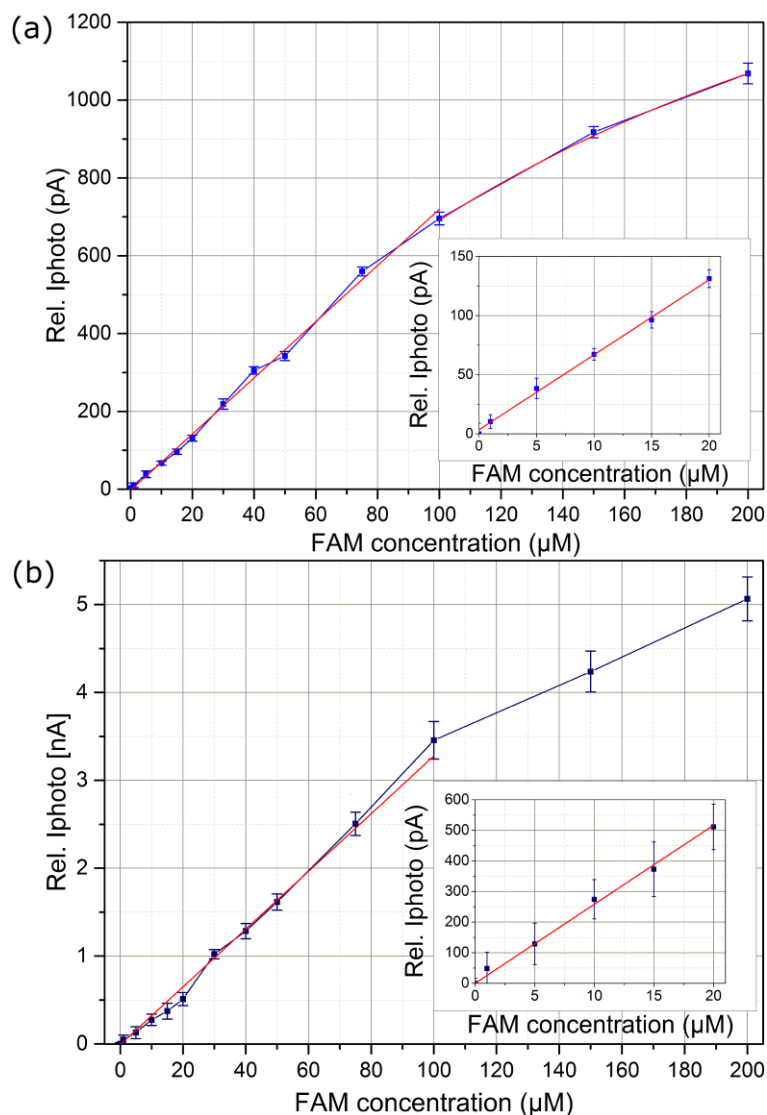
Figure 7-8 Fluorescent detection measurement by integrated OLEC and OPD with different FAM concentrations in water. The FAM solutions were excited by the blue OLEC with brightnesses of (a) 500 cd/m² and (b) 2000 cd/m²; The Inset graphs are the zoom-in of the low concentration parts (1 to 20 µM).

It can be observed that concentrations as low as 1 µM can be measured even with a relatively low brightness of 500 cd/m² of the blue OLEC device, which corresponds to an OLEC electrical driving power as low as 5.8 mW. For low concentrations up to 20 µM, a strong linear dependency (R=0.9999) is visible. This linear dependency could be extended to 100 µM. For concentrations of more than 100 µM, both graphs for 500 cd/m² and 2000 cd/m² start to become non-linear with a decrease in the graphs slope. This non-linearity is an intrinsic behavior of the intensity dependency of the fluorescence response itself.

The signal to noise (S/N) ratio was calculated and is presented in Figure 7-9. When the measured photocurrent is close to the background noise, the measurement setup reaches its theoretical absolute limit of detection (LoD), i.e. S/N ratio equals 1. An S/N ratio of 1.1 (illustrated in Figure 7-9, the blue dash line) is a more practical measurement LoD, which in our case is about 500 nM. Based on this criteria, our results are even slightly better than the literature reports with more efficient evaporated OLED and OPD combinations [18,137]. This demonstrates that solution-processed OLECs and OPDs can be a suitable combination for the direct integration of a microfluidic fluorescent detection setup. Moreover, it brings the advantages of low-cost, flexibility and direct on-chip integration.
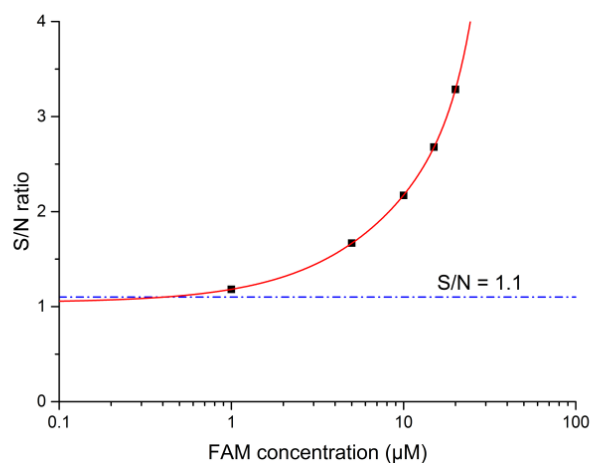
Figure 7-9 S/N ratio as a function of concentration of FAM dye as OLEC driven at 20 V pulses. Solid red line predicted trends for the theoretical LOD at S/N = 1.1, which is shown with a dashed blue line.

7.4 Conclusions and workflow guideline

All together three demonstrators have been shown. First demonstrator proves that the OLEC can easily work with another LEP and ITO can be replaced by a bi-layer of solution-processed PEDOT:PSS and ZnO. Second demonstrator gives a proof-of-the concept of tandem architecture to either improve maximum emission brightness or cover a broader excitation spectrum at one spot. The last demonstrator gives a first demonstration of microfluidic fluorescence sensing system including a fully solution-processed OLEC, a fully solution-processed OPD and two polarization filters. For the first time, the blue OLEC is introduced and demonstrated as a low-cost excitation light source. At 500 and 2000 cd/m² OLEC brightness, minimum concentrations of 1 µM FAM in water with an S/N-ratio > 1.1 could be detected. These results show that this fluorescence sensor featuring a combination

of a fully solution-processed OLEC and OPD, with linear polarization filters provides a viable solution for portable, disposable or multi-usage point-of-care applications.
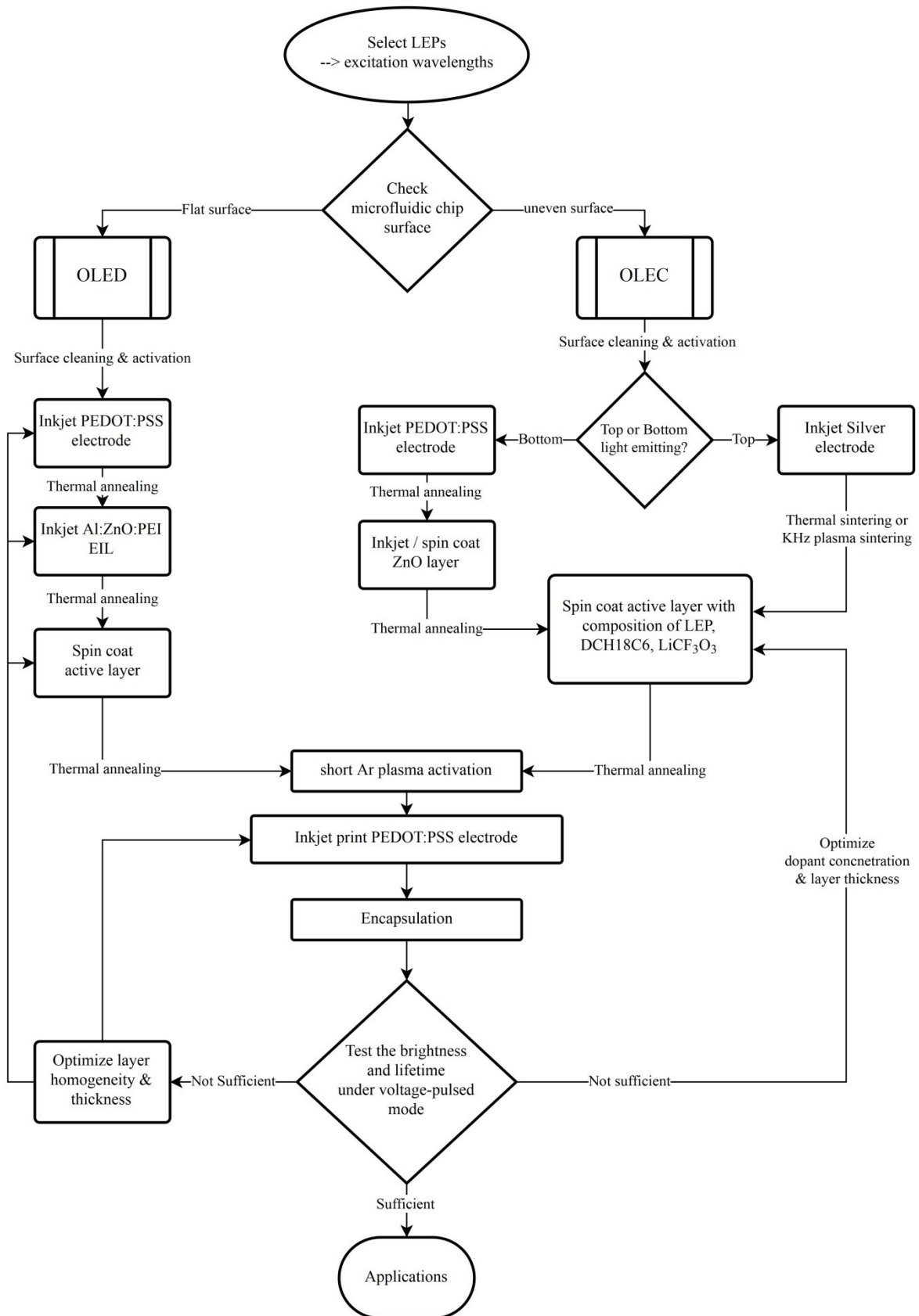
8 Conclusions and outlook

In this dissertation, a general guideline of integrating organic light sources (OLED and OLEC) as cost-efficient excitation light sources for fluorescence sensors on disposable microfluidic LoC systems has been developed. Two light emitters (blue and yellow) are selected to demonstrate the functionalities as well as to cover a wide part of the excitation light spectrum. First, bright yellow OLEDs were fully solution-processed with a simple 4-layer structure using a novel electron injection layer (EIL). The novel EIL was inkjet printed from a mixed ink of Al-doped ZnO nanoparticle dispersion and PEI. Al:ZnO provides work-function reduction as well as good electrical conductivity. The PEI serves as a universal work-function adaptation layer. With both materials, the inkjet-printed EIL eliminated the need of ultrathin PEI layer for work-function adaptation, and it enabled a one-step solution for electron injection instead of step-wise work-function adaptation via two different layers. Consequently, a fully solution-processed yellow OLED could be manufactured by inkjet printing and spin-coating. Because of high requirement on surface smoothness, pre-patterned ITO glass substrates were first used for performance investigation. The OLED had a layer structure of a pre-patterned ITO cathode, an inkjet-printed Al:ZnO:PEI EIL, a spin-coated SuperYellow active layer, and an inkjet-printed PEDOT:PSS anode. A brightness as high as 50 000 cd/m^2 has been measured under 40 V pulses. Even at a brightness of 10 000 cd/m^2, 85% of initial brightness can be still emitted after 3000 pulses, which is sufficiently stable for disposable on-chip sensing applications. The first time a lifetime characterization for solution-processed OLEDs at a high emission brightness of > 10 000 cd/m² has been achieved. This high brightness brings advantages of lower driving voltage and high fluorescent sensitivity. In the end, an ITO-free, fully solution-processed yellow OLED was also demonstrated by replacing the ITO anode with an inkjet-printable AgNW-embedded PEDOT:PSS electrode. Although the inkjet-printed bottom electrode had higher surface roughness and dark current, a brightness of > 16 000 cd/m² can be still achieved under 40 V pulses. **This is the first fully solution-processed, bright OLEDs produced using exclusively inkjet printing as a vacuum-free, mask-free, low processing temperature patterning method.** In contrast to the recently reported fully spin-coated OLEDs, the devices presented here showed higher maximum brightnesses. At the same driving voltages, the devices demonstrated here have lower brightness and efficiency. However, it is mainly due to the rougher surfaces of inkjet printed layers and simpler de-

vice structures without ultrathin layers. The device performance can be still improved by optical and electrical optimizations.

On the other hand, a fully solution-processable OLEC was introduced as a universal excitation light source on microfluidic LoC systems, in particular on microfluidic chips with 3D and/or uneven surfaces. Because of the *in situ* electrochemical doping, OLECs are relatively insensitive to carrier injection barriers due to the work function mismatch and to active layer thickness [35]. Consequently, typical blue OLEDs with 5 to 7 layers can be directly simplified into a sandwiched 3-layer OLEC structure. This dramatically reduces manufacturing steps and complexity in dealing with multi-layers, therefore it is a suitable organic light source for cost-efficient manufacturing and integration on polymeric chips with relatively rough surfaces and 3D structures. This advantage was proven by a fully solution-processed blue OLEC with an inkjet-printed silver cathode and transparent PEDOT:PSS anode, which emitted a maximum brightness of > 1000 cd/m^2 under the voltage-pulsed mode. However, OLECs exhibit intrinsic low maximum emission brightness and shorter lifetime due to the electrochemical doping. Consequently, this work has provided the first material investigation of OLEC on improving the maximum emission brightness under high voltage-pulsed driving mode. ITO electrode was chosen for better device reproducibility so that the device performance could be systematically compared. Two key material parameters-the dopant concentrations and active layer thicknesses-were varied and compared. It has been found that higher brightnesses can be achieved using lower a dopant concentration (mass ratio), and a thicker active layer normally leads to a higher emission brightness, in particular at high voltages such as 40 V. With a dopant mass ratio of 0.02 and an active layer thickness of 300 nm, the solution-processed transparent blue OLEC can emit a brightness of > 4000 cd/m^2. For the operational lifetime test, no degradation was observed after 1000 pulses under a 2000 cd/m^2 brightness level. Moreover, with an additional ZnO interlayer, higher brightnesses can be achieved and the device retains 90% of its initial brightnesses after $> 25\,000$ pulses at 2800 cd/m^2. Thus, both the emission brightness and operational lifetime should meet the requirement for an excitation light source on disposable microfluidic LoC systems. It can be concluded that low doping concentrations and thick active layers are beneficial when using OLEC for on-chip fluorescence sensing applications. When applicable, an additional ZnO interlayer can improve further emission brightness and device stability. **For the first time, the dopant concentra-**

tion and active layer thickness of OLEC were investigated for its potential in improving emission brightness and operational lifetime under the voltage-pulsed mode.

Altogether, three demonstrators have been shown. An on-chip demonstrator has been constructed by integrating solution-processed blue OLEC and OPD as well as two orthogonally oriented linear polarizers on a glass chip. **This is the first reported integrated on-chip fluorescence sensor using solution-processed OLEC as an excitation light source and OPD as a detector.** Furthermore, at OLEC brightnesses of 500 and 2000 cd/m², minimum concentrations as low as 1 µM FAM in water with an S/N-ratio > 1.1 was detected. This is better than the state of the art comparable setup with all-evaporated OLEDs and OPDs, which has a projected limit of detection of 10 µM [137]. In addition, a fully solution-processed yellow OLEC has been presented. Transparent inkjet-printed PEDOT:PSS was used for both the cathode and anode with a spin-coated ZnO interlayer. This demonstrated that the OLEC layer structure could be easily transferred to another emitter, and PEDOT:PSS with ZnO interlayer can replace sputtered ITO. At last, in order to further increase the emission brightness, a solution-processed tandem blue OLEC and yellow OLED has been constructed. Through this strategy, theoretically, the maximum emission brightness can be doubled.

In conclusion, this dissertation has demonstrated the research and development of tailing two organic light sources (OLED and OLEC) using a solution-processing technique for microfluidic LoC fluorescence sensing applications. Furthermore, OLEDs have relatively high emission brightnesses yet difficulties in direct chip-integration via cost-efficient manufacturing methods. Thus, an inkjet-printed Al:ZnO:PEI EIL was first introduced to simplify the layer structure of OLED and enable the solution processing of the cathode and EIL at the same time. A fully solution-processing manufacturing recipe for direct chip-integration was developed in the following methods: (1) inkjet-printed PEDOT:PSS bottom electrode; (2) inkjet-printed Al:ZnO:PEI EIL; (3) spin-coated SuperYellow LEP; (4) inkjet-printed PEDOT:PSS top electrodes. Even with a relatively rough bottom electrode, the ITO-free, fully solution-processed OLED emitted a brightness of 16 000 cd/m². It is the first fully solution-processed, bright OLEDs exclusively using inkjet printing as a vacuum-free, mask-free, low processing temperature patterning method. On the other hand, because of the intrinsic doping mechanism, OLEC shows relatively high tolerance on surface roughness, high potential for an all-inkjet-printed manufacturing process, as well as simple and universal layer structure for different emitters. All these advantages make solution-

processed OLEC a promising universal excitation light source for disposable microfluidic LoC devices, specifically for integrating multiple emission colors as well as flexible and non-flat substrates. Currently however, electrochemical doping causes intrinsic low emission brightness and shorter operational lifetime of OLECs. In an effort to overcome this, the influence of dopant concentration and layer thickness on emission brightness was first investigated in voltage-pulsed driving mode. This work suggests that high emission brightnesses can be achieved by reducing dopant concentrations and increasing active layer thicknesses. Moreover, the glass chip demonstrator with fully solution-processed OLEC and OPD as well as integrated linear polarizers showed a better limit of detection than a comparable reported setup [137]. This is the first demonstration showing that OLEC can be used as a fluorescent excitation light source.

The work reported in this dissertation has paved the way for integrating all-inkjet-printed organic light sources directly onto disposable microfluidic LoC systems for multi-purpose fluorescence sensing applications. The previous work has proven that the active layers of RGB OLEDs can also be inkjet printed [55]. Thus, spin-coated active layers can be deposited by inkjet printing, and then organic light sources with different emission wavelength can be locally integrated onto microfluidic chips. In this manner, multiple fluorescent dyes can be simultaneously detected, increasing the sensing abilities of single chips. This also applies to OLECs, where active layers can also be inkjet printed [121] instead of spin-coated to achieve all-inkjet-printed OLECs. Thanks to the relatively high tolerance on surface roughness and flatness, possibilities arise for innovative sensing designs such as printing OLEC on micro-lens array for focusing and printing OLEC on curved optical waveguides. Last but not least, the derived low-cost manufacturing process is compatible with other functionalities integration by inkjet printing such as micro-pumps [7], micro-heaters [8,9], capacitors [37], digital microfluidics [132,133], and micro-channels [134,135]. Hence, disposable monolithic microfluidic LoC systems can be fully inkjet printed.

References

[1]   C. Yi, C.W. Li, S. Ji, M. Yang, Microfluidics technology for manipulation and analysis of biological cells, Anal. Chim. Acta. 560 (1–2) (2006) 1–23.

[2]   K. Yamada, H. Shibata, K. Suzuki, D. Citterio, Toward practical application of paper-based microfluidics for medical diagnostics: state-of-the-art and challenges, Lab Chip. 17 (7) (2017) 1206–1249.

[3]   Lab on a Chip Blog, When microfluidics meets inkjet printing, <http://blogs.rsc.org/lc/2015/03/25/when-microfluidics-meets-inkjet-printing/> (accessed July 27, 2017).

[4]   P. Tseng, C. Murray, D. Kim, D. Di Carlo, Research highlights: printing the future of microfabrication, Lab Chip. 14 (9) (2014) 1491.

[5]   J. Li, F. Rossignol, J. Macdonald, Inkjet printing for biosensor fabrication: combining chemistry and technology for advanced manufacturing., Lab Chip. 15 (12) (2015) 2538–2358.

[6]   O. Pabst, J. Perelaer, E. Beckert, U.S. Schubert, R. Eberhardt, A. Tünnermann, All inkjet-printed piezoelectric polymer actuators: Characterization and applications for micropumps in lab-on-a-chip systems, Org. Electron. 14 (12) (2013) 3423–3429.

[7]   O. Pabst, S. Hölzer, E. Beckert, J. Perelaer, U.S. Schubert, R. Eberhardt, A. Tünnermann, Inkjet printed micropump actuator based on piezoelectric polymers: Device performance and morphology studies, Org. Electron. Physics, Mater. Appl. 15 (11) (2014) 3306–3315.

[8]   C. Hoera, S. Ohla, Z. Shu, E. Beckert, S. Nagl, D. Belder, An integrated microfluidic chip enabling control and spatially resolved monitoring of temperature in micro flow reactors, Anal. Bioanal. Chem. 407 (2) (2015) 387–396.

[9]   C. Hoera, M.M.M. Skadell, S.A. Pfeiffer, M. Pahl, Z. Shu, E. Beckert, D. Belder, A chip-integrated highly variable thermal flow rate sensor, Sensors Actuators B Chem. 225 (2016) 42–49.

[10]   H. Gai, Y. Li, E.S. Yeung, Optical Detection Systems on Microfluidic Chips, in: Top Curr Chem, 2011: pp. 171–201.

[11]   S. Shashkova, M.C. Leake, Single-molecule fluorescence microscopy review: shedding

new light on old problems, Biosci. Rep. 37 (4) (2017).

[12]   F.B. Myers, L.P. Lee, Innovations in optical microfluidic technologies for point-of-care diagnostics, Lab Chip. 8 (12) (2008) 2015.

[13]   M.S. AlSalhi, J. Alam, L.A. Dass, M. Raja, Recent Advances in Conjugated Polymers for Light Emitting Devices, Int. J. Mol. Sci. 12 (3) (2011) 2036–2054.

[14]   E. Manna, F. Fungura, R. Biswas, J. Shinar, R. Shinar, Tunable Near UV Microcavity OLED Arrays: Characterization and Analytical Applications, Adv. Funct. Mater. 25 (8) (2015) 1226–1232.

[15]   M. Ramos-silva, C. Zaldo, P. Chamorro-posada, J. Martín-gil, NIR- OLED (1.54 μm) emitting electroluminescent diode arrays based on Er-complexes manufactured by cost-effective methods, Opt. Pura Y Apl. 46 (3) (2013) 257–263.

[16]   G. Qian, Z. Zhong, M. Luo, D. Yu, Z. Zhang, Z.Y. Wang, D. Ma, Simple and Efficient Near-Infrared Organic Chromophores for Light-Emitting Diodes with Single Electroluminescent Emission above 1000 nm, Adv. Mater. 21 (1) (2009) 111–116.

[17]   R. Liu, Y. Cai, J.-M. Park, K.-M. Ho, J. Shinar, R. Shinar, Organic light-emitting diode sensing platform: Challenges and solutions, Adv. Funct. Mater. 21 (24) (2011) 4744–4753.

[18]   G. Williams, C. Backhouse, H. Aziz, Integration of Organic Light Emitting Diodes and Organic Photodetectors for Lab-on-a-Chip Bio-Detection Systems, Electronics. 3 (1) (2014) 43–75.

[19]   H. Nakanotani, T. Oyamada, Y. Kawamura, H. Sasabe, C. Adachi, Injection and Transport of High Current Density over 1000 A/cm2 in Organic Light Emitting Diodes under Pulse Excitation, Jpn. J. Appl. Phys. 44 (6A) (2005) 3659–3662.

[20]   Dayly Mail Online, Panasonic reveals OLED screen turns into transparent glass when not in use, <http://www.dailymail.co.uk/sciencetech/article-3822108/Panasonic-reveals-invisible-TV-Prototype-OLED-screen-turns-transparent-glass-not-use.html> (accessed April 20, 2017).

[21]   Plusplasticelectronics.com, Audi on track to deliver OLED lighting-equipped cars in 2016, <https://www.plusplasticelectronics.com/electronics/audi-on-track-to-deliver-oled-lighting-equipped-ca> (accessed July 27, 2017).

[22]   Designboom.com, LG Display OLED Design Competition 2016,

<http://www.designboom.com/competition/lg-display-oled-design-competition-2016/> (accessed July 27, 2017).

[23] OLED-Info.com, Mobile phones and smartphones with OLED screens, <http://www.oled-info.com/oled_devices/mobile_phones> (accessed July 27, 2017).

[24] M. Zhang, S. Höfle, J. Czolk, A. Mertens, A. Colsmann, All-solution processed transparent organic light emitting diodes, Nanoscale. 7 (47) (2015) 20009–20014.

[25] S. Höfle, T. Lutz, A. Egel, F. Nickel, S.W. Kettlitz, G. Gomard, U. Lemmer, A. Colsmann, Influence of the Emission Layer Thickness on the Optoelectronic Properties of Solution Processed Organic Light-Emitting Diodes, ACS Photonics. 1 (10) (2014) 968–973.

[26] S. Höfle, A. Schienle, C. Bernhard, M. Bruns, U. Lemmer, A. Colsmann, Solution Processed, White Emitting Tandem Organic Light-Emitting Diodes with Inverted Device Architecture, Adv. Mater. 26 (30) (2014) 5155–5159.

[27] S. Höfle, A. Schienle, M. Bruns, U. Lemmer, A. Colsmann, Enhanced Electron Injection into Inverted Polymer Light-Emitting Diodes by Combined Solution-Processed Zinc Oxide/Polyethylenimine Interlayers, Adv. Mater. 26 (17) (2014) 2750–2754.

[28] S. Stolz, Y. Zhang, U. Lemmer, G. Hernandez-Sosa, H. Aziz, Degradation Mechanisms in Organic Light-Emitting Diodes with Polyethylenimine as a Solution-Processed Electron Injection Layer, ACS Appl. Mater. Interfaces. 9 (3) (2017) 2776–2785.

[29] S. Stolz, M. Petzoldt, N. Kotadiya, T. Rödlmeier, R. Eckstein, J. Freudenberg, U.H.F. Bunz, U. Lemmer, E. Mankel, M. Hamburger, G. Hernandez-Sosa, One-step additive crosslinking of conjugated polyelectrolyte interlayers: improved lifetime and performance of solution-processed OLEDs, J. Mater. Chem. C. 4 (47) (2016) 11150–11156.

[30] S. Stolz, M. Scherer, E. Mankel, R. Lovrinčić, J. Schinke, W. Kowalsky, W. Jaegermann, U. Lemmer, N. Mechau, G. Hernandez-Sosa, Investigation of solution processed ultra-thin electron injection layers for organic light-emitting diodes., ACS Appl. Mater. Interfaces. (2014).

[31] C.H.L. Weijtens, V. van Elsbergen, M.M. de Kok, S.H.P.M. de Winter, Effect of the

alkali metal content on the electronic properties of PEDOT:PSS, Org. Electron. 6 (2) (2005) 97–104.

[32] Z. Yu, Y. Xia, D. Du, J. Ouyang, PEDOT:PSS Films with Metallic Conductivity through a Treatment with Common Organic Solutions of Organic Salts and Their Application as a Transparent Electrode of Polymer Solar Cells, ACS Appl. Mater. Interfaces. 8 (18) (2016) 11629–11638.

[33] J. Ouyang, Solution-Processed PEDOT:PSS Films with Conductivities as Indium Tin Oxide through a Treatment with Mild and Weak Organic Acids, ACS Appl. Mater. Interfaces. 5 (24) (2013) 13082–13088.

[34] Y.K. Seo, C.W. Joo, J. Lee, J.W. Han, N.S. Cho, K.T. Lim, S. Yu, M.H. Kang, C. Yun, B.H. Choi, Y.H. Kim, Efficient ITO-free organic light-emitting diodes comprising PEDOT:PSS transparent electrodes optimized with 2-ethoxyethanol and post treatment, Org. Electron. 42 (2017) 348–354.

[35] Q. Pei, G. Yu, C. Zhang, Y. Yang, A.J. Heeger, Polymer Light-Emitting Electrochemical Cells, Science. 269 (5227) (1995) 1086–1088.

[36] S. Tang, L. Edman, Light-Emitting Electrochemical Cells: A Review on Recent Progress, Top. Curr. Chem. 374 (4) (2016) 40.

[37] S. Khan, L. Lorenzelli, R.S. Dahiya, Technologies for Printing Sensors and Electronics Over Large Flexible Substrates: A Review, IEEE Sens. J. 15 (6) (2015) 3164–3185.

[38] S. Wünscher, S. Stumpf, A. Teichler, O. Pabst, J. Perelaer, E. Beckert, U.S. Schubert, Localized atmospheric plasma sintering of inkjet printed silver nanoparticles, J. Mater. Chem. 22 (47) (2012) 24569.

[39] L. Groenendaal, F. Jonas, D. Freitag, H. Pielartzik, J.R. Reynolds, Poly(3,4-ethylenedioxythiophene) and its derivatives: past, present, and future, Adv. Mater. 12 (7) (2000) 481–494.

[40] F. Jonas, G. Heywang, W. Schmidtberg, J. Heinze, M. Dietrich, Polythiophenes, process for their preparation and their use, US 4959430 A, (1990).

[41] L. Beverina, G.A. Pagani, M. Sassi, Multichromophoric electrochromic polymers: colour tuning of conjugated polymers through the side chain functionalization approach, Chem. Commun. 50 (41) (2014) 5413–5430.

[42] Z.-G. Zhang, Y. Li, Side-chain engineering of high-efficiency conjugated polymer

photovoltaic materials, Sci. China Chem. 58 (2) (2015) 192–209.

[43] C. Sekine, Y. Tsubata, T. Yamada, M. Kitano, S. Doi, Recent progress of high performance polymer OLED and OPV materials for organic printed electronics, Sci. Technol. Adv. Mater. 15 (3) (2014) 34203.

[44] B. Geffroy, P. Le Roy, C. Prat, Organic light-emitting diode (OLED) technology: materials, devices and display technologies, Polym. Int. 55 (6) (2006) 572–582.

[45] J. Fan, M.-K. Fung, J. Tang, L. Liao, Research perspectives on efficient and large-area OLED lighting, Imaging Sci. Photochem. 35 (1) (2017) 26–33.

[46] S. Ho, S. Liu, Y. Chen, F. So, Review of recent progress in multilayer solution-processed organic light-emitting diodes, J. Photonics Energy. 5 (1) (2015) 57611.

[47] S. Jung, A. Sou, K. Banger, D.-H. Ko, P.C.Y. Chow, C.R. McNeill, H. Sirringhaus, All-Inkjet-Printed, All-Air-Processed Solar Cells, Adv. Energy Mater. 4 (14) (2014) 1400432.

[48] R.D. Jansen-van Vuuren, A. Armin, A.K. Pandey, P.L. Burn, P. Meredith, Organic Photodiodes: The Future of Full Color Detection and Image Sensing, Adv. Mater. 28 (24) (2016) 4766–4802.

[49] B. Kang, W.H. Lee, K. Cho, Recent Advances in Organic Transistor Printing Processes, ACS Appl. Mater. Interfaces. 5 (7) (2013) 2302–2315.

[50] M. Shibata, Y. Sakai, D. Yokoyama, Advantages and disadvantages of vacuum-deposited and spin-coated amorphous organic semiconductor films for organic light-emitting diodes, J. Mater. Chem. C. 3 (42) (2015) 11178–11191.

[51] K. Gilissen, J. Stryckers, P. Verstappen, J. Drijkoningen, G.H.L. Heintges, L. Lutsen, J. Manca, W. Maes, W. Deferme, Ultrasonic spray coating as deposition technique for the light-emitting layer in polymer LEDs, Org. Electron. 20 (2015) 31–35.

[52] Y. Chen, J. Wang, Z. Zhong, Z. Jiang, C. Song, Z. Hu, J. Peng, J. Wang, Y. Cao, Fabricating large-area white OLED lighting panels via dip-coating, Org. Electron. 37 (2016) 458–464.

[53] S.M. Raupp, L. Merklein, M. Pathak, P. Scharfer, W. Schabel, An experimental study on the reproducibility of different multilayer OLED materials processed by slot die coating, Chem. Eng. Sci. 160 (2017) 113–120.

[54] M.J.J. Coenen, T.M.W.L. Slaats, T.M. Eggenhuisen, P. Groen, Inkjet printing the three organic functional layers of two-colored organic light emitting diodes, Thin Solid Films. 583 (2015) 194–200.

[55] A. Teichler, Z. Shu, A. Wild, C. Bader, J. Nowotny, G. Kirchner, S. Harkema, J. Perelaer, U.S. Schubert, Inkjet printing of chemically tailored light-emitting polymers, Eur. Polym. J. 49 (8) (2013) 2186–2195.

[56] D. Lee, K.H. Lee, H. Shin, Y.P. Liu, S.M. Cho, Large-Area OLED Lighting Fabricated by Screen Printing, in: IDW '09 - Proc. 16th Int. Disp. Work., 2009.

[57] A. Kim, H. Lee, J. Lee, S.M. Cho, H. Chae, Bi-Layer Gravure Printed Nanoscale Thick Organic Layers for Organic Light Emitting Diode, J. Nanosci. Nanotechnol. 11 (1) (2011) 546–549.

[58] D. Threm, J.L. Gugat, A. Pradana, M. Radler, J. Mikat, M. Gerken, Self-Aligned Integration of Spin-Coated Organic Light-Emitting Diodes and Photodetectors on a Single Substrate, IEEE Photonics Technol. Lett. 24 (11) (2012) 912–914.

[59] L. Duan, L. Hou, T.-W. Lee, J. Qiao, D. Zhang, G. Dong, L. Wang, Y. Qiu, Solution processable small molecules for organic light-emitting diodes, J. Mater. Chem. 20 (31) (2010) 6392.

[60] D.B. Hall, P. Underhill, J.M. Torkelson, Spin coating of thin and ultrathin polymer films, Polym. Eng. Sci. 38 (12) (1998) 2039–2045.

[61] D. Tobjörk, R. Österbacka, Paper Electronics, Adv. Mater. 23 (17) (2011) 1935–1961.

[62] D.J. Gaspar, E. Polikarpov, eds., OLED Fundamentals: Materials, Devices, and Processing of Organic Light-Emitting Diodes, CRC Press, 2015.

[63] G.E. Jabbour, N. Peyghambarian, Screen Printing for Organic-Based Photonics And Electronics, Opt. Photonics News. 12 (12) (2001) 27.

[64] K.C. Chaudhary, L.G. Redekopp, The nonlinear capillary instability of a liquid jet. Part 1. Theory, J. Fluid Mech. 96 (2) (1980) 257–274.

[65] Junfeng Mei, M.R. Lovell, M.H. Mickle, Formulation and processing of novel conductive solution inks in continuous inkjet printing of 3-D electric circuits, IEEE Trans. Electron. Packag. Manuf. 28 (3) (2005) 265–273.

[66] B. Derby, Inkjet Printing of Functional and Structural Materials: Fluid Property

Requirements, Feature Stability, and Resolution, Annu. Rev. Mater. Res. 40 (1) (2010) 395–414.

[67]   D.B. Bogy, F.E. Talke, Experimental and Theoretical Study of Wave Propagation Phenomena in Drop-on-Demand Ink Jet Devices, IBM J. Res. Dev. 28 (3) (1984) 314–321.

[68]   J.R. Castrejon-Pita, W.R.S. Baxter, J. Morgan, S. Temple, G.D. Martin, I.M. Hutchings, Future, opportunities and challenges of inkjet technologies, At. Sprays. 23 (6) (2013) 541–565.

[69]   Z. Yin, Y. Huang, N. Bu, X. Wang, Y. Xiong, Inkjet printing for flexible electronics: Materials, processes and equipments, Chinese Sci. Bull. 55 (30) (2010) 3383–3407.

[70]   H. Liu, H. Zheng, W. Xu, J. Peng, Ink-Jet Printing Organic Light-Emitting Diode (OLED) Displays: Technology and Development, Mater. China. 33 (3) (2014) 37–48.

[71]   J. Perelaer, U.S. Schubert, Novel approaches for low temperature sintering of inkjet-printed inorganic nanoparticles for roll-to-roll (R2R) applications, J. Mater. Res. 28 (4) (2013) 564–573.

[72]   G. Tomaszewski, P. Jankowski-Mihułowicz, M. Węglarski, W. Lichoń, Inkjet-printed flexible RFID antenna for UHF RFID transponders, Mater. Sci. 34 (4) (2016) 760–769.

[73]   K. Koski, E. Koski, J. Virtanen, T. Björninen, L. Sydänheimo, L. Ukkonen, A.Z. Elsherbeni, Inkjet-printed passive UHF RFID tags: review and performance evaluation, Int. J. Adv. Manuf. Technol. 62 (1–4) (2012) 167–182.

[74]   C.F. Madigan, C.R. Hauf, L.D. Barkley, N. Harjee, E. Vronsky, S.A. Van Slyke, Advancements in Inkjet Printing for OLED Mass Production, SID Symp. Dig. Tech. Pap. 45 (1) (2014) 399–402.

[75]   A. Verma, D.M. Zink, C. Fléchon, J. Leganés Carballo, H. Flügge, J.M. Navarro, T. Baumann, D. Volz, Efficient, inkjet-printed TADF-OLEDs with an ultra-soluble NHetPHOS complex, Appl. Phys. A. 122 (3) (2016) 191.

[76]   G. Azzellino, A. Grimoldi, M. Binda, M. Caironi, D. Natali, M. Sampietro, Fully Inkjet-Printed Organic Photodetectors with High Quantum Yield, Adv. Mater. 25 (47) (2013) 6829–6833.

[77]   T.M. Eggenhuisen, Y. Galagan, A.F.K. V. Biezemans, T.M.W.L. Slaats, W.P. Voorthuijzen, S. Kommeren, S. Shanmugam, J.P. Teunissen, A. Hadipour, W.J.H.

Verhees, S.C. Veenstra, M.J.J. Coenen, J. Gilot, R. Andriessen, W. a. Groen, High efficiency, fully inkjet printed organic solar cells with freedom of design, J. Mater. Chem. A. 3 (14) (2015) 7255–7262.

[78] M. Ren, J. Sweelssen, N. Grossiord, H. Gorter, T.M. Eggenhuisen, R. Andriessen, Inkjet Printing Technology for OPV Applications, J. Imaging Sci. Technol. 56 (4) (2012) 1–5.

[79] Y.-J. Kwon, Y. Park, W. Lee, Inkjet-Printed Organic Transistors Based on Organic Semiconductor/Insulating Polymer Blends, Materials. 9 (8) (2016) 650.

[80] P.J. Yunker, T. Still, M.A. Lohr, A.G. Yodh, Suppression of the coffee-ring effect by shape-dependent capillary interactions, Nature. 476 (7360) (2011) 308–311.

[81] W. Helfrich, W.G. Schneider, Recombination Radiation in Anthracene Crystals, Phys. Rev. Lett. 14 (7) (1965) 229–231.

[82] C.W. Tang, S.A. VanSlyke, Organic electroluminescent diodes, Appl. Phys. Lett. 51 (12) (1987) 913.

[83] AndroidAuthority.com, Galaxy S6 Edge demand is to blame for Samsung's poor Q2, <http://www.androidauthority.com/galaxy-s6-edge-demand-is-to-blame-for-samsungs-poor-q2-623118/> (accessed July 27, 2017).

[84] OLED-info.com, OLED TVs: introduction and market status, <http://www.oled-info.com/oled-tv> (accessed July 27, 2017).

[85] PrintedElectronicNow.com, PE USA 2016 Shows Growth of Flexible Electronics, <http://www.printedelectronicsnow.com/live-from-shows/printed-electronics-usa/2016-11-23/pe-usa-2016-shows-growth-of-flexible-electronics/?email_uid=7ef71866ac/list_id=b41ded4d91/> (accessed July 27, 2017).

[86] S. Schols, Device Architecture and Materials for Organic Light-Emitting Devices, Springer Netherlands, 2011.

[87] T. Yu, L. Liu, Z. Xie, Y. Ma, Progress in small-molecule luminescent materials for organic light-emitting diodes, Sci. China Chem. 58 (6) (2015) 907–915.

[88] J. H. Burroughes, D. D. C. Bradley, A. R. Brown, R. N. Marks, K. Mackay, P.L.B.& A.B.H. R. H. Friend, J.H. Burroughes, D.D.C. Bradley, A.R. Brown, R.N. Marks, K. Mackay, R.H. Friend, P.L. Burns, A.B. Holmes, Light-emitting diodes based on conjugated polymers, Nature. 347 (6293) (1990) 539–541.

[89]   G. Zucchi, D. Tondelier, Y. Bonnassieux, B. Geffroy, Improving the performance of polymer light-emitting devices with chemical tools, Polym. Int. 63 (8) (2014) 1368–1377.

[90]   M. Pope, C.S. Swenberg, Electronic Processes in organic Crystals and Polymers, 2nd ed., Oxford University Press, New York, 1999.

[91]   P.W.M. Blom, M.J.M. De Jong, Electrical characterization of polymer light-emitting diodes, IEEE J. Sel. Top. Quantum Electron. 4 (1) (1998) 105–112.

[92]   J.-H. Jou, S. Kumar, A. Agrawal, T.-H. Li, S. Sahoo, Approaches for fabricating high efficiency organic light emitting diodes, J. Mater. Chem. C. 3 (13) (2015) 2974–3002.

[93]   R. Meerheim, B. Lussem, K. Leo, Efficiency and Stability of p-i-n Type Organic Light Emitting Diodes for Display and Lighting Applications, in: Proc. IEEE, 2009: pp. 1606–1626.

[94]   Y. Li, X. Hu, S. Zhou, L. Yang, J. Yan, C. Sun, P. Chen, A facile process to produce highly conductive poly(3,4-ethylenedioxythiophene) films for ITO-free flexible OLED devices, J. Mater. Chem. C. 2 (5) (2014) 916–924.

[95]   A.I. Hofmann, W.T.T. Smaal, M. Mumtaz, D. Katsigiannopoulos, C. Brochon, F. Schütze, O.R. Hild, E. Cloutet, G. Hadziioannou, An Alternative Anionic Polyelectrolyte for Aqueous PEDOT Dispersions: Toward Printable Transparent Electrodes, Angew. Chemie Int. Ed. 54 (29) (2015) 8506–8510.

[96]   R. Xing, T. Ye, Y. Ding, Z. Ding, D. Ma, Y. Han, Thickness uniformity adjustment of inkjet printed light-emitting polymer films by solvent mixture, Chinese J. Chem. 31 (11) (2013) 1449–1454.

[97]   F. Villani, P. Vacca, G. Nenna, O. Valentino, G. Burrasca, T. Fasolino, C. Minarini, D. Della Sala, Inkjet printed polymer layer on flexible substrate for OLED applications, J. Phys. Chem. C. 113 (30) (2009) 13398–13402.

[98]   S.-H. Lee, J.Y. Hwang, K. Kang, H. Kang, Fabrication of organic light emitting display using inkjet printing technology, in: 2009 Int. Symp. Optomechatronic Technol., IEEE, 2009: pp. 71–76.

[99]   C. Zhong, C. Duan, F. Huang, H. Wu, Y. Cao, Materials and devices toward fully solution processable organic light-emitting diodes, Chem. Mater. 23 (3) (2011) 326–340.

[100] L. Derue, S. Olivier, D. Tondelier, T. Maindron, B. Geffroy, E. Ishow, All-Solution-Processed Organic Light-Emitting Diodes Based on Photostable Photo-cross-linkable Fluorescent Small Molecules, ACS Appl. Mater. Interfaces. 8 (25) (2016) 16207–16217.

[101] F. Hermerschmidt, I. Burgués-Ceballos, A. Savva, E.D. Sepos, A. Lange, C. Boeffel, S. Nau, E.J.W. List-Kratochvil, S.A. Choulis, High performance indium tin oxide-free solution-processed organic light emitting diodes based on inkjet-printed fine silver grid lines, Flex. Print. Electron. 1 (3) (2016) 35004.

[102] Y. Zhou, C. Fuentes-Hernandez, J. Shim, J. Meyer, A.J. Giordano, H. Li, P. Winget, T. Papadopoulos, H. Cheun, J. Kim, M. Fenoll, A. Dindar, W. Haske, E. Najafabadi, T.M. Khan, H. Sojoudi, S. Barlow, S. Graham, J.-L. Bredas, S.R. Marder, A. Kahn, B. Kippelen, A Universal Method to Produce Low-Work Function Electrodes for Organic Electronics, Science. 336 (6079) (2012) 327–332.

[103] R. Kaçar, S.P. Mucur, F. Yıldız, S. Dabak, E. Tekin, Highly efficient inverted organic light emitting diodes by inserting a zinc oxide/polyethyleneimine (ZnO:PEI) nano-composite interfacial layer, Nanotechnology. 28 (24) (2017) 245204.

[104] J.-K. Lee, D.S. Yoo, E.S. Handy, M.F. Rubner, Thin film light emitting devices from an electroluminescent ruthenium complex, Appl. Phys. Lett. 69 (12) (1996) 1686–1688.

[105] G. Gozzi, L.D. Cagnani, R.M. Faria, L.F. Santos, Electrical properties of electrochemically doped organic semiconductors using light-emitting electrochemical cells, J. Solid State Electrochem. 20 (8) (2016) 2127–2133.

[106] J. Gao, J. Dane, Imaging the doping and electroluminescence in extremely large planar polymer light-emitting electrochemical cells, J. Appl. Phys. 98 (6) (2005) 63513.

[107] S. van Reenen, P. Matyba, A. Dzwilewski, R.A.J. Janssen, L. Edman, M. Kemerink, A Unifying Model for the Operation of Light-Emitting Electrochemical Cells, J. Am. Chem. Soc. 132 (39) (2010) 13776–13781.

[108] J.D. Slinker, J. a DeFranco, M.J. Jaquith, W.R. Silveira, Y. Zhong, J.M. Moran-Mirabal, H.G. Craighead, H.D. Abruña, J. a Marohn, G.G. Malliaras, Direct measurement of the electric-field distribution in a light-emitting electrochemical cell., Nat. Mater. 6 (11) (2007) 894–899.

[109] Y. Hu, J. Gao, Direct Imaging and Probing of the p−n Junction in a Planar Polymer Light-Emitting Electrochemical Cell, J. Am. Chem. Soc. 133 (7) (2011) 2227–2231.

[110] J.H. Shin, N.D. Robinson, S. Xiao, L. Edman, Polymer light-emitting electrochemical cells: Doping concentration, emission-zone position, and turn-on time, Adv. Funct. Mater. 17 (11) (2007) 1807–1813.

[111] S. van Reenen, P. Matyba, A. Dzwilewski, R.A.J. Janssen, L. Edman, M. Kemerink, Salt concentration effects in planar light-emitting electrochemical cells, Adv. Funct. Mater. 21 (10) (2011) 1795–1802.

[112] P. Matyba, M.R. Andersson, L. Edman, On the desired properties of a conjugated polymer-electrolyte blend in a light-emitting electrochemical cell, Org. Electron. 9 (5) (2008) 699–710.

[113] Z. Yu, M. Wang, G. Lei, J. Liu, L. Li, Q. Pei, Stabilizing the Dynamic p−i−n Junction in Polymer Light-Emitting Electrochemical Cells, J. Phys. Chem. Lett. 2 (5) (2011) 367–372.

[114] J. Mindemark, L. Edman, Illuminating the electrolyte in light-emitting electrochemical cells, J. Mater. Chem. C. 4 (3) (2016) 420–432.

[115] T.D. Shoji, Z. Zhu, J.M. Leger, Characterizing ion profiles in dynamic junction light-emitting electrochemical cells, ACS Appl. Mater. Interfaces. 5 (22) (2013) 11509–11514.

[116] J.H. Shin, P. Matyba, N.D. Robinson, L. Edman, The influence of electrodes on the performance of light-emitting electrochemical cells, Electrochim. Acta. 52 (23) (2007) 6456–6462.

[117] A. Sandström, H.F. Dam, F.C. Krebs, L. Edman, Ambient fabrication of flexible and large-area organic light-emitting devices using slot-die coating, Nat Commun. 3 (2012) 1002.

[118] A. Sandström, A. Asadpoordarvish, J. Enevold, L. Edman, Spraying Light: Ambient-Air Fabrication of Large-Area Emissive Devices on Complex-Shaped Surfaces, Adv. Mater. 26 (29) (2014) 4975–4980.

[119] G. Hernandez-Sosa, S. Tekoglu, S. Stolz, R. Eckstein, C. Teusch, J. Trapp, U. Lemmer, M. Hamburger, N. Mechau, The Compromises of Printing Organic Electronics: A Case Study of Gravure-Printed Light-Emitting Electrochemical Cells, Adv. Mater. 26 (20)

(2014) 3235–3240.

[120] E.M. Lindh, A. Sandstroem, L. Edman, Inkjet printed bilayer light-emitting electrochemical cells for display and lighting applications, Small. 10 (20) (2014) 4148–4153.

[121] G. Mauthner, K. Landfester, A. Köck, H. Brückl, M. Kast, C. Stepper, E.J.W. List, Inkjet printed surface cell light-emitting devices from a water-based polymer dispersion, Org. Electron. 9 (2) (2008) 164–170.

[122] P. Matyba, H. Yamaguchi, G. Eda, M. Chhowalla, L. Edman, N.D. Robinson, Graphene and mobile ions: The key to all-plastic, solution-processed light-emitting devices, ACS Nano. 4 (2) (2010) 637–642.

[123] J. Liang, L. Li, X. Niu, Z. Yu, Q. Pei, Fully Solution-Based Fabrication of Flexible Light-Emitting Device at Ambient Conditions, J. Phys. Chem. C. 117 (32) (2013) 16632–16639.

[124] A. Asadpoordarvish, A. Sandström, C. Larsen, R. Bollström, M. Toivakka, R. Österbacka, L. Edman, Light-emitting paper, Adv. Funct. Mater. 25 (21) (2015) 3238–3245.

[125] Z. Zhang, K. Guo, Y. Li, X. Li, G. Guan, H. Li, Y. Luo, F. Zhao, Q. Zhang, B. Wei, Q. Pei, H. Peng, A colour-tunable, weavable fibre-shaped polymer light-emitting electrochemical cell, Nat. Photonics. 9 (2015) 233–238.

[126] T. Lanz, A. Sandström, S. Tang, P. Chabrecek, U. Sonderegger, L. Edman, A light–emission textile device: conformal spray-sintering of a woven fabric electrode, Flex. Print. Electron. 1 (2) (2016) 25004.

[127] C.D. Chin, V. Linder, S.K. Sia, Commercialization of microfluidic point-of-care diagnostic devices, Lab Chip. 12 (12) (2012) 2118–2134.

[128] C.D. Chin, V. Linder, S.K. Sia, A.S. Daar, H. Thorsteinsdottir, D.K. Martin, Lab-on-a-chip devices for global health: Past studies and future opportunities, Lab Chip. 7 (1) (2007) 41–57.

[129] A. St John, C.P. Price, Existing and Emerging Technologies for Point-of-Care Testing, Clin. Biochem. Rev. 35 (3) (2014) 155–167.

[130] E. Beckert, R. Eberhardt, O. Pabst, F. Kemper, Z. Shu, A. Tünnermann, J. Perelaer, U. Schubert, H. Becker, Inkjet printed structures for smart lab-on-chip systems, in: H.

Becker, B.L. Gray (Eds.), Proc. SPIE 8615, Microfluid. BioMEMS, Med. Microsystems XI, International Society for Optics and Photonics, San Francisco, California, United States, 2013: p. 86150E.

[131] T. -a. Meier, E. Poehler, F. Kemper, O. Pabst, H.-G. Jahnke, E. Beckert, A. Robitzki, D. Belder, Fast electrically assisted regeneration of on-chip SERS substrates, Lab Chip. 15 (14) (2015) 2923–2927.

[132] R. Fobel, A.E. Kirby, A.H.C. Ng, R.R. Farnood, A.R. Wheeler, Paper Microfluidics Goes Digital, Adv. Mater. 26 (18) (2014) 2838–2843.

[133] H. Ko, J. Lee, Y. Kim, B. Lee, C.-H. Jung, J.-H. Choi, O.-S. Kwon, K. Shin, Active Digital Microfluidic Paper Chips with Inkjet-Printed Patterned Electrodes, Adv. Mater. 26 (15) (2014) 2335–2340.

[134] K. Maejima, T. Enomae, A. Isogai, K. Suzuki, D. Citterio, All-inkjet-printed "lab-on-paper" with Electrodes and Microchannels, in: NIP28 Int. Conf. Digit. Print. Technol. Digit. Fabr. 2012, 2012: pp. 554–556.

[135] Y. Guo, L. Li, F. Li, H. Zhou, Y. Song, Inkjet print microchannels based on a liquid template, Lab Chip. 15 (7) (2015) 1759–1764.

[136] G. Meller, T. Grasser, Organic Electronics, Springer Berlin Heidelberg, Berlin, Heidelberg, 2010.

[137] A. Pais, A. Banerjee, D. Klotzkin, I. Papautsky, High-sensitivity, disposable lab-on-a-chip with thin-film organic electronics for fluorescence detection, Lab Chip. 8 (5) (2008) 794.

[138] K.S. Shin, Y.H. Kim, K.K. Paek, J.H. Park, E.G. Yang, T.S. Kim, J.Y. Kang, B.K. Ju, Characterization of an integrated fluorescence-detection hybrid device with photodiode and organic light-emitting diode, IEEE Electron Device Lett. 27 (9) (2006) 746–748.

[139] F. Lefèvre, A. Chalifour, L. Yu, V. Chodavarapu, P. Juneau, R. Izquierdo, Algal fluorescence sensor integrated into a microfluidic chip for water pollutant detection, Lab Chip. 12 (4) (2012) 787–793.

[140] Y. Shuai, A. Banerjee, D. Klotzkin, I. Papautsky, On-chip fluorescence detection with organic thin film devices for disposable lab-on-a-chip sensors, in: Proc. IEEE Sensors, 2008: pp. 122–125.

[141] L. Schöler, K. Seibel, K. Panczyk, M. Böhm, An integrated PLED - A light source for

application specific lab-on-microchips (ALM), Microelectron. Eng. 86 (4–6) (2009) 1502–1504.

[142] O. Hofmann, X. Wang, J.C. deMello, D.D.C. Bradley, A.J. deMello, Towards microalbuminuria determination on a disposable diagnostic microchip with integrated fluorescence detection based on thin-film organic light emitting diodes, Lab Chip. 5 (8) (2005) 863–868.

[143] A.F. Henwood, E. Zysman-Colman, Luminescent Iridium Complexes Used in Light-Emitting Electrochemical Cells (LEECs), Top. Curr. Chem. 374 (4) (2016) 36.

[144] S. Burns, J. MacLeod, T. Trang Do, P. Sonar, S.D. Yambem, Effect of thermal annealing Super Yellow emissive layer on efficiency of OLEDs, Sci. Rep. 7 (2017) 40805.

[145] S. Tang, L. Edman, Quest for an Appropriate Electrolyte for High-Performance Light-Emitting Electrochemical Cells, J. Phys. Chem. Lett. 1 (18) (2010) 2727–2732.

[146] S.R. Tseng, Y.S. Chen, H.F. Meng, H.C. Lai, C.H. Yeh, S.F. Horng, H.H. Liao, C.S. Hsu, Electron transport and electroluminescent efficiency of conjugated polymers, Synth. Met. 159 (1–2) (2009) 137–141.

[147] S.D. Yambem, M. Ullah, K. Tandy, P.L. Burn, E.B. Namdas, ITO-free top emitting organic light emitting diodes with enhanced light out-coupling, Laser Photon. Rev. 8 (1) (2014) 165–171.

[148] Y.-H.H. Kim, T.-H.H. Han, H. Cho, S.-Y.Y. Min, C.-L.L. Lee, T.-W.W. Lee, Polyethylene imine as an ideal interlayer for highly efficient inverted polymer light-emitting diodes, Adv. Funct. Mater. 24 (24) (2014) 3808–3814.

[149] S. van Reenen, R.A.J. Janssen, M. Kemerink, Fundamental tradeoff between emission intensity and efficiency in light-emitting electrochemical cells, Adv. Funct. Mater. 25 (20) (2014) 3066–3073.

[150] S.B. Meier, D. Tordera, A. Pertegás, C. Roldán-Carmona, E. Ortí-, H.J. Bolink, E. Ortí, H.J. Bolink, Light-emitting electrochemical cells: recent progress and future prospects, Mater. Today. 17 (5) (2014) 217–223.

[151] G. Yu, Y. Cao, M. Andersson, J. Gao, A.J. Heeger, Polymer Light-Emitting Electrochemical Cells with Frozen p-i-n Junction at Room Temperature, Adv. Mater. 10 (5) (1998) 385–388.

[152] T.-B. Song, N. Li, Emerging Transparent Conducting Electrodes for Organic Light Emitting Diodes, Electronics. 3 (1) (2014) 190–204.

[153] K. Tominaga, T. Ueda, T. Ao, M. Kataoka, I. Mori, ITO films prepared by facing target sputtering system, Thin Solid Films. 281–282 (1996) 194–197.

[154] K. Fehse, K. Walzer, K. Leo, W. Lövenich, A. Elschner, Highly Conductive Polymer Anodes as Replacements for Inorganic Materials in High-Efficiency Organic Light-Emitting Diodes, Adv. Mater. 19 (3) (2007) 441–444.

[155] T. Arii, A. Kishi, Humidity controlled thermal analysis: The effect of humidity on thermal decomposition of zinc acetylacetonate monohydrate, J. Therm. Anal. Calorim. 83 (1) (2006) 253–260.

[156] B.H. Cumpston, I.D. Parker, K.F. Jensen, In situ characterization of the oxidative degradation of a polymeric light emitting device, J. Appl. Phys. 81 (8) (1997) 3716–3720.

[157] F. So, D. Kondakov, Degradation Mechanisms in Small-Molecule and Polymer Organic Light-Emitting Diodes, Adv. Mater. 22 (34) (2010) 3762–3777.

[158] M. Schaer, F. Nüesch, D. Berner, W. Leo, L. Zuppiroli, Water Vapor and Oxygen Degradation Mechanisms in Organic Light Emitting Diodes, Adv. Funct. Mater. 11 (2) (2001) 116–121.

[159] K. Tvingstedt, O. Malinkiewicz, A. Baumann, C. Deibel, H.J. Snaith, V. Dyakonov, H.J. Bolink, Radiative efficiency of lead iodide based perovskite solar cells, Sci. Rep. 4 (1) (2015) 6071.

[160] A. Asadpoordarvish, A. Sandström, S. Tang, J. Granström, L. Edman, Encapsulating light-emitting electrochemical cells for improved performance, Appl. Phys. Lett. 100 (19) (2012) 193508.

[161] D.G. Georgiadou, M. Vasilopoulou, L.C. Palilis, I.D. Petsalakis, G. Theodorakopoulos, V. Constantoudis, S. Kennou, A. Karantonis, D. Dimotikali, P. Argitis, All-organic sulfonium salts acting as efficient solution processed electron injection layer for PLEDs, ACS Appl. Mater. Interfaces. 5 (23) (2013) 12346–12354.

[162] M. Park, K.S. Lee, J. Shim, Y. Liu, C. Lee, H. Cho, M.J. Kim, S.-J. Park, Y.J. Yun, H.Y. Kim, D.I. Son, Environment friendly, transparent nanofiber textiles consolidated with high efficiency PLEDs for wearable electronics, Org. Electron. 36 (2016) 89–96.

[163] Youngkyoo Kim and Chang-Sik Ha, Advances in Organic Light-Emitting Device, softcover, Trans Tech Publications, 2008.

[164] L.J. Rothberg, A.J. Lovinger, Status of and prospects for organic electroluminescence, J. Mater. Res. 11 (12) (1996) 3174–3187.

[165] H. Uoyama, K. Goushi, K. Shizu, H. Nomura, C. Adachi, Highly efficient organic light-emitting diodes from delayed fluorescence, Nature. 492 (7428) (2012) 234–238.

[166] N.C. Greenham, R.H. Friend, D.D.C. Bradley, Angular Dependence of the Emission from a Conjugated Polymer Light-Emitting Diode: Implications for efficiency calculations, Adv. Mater. 6 (6) (1994) 491–494.

[167] R. Mac Ciarnain, D. Michaelis, T. Wehlus, A.F. Rausch, N. Danz, A. Bräuer, A. Tünnermann, Emission from outside of the emission layer in state-of-the-art phosphorescent organic light-emitting diodes, Org. Electron. 44 (2017) 115–119.

[168] S. van Reenen, R.A.J. Janssen, M. Kemerink, Dynamic Processes in Sandwich Polymer Light-Emitting Electrochemical Cells, Adv. Funct. Mater. 22 (21) (2012) 4547–4556.

[169] S. Van Reenen, R.A.J. Janssen, M. Kemerink, Doping dynamics in light-emitting electrochemical cells, Org. Electron. Physics, Mater. Appl. 12 (10) (2011) 1746–1753.

[170] R.H. Fowler, L. Nordheim, Electron Emission in Intense Electric Fields, Proc. R. Soc. A Math. Phys. Eng. Sci. 119 (781) (1928) 173–181.

[171] P.R. Emtage, J. O'Dwyer, J.J. O'Dwyerf, Richardson-Schottky Effect in Insulators, Phys. Rev. Lett. 16 (9) (1966) 1964–1966.

[172] R. Meerheim, M. Furno, S. Hofmann, B. Lüssem, K. Leo, Quantification of energy loss mechanisms in organic light-emitting diodes, Appl. Phys. Lett. 97 (25) (2010) 253305.

[173] C. Murawski, K. Leo, M.C. Gather, Efficiency roll-off in organic light-emitting diodes, Adv. Mater. 25 (47) (2013) 6801–6827.

[174] J.J. Park, S.T. Lee, T.J. Park, W.S. Jeon, J. Jang, J.H. Kwon, R. Pode, Stable efficiency roll-off in solution-processed phosphorescent green organic light-emitting diodes, J. Korean Phys. Soc. 55 (1) (2009) 327–330.

[175] H. Nakanotani, H. Sasabe, C. Adachi, Singlet-singlet and singlet-heat annihilations in fluorescence-based organic light-emitting diodes under steady-state high current

density, Appl. Phys. Lett. 86 (21) (2005) 1–3.

[176] M.A. Baldo, C. Adachi, S.R. Forrest, Transient analysis of organic electrophosphorescence. II. Transient analysis of triplet-triplet annihilation, Phys. Rev. B - Condens. Matter Mater. Phys. 62 (16) (2000) 10967–10977.

[177] S. Reineke, K. Walzer, K. Leo, Triplet-exciton quenching in organic phosphorescent light-emitting diodes with Ir-based emitters, Phys. Rev. B. 75 (12) (2007) 125328.

[178] Z. Gao, F. Wang, K. Guo, H. Wang, B. Wei, B. Xu, Carrier transfer and luminescence characteristics of concentration-dependent phosphorescent Ir(ppy)3 doped CBP film, Opt. Laser Technol. 56 (2014) 20–24.

[179] N.C. Giebink, S.R. Forrest, Quantum efficiency roll-off at high brightness in fluorescent and phosphorescent organic light emitting diodes, Phys. Rev. B. 77 (23) (2008) 235215.

[180] Y.-S. Park, W.-I. Jeong, J.-J. Kim, Energy transfer from exciplexes to dopants and its effect on efficiency of organic light-emitting diodes, J. Appl. Phys. 110 (12) (2011) 124519.

[181] B. Ruhstaller, B. Perucco, D. Rezzonico, E. Knapp, Advanced numerical simulation of organic light-emitting devices, in: O. Sergiyenko (Ed.), Optoelectron. Devices Prop., InTech, 2011.

[182] N. Kaihovirta, A. Asadpoordarvish, A. Sandstr?m, L. Edman, Doping-Induced Self-Absorption in Light-Emitting Electrochemical Cells, ACS Photonics. 1 (3) (2014) 182–189.

[183] J. Fang, P. Matyba, N.D. Robinson, L. Edman, Identifying and alleviating electrochemical side-reactions in light-emitting electrochemical cells, J. Am. Chem. Soc. 130 (13) (2008) 4562–4568.

[184] P. Dyreklev, O. Inganäs, J. Paloheimo, H. Stubb, Photoluminescence quenching in a polymer thin-film field-effect luministor, J. Appl. Phys. 71 (6) (1992) 2816–2820.

[185] S. Hayashi, K. Kaneto, K. Yoshino, Quenching of photoluminescence in poly(thiophene) films by electrochemical doping, Solid State Commun. 61 (4) (1987) 249–251.

[186] X. Li, J. Gao, G. Liu, Reversible luminance decay in polymer light-emitting electrochemical cells, Appl. Phys. Lett. 102 (22) (2013) 223303.

[187] R.D. Scurlock, B. Wang, P.R. Ogilby, J.R. Sheats, R.L. Clough, Singlet Oxygen as a Reactive Intermediate in the Photodegradation of an Electroluminescent Polymer, J. Am. Chem. Soc. 117 (41) (1995) 10194–10202.

[188] M. Atreya, S. Li, E.. Kang, K.. Neoh, Z.. Ma, K.. Tan, W. Huang, Stability studies of poly(2-methoxy-5-(2′-ethyl hexyloxy)-p- (phenylene vinylene) [MEH-PPV], Polym. Degrad. Stab. 65 (2) (1999) 287–296.

[189] P.R.F. Rocha, H.L. Gomes, K. Asadi, I. Katsouras, B. Bory, F. Verbakel, P. van de Weijer, D.M. de Leeuw, S.C.J. Meskers, Sudden death of organic light-emitting diodes, Org. Electron. 20 (2015) 89–96.

[190] S.B. Meier, D. Hartmann, D. Tordera, H.J. Bolink, A. Winnacker, W. Sarfert, Dynamic doping and degradation in sandwich-type light-emitting electrochemical cells, Phys. Chem. Chem. Phys. 14 (31) (2012) 10886–10890.

[191] D. Hohertz, J. Gao, How Electrode Work Function Affects Doping and Electroluminescence of Polymer Light-Emitting Electrochemical Cells, Adv. Mater. 20 (17) (2008) 3298–3302.

[192] M. Ullah, K. Tandy, S.D. Yambem, M. Aljada, P.L. Burn, P. Meredith, E.B. Namdas, Simultaneous Enhancement of Brightness, Efficiency, and Switching in RGB Organic Light Emitting Transistors, Adv. Mater. 25 (43) (2013) 6213–6218.

[193] T.-W. Wang, H.-C. Su, Extracting evolution of recombination zone position in sandwiched solid-state light-emitting electrochemical cells by employing microcavity effect, Org. Electron. 14 (9) (2013) 2269–2277.

[194] A. Coens, M. Chakaroun, A.P. Fischer, M.W. Lee, A. Boudrioua, J. Solard, B. Geffroy, Experimental and theoretical study of the optical and electrical properties optimization of an OLED in a microcavity, in: B.P. Rand, C. Adachi, V. van Elsbergen (Eds.), International Society for Optics and Photonics, 2012: p. 843515.

[195] Y.-C. Chen, C.-Y. Gao, K.-L. Chen, T.-H. Meen, C.-J. Huang, Enhancement and Quenching of Fluorescence by Silver Nanoparticles in Organic Light-Emitting Diodes, J. Nanomater. 2013 (2013) 1–5.

[196] X. Yang, R. Wang, C. Fan, G. Li, Z. Xiong, G.E. Jabbour, Ethoxylated polyethylenimine as an efficient electron injection layer for conventional and inverted polymer light emitting diodes, Org. Electron. 15 (10) (2014) 2387–2394.

[197] S. Tang, A. Sandström, J. Fang, L. Edman, A solution-processed trilayer electrochemical device: Localizing the light emission for optimized performance, J. Am. Chem. Soc. 134 (34) (2012) 14050–14055.

[198] S. So, W. Choi, C. Cheng, L.M. Leung, C.F. Kwong, Surface preparation and characterization of indium tin oxide substrates for organic electroluminescent devices, Appl. Phys. A Mater. Sci. Process. 68 (1999) 447–450.

[199] P. de Bruyn, D.J.D. Moet, P.W.M. Blom, A facile route to inverted polymer solar cells using a precursor based zinc oxide electron transport layer, Org. Electron. 11 (8) (2010) 1419–1422.

[200] A. Ryer, The Light Measurement Handbook, International Light Technologies, 1997.

[201] Merck KGaA, Polymer Yellow PDY-132 (Super Yellow) Datasheet, 2012.

[202] Y. Cao, Q. Pei, M.R. Andersson, G. Yu, A.J. Heeger, Light-Emitting Electrochemical Cells with Crown Ether as Solid Electrolyte, J. Electrochem. Soc. 144 (12) (1997) 317–320.

[203] K.H. Lee, H.W. Jang, K.-B. Kim, Y.-H. Tak, J.-L. Lee, Mechanism for the increase of indium-tin-oxide work function by O2 inductively coupled plasma treatment, J. Appl. Phys. 95 (2) (2004) 586–590.

[204] Z. Shu, O. Pabst, E. Beckert, R. Eberhardt, A. Tünnermann, Inkjet Printed Organic Light-emitting Electrochemical Cells for Disposable Lab-on-chip Applications Manufactured at Ambient Atmosphere1, Mater. Today Proc. 3 (3) (2016) 733–738.

[205] J. Fang, P. Matyba, L. Edman, The design and realization of flexible, long-lived light-emitting electrochemical cells, Adv. Funct. Mater. 19 (16) (2009) 2671–2676.

[206] X. Li, F. AlTal, G. Liu, J. Gao, Long-term, intermittent testing of sandwich polymer light-emitting electrochemical cells, Appl. Phys. Lett. 103 (24) (2013) 243304.

[207] Y. Shao, G.C. Bazan, A.J. Heeger, LED to LEC transition behavior in polymer light-emitting devices, Adv. Mater. 20 (6) (2008) 1191–1193.

[208] Y.-P. Jhang, H.-F. Chen, H.-B. Wu, Y.-S. Yeh, H.-C. Su, K.-T. Wong, Improving device efficiencies of solid-state white light-emitting electrochemical cells by adjusting the emissive-layer thickness, Org. Electron. 14 (10) (2013) 2424–2430.

[209] P. Matyba, H. Yamaguchi, M. Chhowalla, N.D. Robinson, L. Edman, Flexible and

metal-free light-emitting electrochemical cells based on graphene and PEDOT-PSS as the electrode materials, ACS Nano. 5 (1) (2011) 574–580.

[210] X. Zhang, F. Wei, X. Liu, W. Zhu, X. Jiang, Z. Zhang, Obtaining high-efficiency red electrophosphorescent OLEDs by changing the thickness of light-emitting layer, Displays. 28 (3) (2007) 150–153.

[211] A. Uniyal, P. Mittal, Improvement in performance of OLED by introducing additional hole blocking layer, in: Adv. Intell. Syst. Comput., Springer, Singapore, 2017: pp. 1051–1056.

[212] K. Narayan, S. Varadharajaperumal, G. Mohan Rao, M. Manoj Varma, T. Srinivas, Effect of thickness variation of hole injection and hole blocking layers on the performance of fluorescent green organic light emitting diodes, Curr. Appl. Phys. 13 (1) (2013) 18–25.

[213] C.K. Kim, I.H. Noh, T.S. Lee, B.W. Lee, C. Hong, D.G. Moon, Efficient white organic light-emitting diodes based on a balanced split of the exciton-recombination zone using a graded mixed layer as an electron-blocking layer, J. Soc. Inf. Disp. 18 (1) (2010) 97–102.

[214] C. Roldán-Carmona, T. Akatsuka, M. Sessolo, S.E. Watkins, H.J. Bolink, Engineering Charge Injection Interfaces in Hybrid Light-Emitting Electrochemical Cells, ACS Appl. Mater. Interfaces. 6 (22) (2014) 19520–19524.

[215] A. Sandström, H.F. Dam, F.C. Krebs, L. Edman, Ambient fabrication of flexible and large-area organic light-emitting devices using slot-die coating, Nat. Commun. 3 (1002) (2012) 1002.

[216] Schott AG, Flexible Glass for Printed Electronics, <http://www.schott.com/english/news/press.html?NID=com4937> (accessed July 27, 2017).

[217] A. Sharma, S.G. Schulman, Introduction to fluorescence spectroscopy, Microchem. J. 65 (3) (2000) 353.

[218] H. Becker, A. Lux, A.B. Holmes, R.H. Friend, PL and EL quenching due to thin metal films in conjugated polymers and polymer LEDs, Synth. Met. 85 (1–3) (1997) 1289–1290.

[219] A.L. Burin, M.A. Ratner, Exciton Migration and Cathode Quenching in Organic Light

Emitting Diodes, J. Phys. Chem. A. 104 (20) (2000) 4704–4710.

[220] F. Liu, J.-M. Nunzi, Phosphorescent organic light emitting diode efficiency enhancement using functionalized silver nanoparticles, Appl. Phys. Lett. 99 (12) (2011) 123302.

[S1] Majority of section 4.2.1 and 6.2 are reproduced from Materials Today: Proceedings, Vol 3 (3), Z. Shu, O. Pabst, E. Beckert, R. Eberhardt, A. Tünnermann, Inkjet Printed Organic Light-emitting Electrochemical Cells for Disposable Lab-on-chip Applications Manufactured at Ambient Atmosphere, Pages 733-738., Copyright (2017), with permission from Elsevier.

[S2] Majority of section 7.1 are reproduced from Materials Today: Proceedings, Vol 4 (4), Z. Shu, F. Kemper, E. Beckert, R. Eberhardt, A. Tünnermann, ITO-Free, Fully Solution Processed Transparent Organic Light-Emitting Electrochemical Cells on Thin Glass, Pages 5039–5044, Copyright (2017), with permission from Elsevier.

[S3] Majority of section 7.3 and Figure 4-13 are reproduced from Z. Shu, F. Kemper, E. Beckert, R. Eberhardt and A. Tünnermann, *RSC Adv.*, 2017, **7**, 26384 with permission from the Royal Society of Chemistry.

Appendix: Dynamic doping analysis for ITO anode and PEDOT:PSS cathode

In order to simulate the similar situation to the sandwich OLECs, planar OLECs with ITO and PEDOT:PSS electrodes were also fabricated. SuperYellow LEP was used in this study because the Merck blue LEP was run out. The detail of the manufacturing process is described in section 4.2.3. Figure 8-1 illustrates the doping propagation profiles at different time after applying an electrical potential of 500 V between PEDOT:PSS anode and ITO cathode.

Planar SY OLEC with an inkjet-printed PEDOT:PSS as an anode and a pre-patterned ITO as a cathode showed similar doping propagation behavior as the planar blue OLEC: P-doping propagates much faster than N-doping. Thus, the intrinsic / light-emitting area is very close to cathode. It is well-know that the generated excitons from electron and hole recombination can be fully quenched when it is within 20 nm to metal layers [218,219]. Especially, when metal cathode such as silver was inkjet printed from nanoparticle dispersion and is not fully sintered due to thermal stability limitation of underneath organic layers, excitons can be also quenched by metal nanoparticles [195,220]. Consequently, in order to avoid the high efficiency reduction because of metal cathodes and metal nanoparticles, ITO or PEDOT:PSS and ZnO combination (see chapter 7.1) were adopt as the alternative cathodes for fully solution-processed OLECs.

As indicated in Figure 8-1, the p-doping propagate much faster than n-doping, which fits the theory that most LEPs are hole transporting materials. The n-doping and p-doping fronts met each other after approximately 2 min. P-doping has weaker photoluminance light quenching than n-doping at very beginning. Thus, it is a bit difficult to observe from the photo images. Afterwards n-doping and p-doping continued propagating towards each other. I believe that at this point the intrinsic area was not only determined by the hole and electron mobility of the LEP, but also influenced by the external potential and ionic mobility. The intrinsic area (where electrons and holes meet and emit light) was shifted towards the middle of the junction. Nevertheless, the strong photoluminescent light quenching because of over-doping led to weak light emitting and out-coupling. After continuing doping for in total 20 min, the photoluminescent light was strongly quenched, and the intrinsic area was hardly observed (see Figure 8-2, first image at 0 s). Moreover, signs of strong over-doping can be also seen for

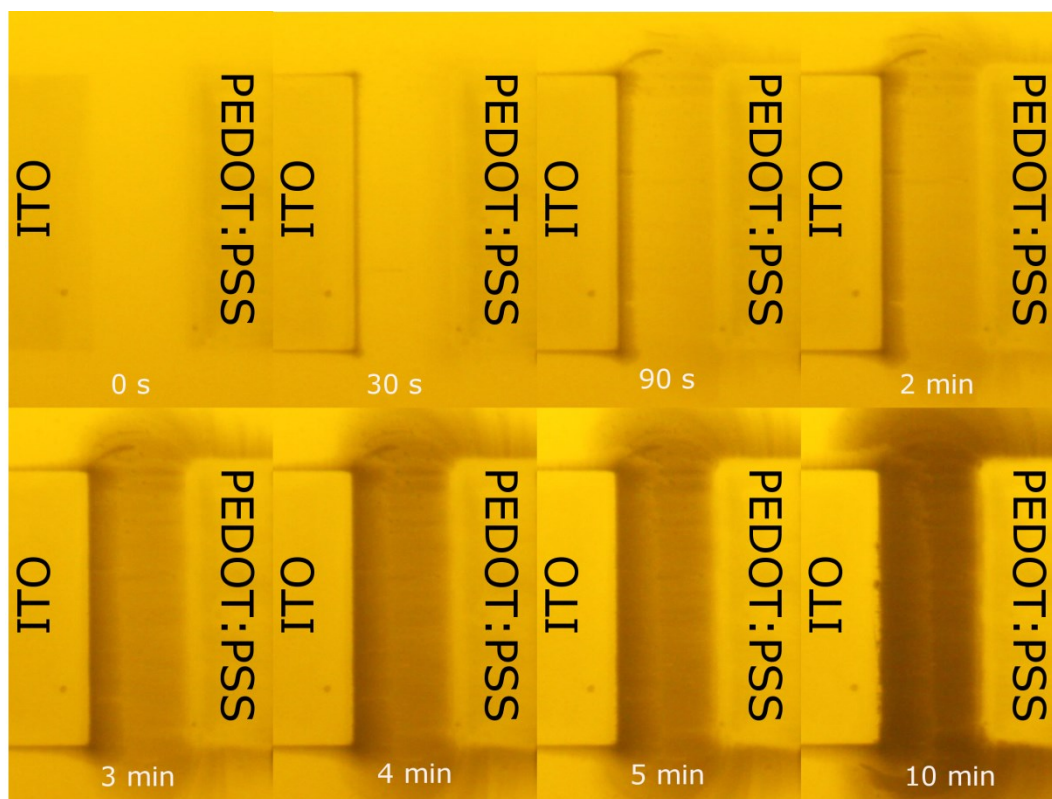both n- and d-doping, as extra darken areas can be clearly seen at edges of ITO and PEDOT:PSS electrodes.

Figure 8-1 Photographs taken at various times (0 s, 30 s, 90 s, 2 min, 3 min,4 min, 5 min and 10 min) during the charging process of an ITO ‖ (SuperYellow LEP +DCH18C6 + LiCF$_3$SO$_3$, with a mass ratio of 1:1:0.2) ‖ PEDOT:PSS planar OLEC with an inter-electrode distance of 300 μm operating at V= +500 V and at room temperature. The negative electrode is positioned to the left. The photographs were taken in a dark room under the illumination of a UV LED array (365 nm) to view the doping-induced photoluminance quenching.

It is well-known that the electrochemical doping of OLECs is a dynamic doping. The doped area will relax over time once there is no electrical potential between electrodes. Figure 8-2 illustrates the relaxation process of a SuperYellow OLEC after doping at 500 V for 20 min. The images were taken at 0 s, 5 s, 10 s, 30 s, 1 min,2 min, 3 min and 9 min after turning off the electrical potential. The intrinsic area became more and more visible during the relaxation process. It is important to observe that there was fast relaxation of n-doping, while little relaxation for p-doping. At the images, which were taken at 2 min, 3 min and 9 min, a relaxation of light p-doping area can be observed. This confirmed that the p-doping had slower relaxation rate than n-doping. Another proven can be seen in the first image of Figure 8-4. After relaxation of 1 h, the p-doping front is still at more or less the same position as observed at 9 min. The reason is not clear to the author. Several explanations could be: 1) work-function mismatch. SuperYellow has a HOMO level of -3 eV and LOMO level of -5.4 eV,

while the ITO and PEDOT:PSS have work-function of -4.7 eV and -5.2 eV, respectively. There is work-function mismatch of 2.3 eV at the cathode side, while 0.4 eV at the anode side. Hence, these could lead to slow an n-doping and shorter n-doping relaxation, while fast p-doping rand longer p-doping relaxation. 2) Dynamic ionic mobility deviations with and without voltage bias. Theoretically, the ions has much lower ionic mobility at room temperature than at elevated temperature (> 60 °C), which is the basic principle of room temperature frozen P-i-N junctions[151]. However, doping can be easily observed at room temperature when the dopant concentration is very high (e.g. mass ratio of 0.2). The doping propagation process shown in Figure 8-1 was record at room temperature. The dopant propagation can be hardly observed at room temperature when the dopant concentration is much lower (e.g. mass ratio of 0.02). Therefore, there could be an ionic mobility deviation between different dopant concentration, with or without external electrical potential and electron & hole mobility. 3) An intrinsic difference between n-doping and p-doping of LEPs. Besides dynamic electrochemical doping, there could be side effects of p-doping and modification of materials.
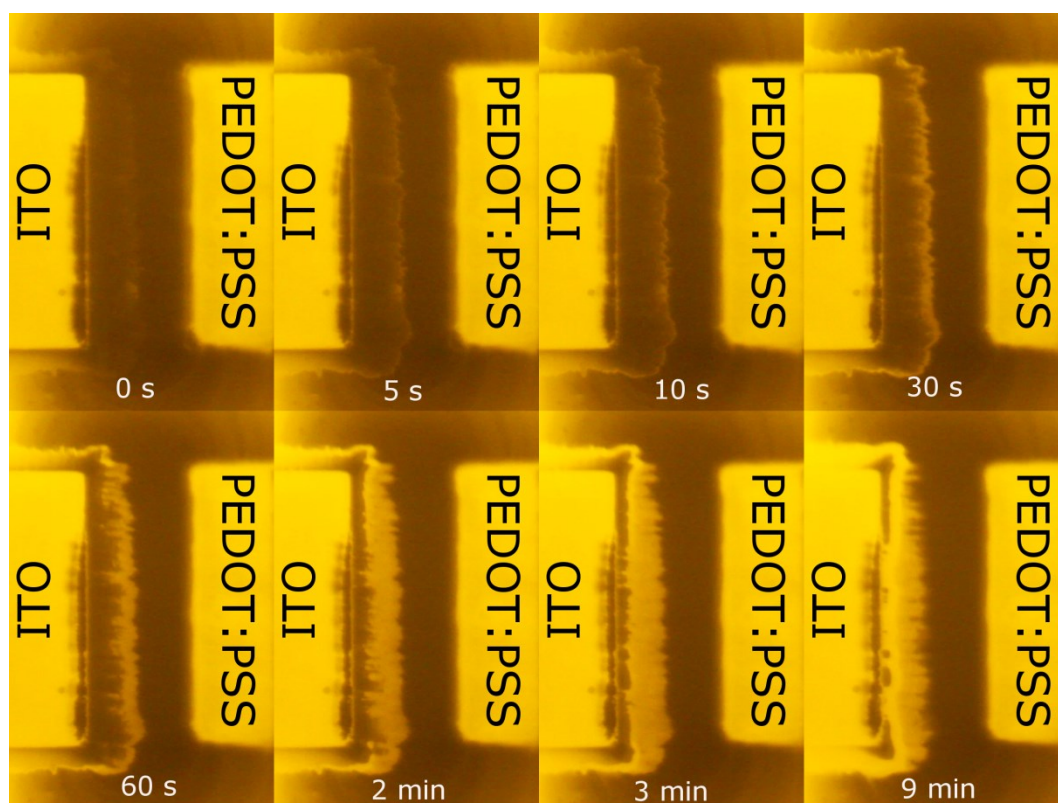

Figure 8-2 Photographs taken at various times (0 s, 5 s, 10 s, 30 s, 1 min, 2 min, 3 min and 9 min) during the relaxation process of an ITO ‖ (SuperYellow LEP +DCH18C6 + LiCF$_3$SO$_3$, with a mass ratio of 1:1:0.2) ‖ PEDOT:PSS planar OLEC with an inter-electrode distance of 300 μm operating at no voltage bias and at room temperature. The negative electrode is positioned to the left. The photographs were taken in a dark room under the illumination of a UV LED array (365 nm) to view the doping-induced photoluminance quenching.

After relaxation for 1 h, the same OLEC sample was *in situ* doped again at 500 V at room temperature. The doping propagation process was recorded and images were taken at 0 s, 5 s, 10 s, 20 s, 30 s, 2 min, 5 min, and 10 min after applying forward electrical potential, as depicted in Figure 8-4. For the second doping process, the n- and p-doping fronts met much faster at 10 s instead of 2 min for the first time. One important reason could be the little relaxation of p-doping area. Even though, the n-doping is much faster than the first time by comparing the Figure 8-1 and Figure 8-4. This indicates that there was still remaining n-doping within the active layer. It could mostly due to the low ionic conductivity of DCH18C6 at room temperature.
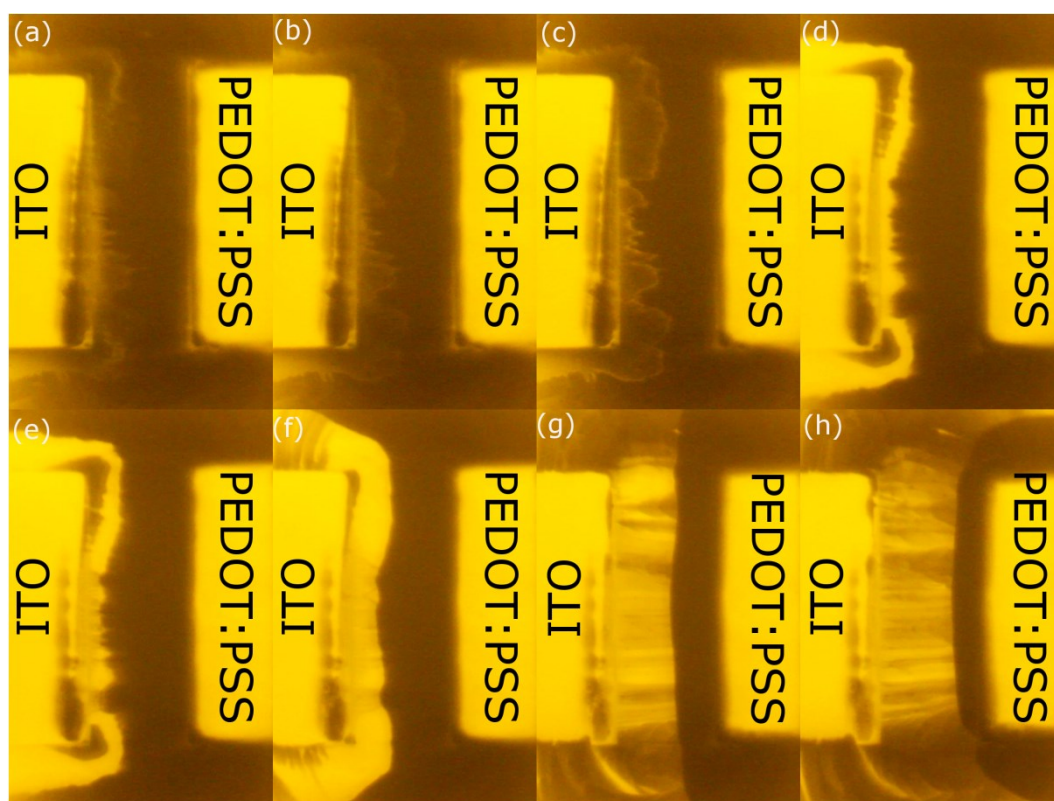

Figure 8-3 Photographs of doping and relaxation process of an ITO ‖ (SuperYellow LEP +DCH18C6 + LiCF$_3$SO$_3$, with a mass ratio of 1:1:0.2) ‖ PEDOT:PSS planar OLEC with an inter-electrode distance of 300 μm. The photographs were taken at (a) after 10 min doping at 1000 V at room temperature, and (b) 1 s, (c) 10 s, and (d) 10 min after turn off the electrical potential. Immediately after 10 min relaxation, a reverse bias of 1000 V was applied; the photographs were taken at (e) 1 s, (f) 30 s, (g) 5 min, (h) 10 min, respectively. The negative electrode is positioned to the left. The photographs were taken in a dark room under the illumination of a UV LED array (365 nm) to view the doping-induced photoluminance quenching

The position of the intrinsic area of *in situ* generated P-i-N junction depended on the external electrical potentials as well. As depicted in Figure 8-3 (a)-(d), the intrinsic part was pushed towards to cathode side (the ITO electrode) under 1000 V compared to 500 V forward

biases. This confirmed that not only the electron / hole as well as ionic mobility influence the doping profile of *in situ* generated P-i-N junctions, but also the external electrical bias. Figure 8-3 (e)-(h) illustrates the doping propagation process under 1000 V reverse bias (ITO connected positive potential while PEDOT:PSS connected negative potential) after 10 min relaxation process of 1000 V forward doping. The photographs were taken at (e) 1 s, (f) 30 s, (g) 5 min, (h) 10 min after applied the 1000 V reverse bias, respectively. There is only 1 s different between Figure 8-3 (e) and (d), and the forward doping from ITO electrode has already propagated and met the pre-doped p-doping under the forward bias. This confirmed again the fast relaxation of n-doping and fast p-doping of the LEPs. It can be seen at Figure 8-3(h) that the retreat of p-doping area is still rather slow, even under 1000 V reverse bias. After 10 min reverse doping, there is still around 40% p-doping area remaining. Therefore, p-doping is quite stable at both no bias and reverse bias.
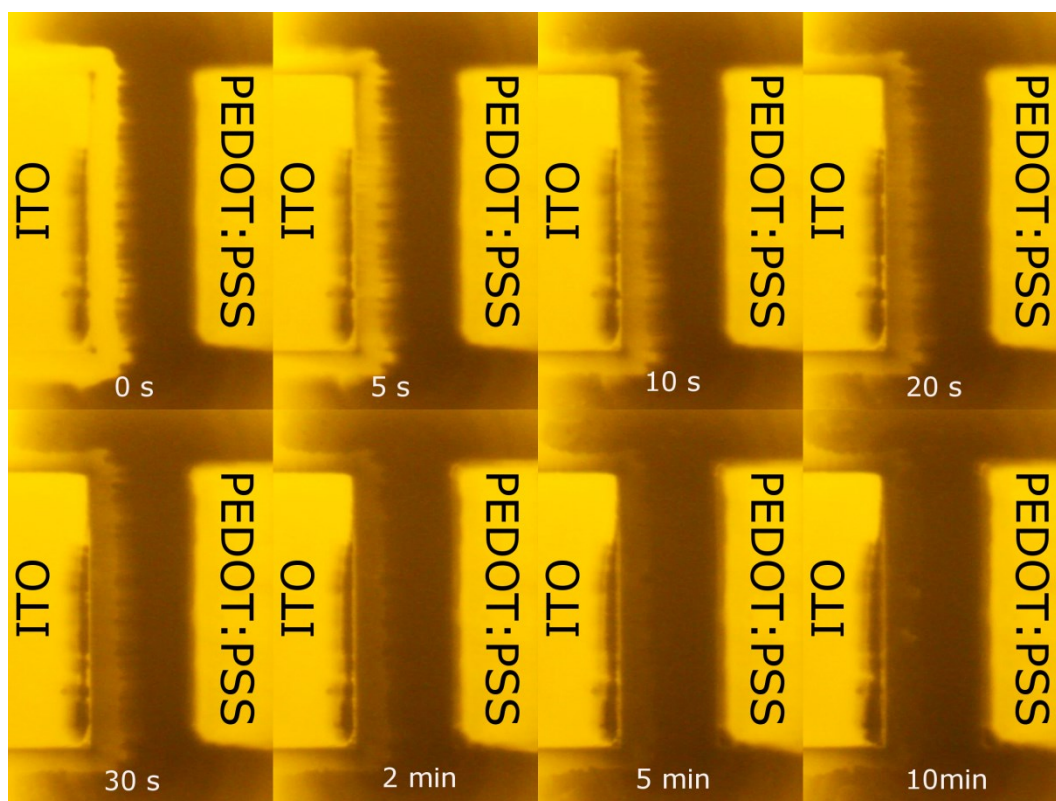

Figure 8-4 Photographs taken at various times (0 s, 5 s, 10 s, 20 s, 30 s, 2 min, 5 min, and 10 min) during the second doping process of an ITO || (SuperYellow LEP +DCH18C6 + LiCF$_3$SO$_3$, with a mass ratio of 1:1:0.2) || PEDOT:PSS planar OLEC with an inter-electrode distance of 300 μm operating at no voltage bias and at room temperature after relaxation of 1 h. The negative electrode is positioned to the left. The photographs were taken in a dark room under the illumination of a UV LED array (365 nm) to view the doping induced photoluminance quenching.

After observing the dynamic *in situ* doping propagation of SuperYellow OLEC between ITO and PEDOT.PSS electrodes, it can be concluded that: 1) p-doping propagates faster than n-doping at forward bias; 2) n-doping area relaxes relatively fast under no and reverse bias, while p-doping is rather stable and slow retreat under no and reverse bias; 3) The profile of *in situ* generated P-i-N junction is influenced by the external potential bias. Based on this information, a dynamic AC operation method of sandwich OLEC can be derived. In order to achieve as high as possible efficiency, the intrinsic part of P-i-N junction should be as center as possible. Therefore, a sandwich OLEC should be pre-doped at relative low voltage such as 7 V until the maximum brightness has been achieved under the elevated temperature (e.g. > 60 °C). That should be the time the n- and p-doping area meet and before over-doping starts. After the pre-doping, the sandwich OLEC can be operated at pulsed mode (e.g. up to 100 ms pulse-width) at high voltages (up to 50 V) to emit high brightnesses. The short pulse-width is to ensure that there is little p-doping while enough n-doping so that the electrons and holes can be injected, transported and combined to emit light. A much longer off-duty time should be implemented so that there is enough time for n-doping relaxation.

Nomenclature

Symbols

Symbol	Full expression	Unit
d	Thickness	m
E	Electric field	$V\ m^{-1}$
f	frequency	Hz
I	Electric current	A
j	Electric current density	mA/cm^2
k	Extinction coefficient	-
L	Light-emitting brightness	cd/m^2
M_n	the number average molecular	Kg/mol
M_w	the weight average molecular weight	Kg/mol
n	Refractive index	-
R	resistance	Ω
R_a	surface roughness	m
t	time	s
T_C	Curie temperature	°C
T_d	Decomposition temperature	°C
T_g	glass transition temperature	°C
V	voltage	V
γ	recombination probability of injected holes and electrons	
ε	dielectric permittivity	$F\ m^{-1}$
η	efficiency	-
η_{ext}	external quantum efficiency	-
η_{int}	internal quantum efficiency	-
η_{out}	Light out-coupling efficiency	-
λ	Optical light wavelength	nm
ρ	resistivity	$\Omega\ m$

Abbreviations

AFM	atomic force microscopy
AgNW	Silver nanowire
Al:ZnO	Al-doped Zinc oxide
Al:ZnO:PEI	Al-doped Zinc oxide mixture with branched polyethylenimine
CAD	computer-aided design
CP	Conjugated polymer
DCH18C6	Dicyclohexano-18-crown-6
DI-water	Distilled water
DoD	Drop-on-demand
EDL	electric double layer
EHL	Electron blocking layer
EIL	Electron injection layer
EML	Emissive layer
ETL	Electron transport layer
F8BT	poly(9,9′-dioctylfluorene)-co-benzothiodiazole
FAM	Fluorescein amidite
HBL	Hole blocking layer
HIL	Hole injection layer
HOMO	The highest occupied molecular orbital
HTL	Hole transport layer
iTMC	Ionic transition metal complex
ITO	Indium tin oxide
IR	infrared
I - V	Current - Voltage
J - V	Current density - Voltage
LCD	Liquid crystal display
LED	Light emitting diode
LEP	Light emitting polymer
$LiCF_3SO_3$	Lithium trifluoromethanesulfonate
LiF	Lithium fluoride
LiTf	Lithium triflate
LoC	lab-on-a-chip
LoD	Limit of detection

LUMO	The lowest unoccupied molecular orbital
MEH-PPV	Poly[2-methoxy-5-(2-ethylhexyloxy)-1,4-phenylenevinylene]
OLEC	organic light-emitting electrochemical cell
OLED	organic light-emitting diode
OPD	organic photodiode
OPV	organic photovoltaics
P3TH	poly(3-hexylthiophen-2,5-diyl)
PC	polycarbonate
PCBM	phenyl-C61-butyric acid methyl ester
PDI	Polydispersity index
PDMS	poly(dimethyl siloxane)
PE	polyethylene
PEDOT:PSS	poly(3,4-ethylenedioxythiophene):polystyrene sulfonate
PEI	branched polyethylenimine
PEO	Poly(ethylene oxide)
PET	poly(ethylene terephthalate)
PLEC	polymer light-emitting electrochemical cells
PMMA	poly(methyl methacrylate)
PP	Polypropylene
PTFE	Polytetrafluoroethylene
RF	radio frequency
RFID	radio-frequency identification
RGB	red, green and blue
S/N	signal to noise
SEM	scanning electron microscope
SY	SuperYellow light-emitting polymer
TFT	Thin film transistor
UPS	Ultraviolet photoelectron spectroscopy
V – L	Voltage – brightness
wt	weight
$Zn(acac)_2$	Zinc acetylacetonate hydrate
ZnO	Zinc oxide

Prefixes

Symbol	Prefix	10^n
G	giga	10^9
M	mega	10^6
k	kilo	10^3
c	centi	10^{-2}
m	milli	10^{-3}
μ	micro	10^{-6}
n	nano	10^{-9}
p	pico	10^{-12}
f	femto	10^{-15}

List of publications

Refereed publications

- Z. Shu, E. Beckert, R. Eberhardt and A. Tünnermann, ITO-free, inkjet-printed transparent organic light-emitting diodes with single inkjet-printed Al:ZnO:PEI interlayer for sensing applications, J. Mater. Chem. C, 2017, DOI: 10.1039/C7TC04084A. *(submitted and accepted after submission of thesis, but before the disputation of dissertation)*

- **Z. Shu**, F. Kemper, E. Beckert, R. Eberhardt, A. Tünnermann, Highly sensitive on-chip fluorescence sensor with integrated fully solution processed organic light sources and detectors, RSC Adv. 7 (42) (2017) 26384–26391.

- **Z. Shu**, F. Kemper, E. Beckert, R. Eberhardt, A. Tünnermann, ITO-Free, Fully Solution Processed Transparent Organic Light-Emitting Electrochemical Cells on Thin Glass, Mater. Today Proc. 4 (4) (2017) 5039-5044.

- **Z. Shu**, O. Pabst, E. Beckert, R. Eberhardt, A. Tünnermann, Inkjet Printed Organic Light-emitting Electrochemical Cells for Disposable Lab-on-chip Applications Manufactured at Ambient Atmosphere, Mater. Today Proc. 3 (3) (2016) 733–738.

Non-refereed publications:

- **Z. Shu**, E. Beckert, R. Eberhardt, A. Tünnermann, Fully Solution Processed Organic Light-emitting Electrochemical Cells (OLEC) with ZnO Interlayer for Lab-on-Chip Applications, in: Proc. Printing for Fabrication, 2016

- **Z. Shu**, O. Pabst, E. Beckert, R. Eberhardt, A. Tünnermann, Fully solution-processed organic light-emitting electrochemical cells (OLEC) with inkjet-printed micro-lenses for disposable lab-on-chip applications at ambient conditions , in: Proc. SPIE 9745, Organic Photonic Materials and Devices XVIII, 97450W (February 24, 2016).

- **Z. Shu**, O. Pabst, F. Kemper, E. Beckert, R. Eberhardt, A. Tünnermann, Inkjet printing multifunctionalities on microfluidic chips for biosensing applications, in: Proc. Printing Future days, 2013.

- E. Beckert, O. Pabst, **Z. Shu**, J. Perelaer, R. Eberhardt, A. Tünnermann, U. S. Schubert, H. Becker, Inkjet-printed functionalities for microfluidic lab-on-a-chip systems, in: Proc. Smart Systems Integration, 2013.

- J. Perelaer, **Z. Shu**, A. Teichler, A. Wild, U. S. Schubert, Inkjet printing of conducting polymers for OLED applications, in: Proc. LOPE-C, 2012, pp 30-32.

Presentations

- **Z. Shu**, E. Beckert, R. Eberhardt, A. Tünnermann, Highly sensitive on-chip fluorescence sensor with integrated fully solution processed organic light sources and detectors, at ISFOE17, 3-6 July 2017, Thessaloniki, Greece.

- **Z. Shu**, E. Beckert, R. Eberhardt, A. Tünnermann, Fully Solution Processed, ITO-free Organic Light-emitting Electrochemical Cells (OLEC) with ZnO Interlayer for Lab-on-Chip Applications, at: LOPE-C 2016, 05.-07.04.2016, Munich, Germany.

- **Z. Shu**, A. Teichler, J. Perelaer, A. Wild, E. Beckert, R. Eberhardt, U. S. Schubert, A. Tünnermann, Inkjet Printing of Conducting Polymers for OLED Applications, at: SID-ME, 07.-08.05.2012, Stockholm, Sweden.

Poster:

- **Z. Shu**, O. Pabst, E. Beckert, R. Eberhardt, A. Tünnermann, Fully Solution-Processed Blue Organic Light-emitting Electrochemical Cells (OLEC) for Microfluidic Lab-on-a-chip Applications, at: 10th International Conference on Electroluminescence and Optoelectronic Devices, 31.08 – 03.09.2014, Cologne, Germany.

Publications not directly related to the topic of the thesis

- C. Hoera, M.M. Skadell, S.A. Pfeiffer, M. Pahl, **Z. Shu**, E. Beckert, D. Belder, A chip-integrated highly variable thermal flow rate sensor, Sensors Actuators B Chem. 225 (2016) 42–49.

- C. Hoera, S. Ohla, **Z. Shu**, E. Beckert, S. Nagl, D. Belder, An integrated microfluidic chip enabling control and spatially resolved monitoring of temperature in micro flow reactors, Anal. Bioanal. Chem. 407 (2) (2015) 387–396.

- E. Beckert, R. Eberhardt, O. Pabst, F. Kemper, **Z. Shu**, A. Tünnermann, J. Perelaer, U. Schubert, H. Becker, Inkjet printed structures for smart lab-on-chip systems, (2013) 86150E–86150E–10.

■ A. Teichler, **Z. Shu**, A. Wild, C. Bader, J. Nowotny, G. Kirchner, S. Harkema, J. Perelaer, U.S. Schubert, Inkjet printing of chemically tailored light-emitting polymers, Eur. Polym. J., 49 (8) (2013) 2186–2195.

Acknowledgements

I would like to express my gratitude to all those who have helped, contributed, and supported me for my PhD studies.

First of all, I want to thank Prof. Dr. A. Tünnermann for scientific supervising my PhD research and for the valuable advices and suggestions. I would like to thank Dr. Ramona Eberhardt und Dr. Erik Beckert to provide the possibility to work in Fraunhofer Institute for Applied Optics and Precision Engineering (IOF) and for providing a nice working environment as well as financial support so that I can have necessary experimental setups and materials to research in this new field.

For the constructive working atmosphere, I want to thank all the colleagues of precision engineering department. In particular, I want to thank Dr. Oliver Pabst for introduction and guiding on the printing research in IOF, numerous valuable discussion and suggestions on my works. I also want to thank Falk Kemper. We are the only two researchers in-house who are doing inkjet printing of organic diodes. Without sharing the knowledge and experience, it will take even longer time to achieve the results I have presented in this dissertation. Extra credit should be given to him for providing OPDs and assisting in demonstrator characterization. I also want to thank all the supports and discussions of other former and current printing group members, i.e. Sophie Sauva, Maximillian Reif, Manuel Kirsche, Norman Böhme, Amaris Castanon, Sean Garnsey, Pauline Hibon, and Stefan Mittwoch.

Many thanks should be given to Dr. Norbert Danz for valuable discussions on OLEDs related issues, for providing various measurement setups, and helps on electroluminance spectrum measurement. I want to thank Christian Hupel and Stefan Schwinde for SEM measurements, Ben Zaage for programming LabVIEW so that I can drive the power supply and records results from the pico-amperemeter, Uwe Lippmann for allowing using Luminance camera, Dr. Peter Dannberg and Dr. Robert Leitel for providing the possibility to use the spincoater in the cleanroom. I want to thank Dr. Stenzel Olaf's group for thin film deposition and characterization. More specifically, I want to thank Dr. Steffen Wilbrandt for refractive index measurement as well as transmission and reflection measurement, Mrs. Heidi Haase (previously at Fraunhofer IOF) for vacuum evaporation of LiF, Al, and Al_2O_3 thin films on solution-processed OLEDs. I also want to thank Abbe School of Photonics, in particular Prof. Pertsch, Claudia Lang, Szilvia Mammel, Dörte Hansen and Dorit Schmidt, for providing me the chance to come to Jena for studying my Master.

XXXVII

Ehrenwörtliche Erklärung

Ich erkläre hiermit ehrenwörtlich, dass ich die vorliegende Arbeit selbstständig, ohne unzulässige Hilfe Dritter und ohne Benutzung anderer als der angegebenen Hilfsmittel und Literatur angefertigt habe. Die aus anderen Quellen direkt oder indirekt übernommenen Daten und Konzepte sind unter Angabe der Quelle gekennzeichnet. Bei der Auswahl und Auswertung folgenden Materials haben mir die nachstehend aufgeführten Personen in der jeweils beschriebenen Weise unentgeltlich geholfen:

1. Dr. Steffen Wilbrandt (Fraunhofer IOF): Measuring refractive indices and extinction coefficients of PEDOT:PSS, LEPs and OLECs thin films in section 6.1, Figure 6-2.

2. Mr. Falk Kemper (Fraunhofer IOF): Providing solution-processed OPDs and helping on fluorescent signal detection with OPDs in section 7.3.

Weitere Personen waren an der inhaltlich-materiellen Erstellung der vorliegenden Arbeit nicht beteiligt. Insbesondere habe ich hierfür nicht die entgeltliche Hilfe von Vermittlungs- bzw. Beratungsdiensten (Promotionsberater oder andere Personen) in Anspruch genommen. Niemand hat von mir unmittelbar oder mittelbar geldwerte Leistungen für Arbeiten erhalten, die im Zusammenhang mit dem Inhalt der vorgelegten Dissertation stehen. Die Arbeit wurde bisher weder im In- noch im Ausland in gleicher oder ähnlicher Form einer anderen Prüfungsbehörde vorgelegt. Die geltende Promotionsordnung der Physikalisch-Astronomischen Fakultät ist mir bekannt.

Ich versichere ehrenwörtlich, dass ich nach bestem Wissen die reine Wahrheit gesagt und nichts verschwiegen habe.

Jena, ...

Zhe Shu